Copyright
by
John Charles Robinson
1995

ATOM OPTICS:
A NEW TESTING GROUND FOR
QUANTUM CHAOS.

by

JOHN CHARLES ROBINSON, B.A., M.A.

DISSERTATION

Presented to the Faculty of the Graduate School of

The University of Texas at Austin

in Partial Fulfillment

of the Requirements

for the Degree of

DOCTOR OF PHILOSOPHY

THE UNIVERSITY OF TEXAS AT AUSTIN

December 1995

ATOM OPTICS:
A NEW TESTING GROUND FOR
QUANTUM CHAOS.

APPROVED BY
DISSERTATION COMMITTEE:

Supervisor: _____

_____

_____

_____

_____

This dissertation is dedicated to
Andrea and Anna.

Acknowledgements

I am indebted to my advisor, Professor Mark G. Raizen, for his insight and guidance during the course of this work. It was he who found the theoretical proposal of Graham, Schlautmann, and Zoller [1], rescued it from certain obscurity, and turned it into one of the premier experiments of both atom optics and quantum chaos. With his unending stream of new ideas, this type of research will be at the forefront of physics for many years to come.

I am grateful to have had the opportunity to work closely with postdoctoral fellow Dr. Fred L. Moore, with whom I took all of the data for Chapters 2,3, 4, and 6. His stubborn determination and uncanny ability to make things work allowed this project to progress rapidly. He is without a doubt the most talented experimentalist that I have ever had the privilege of working with.

Thanks also go to Cyrus Bharucha for being an unending source of useful discussion for this project from its very beginning. It is his unending attention to detail that allowed us to keep all of the 'scaled' quantities straight. I would like to thank Kirk Madison for his competence and enthusiasm in programming the GPIB devices. I consider myself to be very lucky to have had the chance to work with and learn from Cyrus and Kirk. I would like to thank postdoctoral fellow Dr. Steve Wilkinson, with whom Cyrus, Kirk, and I took the data presented in Chapter 5. I know that the future of this experiment will be in good hands with this crew.

I would like to thank Dr. Bala Sundaram for his theoretical support,

and encyclopedic knowledge of the physics literature. He provided invaluable insights about quantum chaos and performed numerical simulations. Thanks also go to Professor Qian Niu and his students Georgios Georgakis and Bob Jahnke for the quantum Floquet analysis in Chapter 3, and for insights into future directions with periodic potentials. I would like to thank Martin Fischer [2] and Michael Käsbauer for the construction of the homebuilt dye laser, and John Miller for assistance with the National Instruments I/O boards and LabWindows.

I would like to acknowledge the financial support of the University of Texas at Austin, the ONR Young Investigator Program, the NSF Young Investigator Program, the Robert A. Welch Foundation, and Honeywell Inc.

ATOM OPTICS:
A NEW TESTING GROUND FOR
QUANTUM CHAOS.

Publication No. _____

John Charles Robinson, Ph.D.
The University of Texas at Austin, 1995

Supervisor: Mark G. Raizen

By using the techniques of laser cooling and trapping, the ability to control the momentum and position of atoms with light has improved drastically in the last 10 years. At the low temperatures that can be achieved, the deBroglie wavelength of an atom $\lambda_{dB} = \mathrm{h/p}$ becomes significant and the wave nature of the atom needs to be considered. "Atom optics" consists of acting on atoms to obtain effects analogous to what we know for light: reflection, refraction, diffraction, and interference. In general, however, interactions in atom optics need not have optical analogs. Light acting on atoms provides the initial state preparation and the time dependent interaction potentials that are necessary for the work described here.

The study of quantum mechanical systems that exhibit dynamical chaos in their classical limit is called "quantum chaos," and has attracted a great deal of interest in recent years. What is found are sharp deviations from classical physics, which are nonetheless fingerprints of classical chaos in the quantal behavior. The nature of these fingerprints has been explored in the atom optics experiments described here, involving the study of momentum transfer

to a sample of ultra-cold sodium atoms by a time dependent standing wave of light.

An experimental realization of the periodically driven rotor is described, where the underlying classical phase space goes from stable to chaotic as the phase modulation of the standing wave is varied. Dynamical localization, the quantum suppression of diffusion in a system that is classically chaotic, is observed. The experimental results are in good absolute agreement with a quantum Floquet analysis and with a quantum simulation.

The first direct experimental realization of the quantum δ-kicked rotor is also described. A standing wave of light is pulsed. Momentum spread of the atoms increases diffusively with every pulse until the "quantum break time" after which exponentially localized distributions are observed. Quantum resonances are found for specific values of the pulse period.

A third experiment involves momentum transfer to atoms by a single pulse of a standing wave of light. The classical mechanism of resonance overlap is seen, and the results are in good agreement with theoretical predictions.

Table of Contents

Acknowledgements **v**

Abstract **vii**

List of Figures **xi**

Chapter 1. Introduction **1**
1.1 Atom Optics 1
1.2 Classical Chaos 8
1.3 Quantum Chaos 9

Chapter 2. Experimental Realization **14**
2.1 Overview 14
2.1.1 Computer Control 19
2.2 Initial Conditions: MOT 22
2.2.1 MOT Theory 28
2.2.2 Trap Envelope 30
2.2.3 Magnetic Field Coils 32
2.2.4 1.7 GHz Sidebands 34
2.2.5 Saturated Absorption FM Spectroscopy 38
2.2.6 Scanning Fabry-Perot Cavities 42
2.3 Interaction Potential 43
2.3.1 Home Built Dye Laser 43
2.3.2 Wavemeter 45
2.3.3 Time Dependent Optical Potential: Phase Modulation 48
2.3.4 Time Dependent Optical Potential: Amplitude Modulation . 51
2.3.5 Spatial Filter and Power Calibration 53
2.3.6 Spatial Overlap 56
2.4 Detection of Momentum Transfer 58

2.4.1 Molasses . . . 58
2.4.2 Optimizing the MOT/Molasses . . . 59
2.4.3 Time of Flight . . . 61
2.4.4 CCD Camera and Data Analysis . . . 62

Chapter 3. Modulated Standing Wave (Phase Modulation) 68
3.1 Introduction . . . 68
3.2 Classical Analysis . . . 69
3.3 Quantum Analysis . . . 74

Chapter 4. δ-Kicked Rotor (Amplitude Modulation) 83
4.1 Introduction . . . 83
4.2 Standard Map Analysis . . . 85
4.3 Effect of Pulse Shape . . . 88
4.4 Quantum Break Time and Dynamical Localization . . . 89
4.5 Quantum Resonances . . . 95
4.6 Selecting Experimental Parameters . . . 96

Chapter 5. Single Pulse (Amplitude Modulation) 101
5.1 Single Pulse . . . 101
5.2 Resonance Overlap . . . 104
5.3 Adiabatic Limit . . . 108

Chapter 6. Future Directions in Atom Optic Quantum Chaos 111
6.1 Conclusions . . . 111
6.2 Future Directions . . . 112
6.3 Noise and Dissipation . . . 113
6.4 Beyond Quantum Chaos . . . 115

Bibliography 118

Vita 125

List of Figures

1.1 Standing Wave Beam Angle 7

2.1 Temperature Measurement 15
2.2 Momentum Transfer Measurement 16
2.3 Laser Table 18
2.4 Beam Experiment 20
2.5 PM Control Electronics 23
2.6 AM Control Electronics 24
2.7 Pulse Sequence 25
2.8 Vacuum Chamber Photograph 27
2.9 Power Lock Schematic 29
2.10 MOT Configuration 31
2.11 Coil Driver Circuit 34
2.12 1.7 GHz EOM 37
2.13 Term Diagram for Sodium D_2 37
2.14 Saturated Absorption Setup 40
2.15 Saturated Absorption Lockbox 41
2.16 Home-build Dye Laser 44
2.17 Wavemeter 47
2.18 PM Interaction 49
2.19 AM Interaction 53
2.20 Atom and Light Overlap 57
2.21 Time-of-Flight and Freeze-in Time Comparison 63
2.22 2 Dimensional Atomic Distributions 64
2.23 1 Dimensional Atomic Distributions 64

3.1 RMS Momentum 70
3.2 Bessel Functions J_0 and J_1 71
3.3 Lineshapes and Phase Space Portraits 75

3.4 Initial and Exponential Lineshape 77
3.5 Squeezed Initial Condition 78
3.6 Mixed Phase Space Lineshapes 80
3.7 Floquet States 82

4.1 Kicked Rotor 84
4.2 Digitized Pulse Train 85
4.3 Pulse Shapes 90
4.4 Fourier Transform of Pulse Shapes 90
4.5 Classical Phase Portrait 91
4.6 Localization Time Evolution 93
4.7 Diffusion in Energy vs. Time 94
4.8 Resonance Time Evolution 96
4.9 Quantum Resonances 97

5.1 Pulse Profile 102
5.2 Pulse Lineshapes 103
5.3 Pulse Phase Portraits and Lineshapes 106
5.4 RMS Momentum: Resonance Overlap 109

6.1 Amplitude Noise Induced Delocalization 116

Chapter 1

Introduction

1.1 Atom Optics

Light can exchange momentum with an atom incoherently or coherently, and can be viewed as the interaction of light with the imaginary or real part of polarizability, respectively [3]. The incoherent force, known as the scattering, spontaneous, or radiation pressure force, results from stimulated absorption and spontaneous re-emission of photons and is responsible for the dissipative cooling and trapping necessary for experiments described here. Though the momentum transfer from a single scattering event is insignificant compared to the room temperature thermal momentum, over 10^7 photons can be scattered per second from a single sodium atom and the force it experiences can be very large. The natural unit of momentum is the momentum transferred to an atom from absorption of one photon. One photon recoil $m\Delta \mathrm{v} = \hbar k_L$ corresponds to a velocity change of $\Delta \mathrm{v} = 3$ cm/sec for sodium. Starting from room temperature vapor, localized distributions of atoms of approximately 30 μK or an rms momentum of 4.6 $\hbar k_L$ are achieved, and serve as the starting point (initial condition) for the experiments described here.

The force arising from the coherent interaction with light, called the dipole force, results from stimulated absorption followed by stimulated emission via a virtual state. A simple picture is that the laser field polarizes the atom and the polarized atom experiences a force in the gradient field of the

laser [3]. This force becomes dominant when far detuned light (compared to the natural linewidth) is used, since the spontaneous force falls off quadratically with detuning whereas the dipole force only falls off linearly in the limit of large detuning.

$$F_{dipole} \propto \frac{I}{\delta_L} \tag{1.1}$$

$$F_{spont.} \propto \frac{I}{\delta_L^2} \tag{1.2}$$

Here δ_L is the laser detuning from resonance and I is the laser intensity. The new physics described in this work results from the dipole force interaction. Unfortunately, the dipole moments that can be induced on an atom are small, and the force is too small to overcome room temperature thermal motion. Once the atoms are cooled to an rms of $4.6\hbar k_L$ by the spontaneous force, however, these feeble forces are sufficient to control the atoms.

The ability to control the momentum and position of atoms has improved drastically in the last 10 years. At the low temperatures that can be achieved, the deBroglie wavelength of an atom

$$\lambda_{dB} = \frac{h}{p} \tag{1.3}$$

becomes significant, and equals the wavelength of laser light when the atom has only one photon recoil of momentum. Atom optics consists of acting on atoms to obtain effects analogous to what we know for light: reflection, refraction, diffraction, and interference. Atom mirrors have been constructed using evanescent waves, for example. Atom lenses can be formed at the nodes or antinodes of a standing wave. Transmission gratings for atoms have been formed by standing waves of light. Atom optics is not, however, limited to these types of processes. In general, interactions in atom optics need not even have optical analogs (unlike photons, atoms have mass and internal degrees of freedom). This field of study is going in many exciting directions, and is

too broad to summarize here. Laser cooled and manipulated atoms offer an incoherent but highly "monochromatic" source of deBroglie waves. The recent observation of the Bose condensation [4] of neutral atoms forms the first coherent source of atoms, and is likely to accelerate this field of research. It may revolutionize atom optics in the way the laser advanced light optics.

The experiments described here fit into this context of manipulating external momentum states of atoms, in regimes where the quantum mechanical aspects become important. The interaction is in the form of a standing wave of laser light, which forms a spatially periodic potential resulting from the dipole force on the atoms. The potential is made time dependent by amplitude or phase modulation. The electromagnetic field is treated classically for all the analysis here. To correctly analyze the motion of the atoms one must use quantum mechanics, however, it is instructive to compare these results with an analysis using the laws of classical mechanics. The question is what effect this standing wave has on the momentum of atoms. A rich interplay between classical and quantum physics is found, especially when classically one expects chaos, as described below (see Section 1.3). Common wisdom for people working in the area of laser cooling and trapping is that quantum effects in atomic motion will only be important at much lower temperatures than what is reached with optical molasses. The main reason for this misconception is that the main focus has been on tunneling and many-body effects, while the quantum effects that we have studied are due to a coherent interaction with the time dependent interaction.

The specific quantum mechanical form of the interaction Hamiltonian is derived as follows. Here only the dipole force will be considered. The atoms are assumed to be non-interacting, and hence only a single atom interacting with the optical field is assumed. Consider a two level atom with ground state $|g\rangle$ and excited state $|e\rangle$ with energy difference $\hbar\omega_0$, and dipole moment d subject

to a classical standing wave light field. A standing wave made of two traveling waves has the form

$$\begin{aligned}\vec{E}(x,t) &= \hat{y}E_0\cos(\omega_L t + k_L x) + \hat{y}E_0\cos(\omega_L t - k_L x) \\ &= \hat{y}2E_0\cos(\omega_L t)\cos(k_L x) \\ &= \hat{y}E_0\cos(k_L x)(e^{-i\omega_L t} + c.c.) \end{aligned} \tag{1.4}$$

The standing wave is along the x-axis and is linearly polarized along the y-axis. For this standing wave the dipole and rotating wave approximations yield the Hamiltonian [1],[5]

$$\hat{H}(x,t) = \frac{\hat{p}^2}{2M} + \hbar\omega_0|e\rangle\langle e| - (dE_0\cos(k_L x)e^{-i\omega_L t}\sigma^+ + H.c.) \tag{1.5}$$

where p is the center-of-mass momentum of the atom of mass M, and $\sigma^{\pm}$ are Pauli spin operators. The center of mass wave function is separable so we consider only motion along the x-axis. We can represent our atomic state as

$$\Psi(x,t) = \Psi_g(x,t)|g\rangle + \Psi_e(x,t)e^{-i\omega_L t}|e\rangle \tag{1.6}$$

If we apply Schrödinger's equation

$$i\hbar\frac{\partial}{\partial t}\Psi = \hat{H}\Psi \tag{1.7}$$

we get the following equation of motion

$$\begin{aligned} i\hbar(\frac{\partial\Psi_g}{\partial t}|g\rangle &+ \frac{\partial\Psi_e}{\partial t}e^{-i\omega_L t}|e\rangle - i\omega_L\Psi_e e^{-i\omega_L t}|e\rangle) = \\ &- \frac{\hbar^2}{2M}\frac{\partial^2\Psi_g}{\partial x^2}|g\rangle - \frac{\hbar^2}{2M}\frac{\partial^2\Psi_e}{\partial x^2}e^{-i\omega_L t}|e\rangle \\ &+ \hbar\omega_0\Psi_e e^{-i\omega_L t}|e\rangle - dE_0\cos(k_L x)e^{-i\omega_L t}\Psi_g|e\rangle \\ &- dE_0\cos(k_L x)\Psi_e|g\rangle \end{aligned} \tag{1.8}$$

Following the convention of [1] we define the resonant Rabi frequency $\Omega/2 = \frac{dE_0}{\hbar}$ and detuning $\delta_L = \omega_0 - \omega_L$, and operate on Eqn. 1.8 with $\langle g|$ from the left and get

$$i\hbar\frac{\partial\Psi_g}{\partial t} = -\frac{\hbar^2}{2M}\frac{\partial^2\Psi_g}{\partial x^2} - \frac{\hbar\Omega}{2}\cos(k_L x)\Psi_e \tag{1.9}$$

Similarly we operate on Eqn. 1.8 with $\langle e|$ from the left and get

$$i\hbar\frac{\partial\Psi_e}{\partial t} = -\frac{\hbar^2}{2M}\frac{\partial^2\Psi_e}{\partial x^2} - \frac{\hbar\Omega}{2}\cos(k_L x)\Psi_g + \hbar\delta_L\Psi_e \tag{1.10}$$

Sufficiently large detuning δ_L allows us to neglect spontaneous emission and simplify these equations by adiabatic elimination of the excited state amplitude. By setting $\frac{\partial\Psi_e}{\partial t} = 0$ and $\frac{\partial^2\Psi_e}{\partial x^2} = 0$, Eq. 1.10 becomes

$$\Psi_e = \frac{\Omega}{2\delta_L}\cos(k_L x)\Psi_g. \tag{1.11}$$

If we substitute Eq. 1.11 into Eq. 1.9 and define an effective Rabi frequency

$$\Omega_{eff} = \frac{\Omega^2}{\delta_L} \tag{1.12}$$

which is also known as the ac-Stark shift Ω_{AC} (not to be confused with the generalized Rabi frequency), we get

$$i\hbar\frac{\partial\Psi_g}{\partial t} = -\frac{\hbar^2}{2M}\frac{\partial^2\Psi_g}{\partial x^2} - \frac{\hbar\Omega_{eff}}{4}\cos^2(k_L x)\Psi_g, \tag{1.13}$$

resulting in the Hamiltonian

$$\hat{H} = \frac{\hat{p}^2}{2M} - \frac{\hbar\Omega_{eff}}{4}\cos^2(k_L x). \tag{1.14}$$

Or equivalently, ignoring a constant potential offset

$$\hat{H} = \frac{\hat{p}^2}{2M} - \frac{\hbar\Omega_{eff}}{8}\cos(2k_L x). \tag{1.15}$$

Sodium, though obviously not a 2-level atom, is optically pumped so that only one F level participates (see Chapter 2). Of paramount importance is that all the (nearly) degenerate m_F levels experience the same Ω_{eff} in the far detuned regime [6]. Therefore the entire ensemble of atoms experiences the same effective potential.

Quantum mechanically momentum is only transferred in discrete units of $2\hbar k_L$. The dipole force involves stimulated scattering via a virtual state.

For a traveling wave an atom absorbs a photon and re-emits it into the same direction via stimulated emission. The net result is no transfer of momentum.

$$\Longrightarrow \bullet \Longleftarrow \text{no recoil} \tag{1.16}$$

For a standing wave, however, the momentum transfer process can be visualized as stimulated absorption of a photon from one traveling wave followed by a subsequent stimulated emission into the counterpropagating traveling wave.

$$\Longrightarrow \bullet \Longrightarrow 2\hbar k_L \text{ recoil} \tag{1.17}$$

The result of this process is that the atom gains $2\hbar k_L$ of momentum parallel to the k-vector of the first traveling wave. If there is an angle θ between the two beams, the standing wave periodicity increases as

$$\frac{\lambda_{eff}}{2} = \frac{\lambda_L}{2}\frac{1}{\sin(\frac{\theta}{2})} \tag{1.18}$$

and the effective momentum kick decreases with $1/\sin(\theta/2)$ (see Fig. 1.1). This is a useful experimental tool to change the periodicity of the standing wave. In addition, as θ is decreased, a traveling wave develops but causes no momentum transfer by this stimulated interaction, as described above (overall ac-Stark shift can be ignored). For all experiments described in this work, $\theta = 180°$ (beams counterpropagating).

Classically Eq. 1.15 can be understood by modeling the atom-field interaction as a driven damped harmonic oscillator [7], with an electron of charge q and mass m_e on a spring of resonant frequency ω_0 and damping rate γ. The equation of motion for the displacement y of the charge from its equilibrium position in a standing wave polarized in the y direction (see Eq. 1.4) is:

$$\ddot{y} + \gamma\dot{y} + \omega_0^2 y = \frac{fq}{m_e} 2E_0 \cos(k_L x)\cos(\omega_L t). \tag{1.19}$$

Sodium has a large number of eigenfrequencies at which it can absorb radiation, though Eq. 1.19 only includes one at ω_0, therefore the oscillator strength f

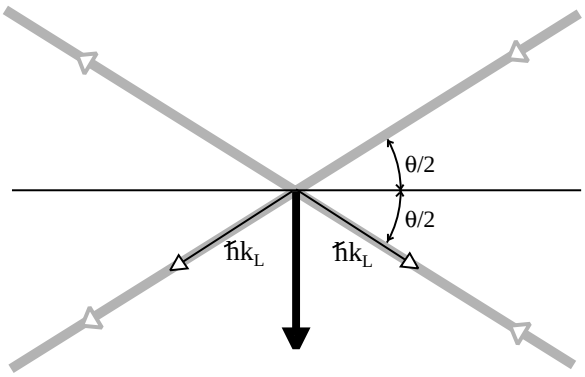

Figure 1.1: As the angle between traveling waves increases, the periodicity of the standing wave increases and the transfer of momentum due to absorption and stimulated emission decreases.

associated with this transition is included [8]. Assuming a solution of the form

$$y = \mathrm{Re}\left[y_0 e^{i(\omega_L t - \phi)}\right] \tag{1.20}$$

substituting into Eqn. 1.19 gives

$$y_0 e^{-i\phi} = \frac{2fqE_0\cos(k_L x)}{m_e(\omega_0^2 - \omega_L^2 + i\omega_L\gamma)}. \tag{1.21}$$

Again we define $\delta_L = \omega_0 - \omega_L$. For $\gamma \ll \delta_L \ll \omega_0$ the amplitude and phase are

$$y_0 = \frac{fqE_0\cos(k_L x)}{m_e\omega_0\delta_L} \tag{1.22}$$

$$\phi = \tan^{-1}(\frac{\gamma}{2\delta_L}). \tag{1.23}$$

Consider the induced electric dipole $\vec{P} = q\vec{y}$ interacting with the field. The effective potential of the atom is the time averaged interaction energy:

$$\begin{aligned} U(x) &= \langle U(x,t)\rangle \\ &= \langle -\vec{P}\cdot\vec{E}\rangle \\ &= \langle -qy_0\cos(\omega_L t - \phi)2E_0\cos(k_L x)cos(\omega_L t)\rangle. \end{aligned} \tag{1.24}$$

We integrate over one optical period $T = \frac{2\pi}{\omega_L}$ to time average:

$$\begin{aligned} U(x) &= \frac{-1}{T}\int_0^T dt\ q2E_0y_0(\cos(\omega_L t)\cos\phi + \sin(\omega_L t)\sin\phi)\cos(k_L x)\cos(\omega_L t) \\ &= -qE_0y_0\cos(k_L x)\cos(\phi). \end{aligned} \tag{1.25}$$

Substituting Eqn. 1.22 and Eqn. 1.23 into Eqn. 1.25 gives

$$U(x) = \frac{-fq^2E_0^2}{m_e\delta_L\omega_0}\cos^2(k_Lx). \tag{1.26}$$

If an arbitrary offset is ignored, a potential with the same functional form as 1.15 is found

$$U(x) = \frac{-fq^2E_0^2}{2m_e\omega_0\delta_L}\cos(2k_Lx). \tag{1.27}$$

Substitution of the oscillator strength[8] of the sodium D_2 line,

$$f = \frac{m_e\omega_0 d^2}{\hbar q^2}, \tag{1.28}$$

yields a potential identical to that of 1.15. For the sodium D_2 line $f = 0.655$ [9].

1.2 Classical Chaos

Contrary to what one may think from reading undergraduate and graduate classical mechanics texts, chaotic motion is not a rare phenomenon. Chaos refers to an effectively random behavior that is nevertheless described by a deterministic set of equations. It is not due to stochastic or random input to the system, but is intrinsic to the nonlinear dynamics itself, and is characterized by exponential sensitivity to initial conditions. Imagine we start a system twice, but from slightly different initial conditions (the difference could be smaller than one's ability to measure, for instance). For non-chaotic systems this leads only to differences in trajectories that grow linearly in time. For chaotic systems, on the other hand, the difference grows exponentially in time so that the state of the system is essentially unpredictable after a very short time. Since we can never know the initial conditions with infinite precision, nor can calculations be done with an infinite string of digits, long term prediction is impossible even though the equations of motion are in principle deterministic [10].

Chaos and integrability represent two opposite extremes of behavior. For a system with N degrees of freedom the corresponding phase space has 2N

dimensions (x_i, p_i). For an integrable system there N independent constants of the motion. For instance, a 1-dimensional system whose Hamiltonian is not explicitly a function of time is integrable because the energy is always a constant of the motion. If the Hamiltonian is explicitly time dependent, or if one considers a 2-dimensional system, the possibility for chaos exists even for such simple cases. If a bounded system is integrable it is quasiperiodic in its time evolution and cannot be chaotic. Quasiperiodic means that if you wait long enough after some starting point, the system will become arbitrarily close to that initial starting point an infinite number of times. Although quasiperiodic motion can look highly complicated and seemingly irregular, it cannot be truly chaotic in the sense of exponential sensitivity to initial conditions. Quasiperiodic systems (of which periodic systems are a subset) are characterized by discrete power spectra. Chaotic systems, on the other hand, are characterized by a broad-band continuous component power spectra [10].

1.3 Quantum Chaos

In classical mechanics, exponential sensitivity to initial conditions can be considered a definition of dynamical chaos. In quantum mechanics the situation is quite different, and there are several ways to see this. Naively, the Heisenberg uncertainty principle makes it impossible to consider infinitesimal differences between initial conditions in the usual sense that we mean in classical mechanics. More importantly, we cannot have sensitivity to initial conditions with unitary time evolution. Suppose we consider two states $|\Psi_1\rangle$ and $|\Psi_2\rangle$ whose overlap at time $t = 0$ is

$$|\langle\Psi_1(0)|\Psi_2(0)\rangle|^2 = 1 - \epsilon \tag{1.29}$$

where ϵ is very small. If the time evolution is governed by a unitary operator, as is the case for bound systems

$$\hat{U}(t)|\Psi_1(0)\rangle = |\Psi_1(t)\rangle \tag{1.30}$$

$$\hat{U}(t)|\Psi_2(0)\rangle = |\Psi_2(t)\rangle \tag{1.31}$$

the overlap at time t is then

$$\begin{aligned} \langle\Psi_1(t)|\Psi_2(t)\rangle &= \langle\Psi_1(0)|\hat{U}^\dagger(t)\hat{U}(t)|\Psi_2(0)\rangle & (1.32)\\ &= \langle\Psi_1(0)|\hat{I}|\Psi_2(0)\rangle & (1.33)\\ &= \langle\Psi_1(0)|\Psi_2(0)\rangle & (1.34) \end{aligned}$$

Thus we do not see an exponential sensitivity to initial conditions in state space. Another way to look at it is that for bound quantum mechanical systems the spectrum is discrete and the motion is quasiperiodic and therefore cannot be considered chaotic [11]. This is the case for experiments described in this work. If the evolution operator is non-unitary, which is the case for unbounded systems, the above argument does not hold. In this case there is no general argument ruling out the possibility of chaotic evolution [11]. It is generally accepted, however, that these systems are not chaotic either [12]. Since no current evidence indicates that the time evolution of a wavefunction can exhibit exponential sensitivity to initial conditions [10]; what, then, is meant by the term 'quantum chaos'?

The study of quantum mechanical systems that exhibit dynamical chaos in their classical limit is called 'quantum chaos,' and has attracted a great deal of interest in recent years. What is found are sharp deviations from classical physics, which are nonetheless fingerprints of classical chaos in the quantal behavior. The nature of these fingerprints has been explored in the atom optics experiments described here, involving the study of momentum transfer to a sample of ultra-cold sodium atoms by a time dependent standing wave of light. Most of the interest in quantum chaos is in the semiclassical limit. In the semiclassical limit the mean separation between eigenstates becomes small, approaching the classical continuum. In this case, a multitude of states becomes involved in the dynamics and a rich variety of phenomena are found

to occur. As will be demonstrated in Chapter 4, it is precisely the spacing of eigenstates that determines how the system makes the transition from behavior that can be predicted classically to that which can only be understood with quantum mechanics.

The above discussion barely begins to describe all of the complex issues involved with the field of quantum chaos. Many issues have been glossed over, and many directions of pursuit have been omitted. For example, the behavior of systems considered in this work can be analyzed in terms of properties that are averaged over many states, and can be described in terms of average quantities. On the level of individual eigenstates, however, quantum structures can display apparently random fluctuations which are sensitive to small changes of an external parameter [13]. It is thus possible that exponential sensitivity to parameters of the Hamiltonian, for instance, and not the initial condition may occur in quantum systems [14], but this is beyond the scope of this work. To even cite all of the references in this active field would probably take up more space than the entirety of this thesis. It is hoped, however, that this brief sketch will provide a context into which the experiments described here can be cast.

Theoretical progress in the field of quantum chaos has far outstripped experimental progress, and what is needed are more experimental tests which can viably check theoretical predictions. There are, however, several previous examples of experimental work in this area. From atomic physics, there is the suppression of ionization of Rydberg atoms in microwave fields [15], the stabilization of ground state atoms in intense laser fields [16], experiments involving the spectral distributions of hydrogenic atoms in strong a magnetic field [17] and proposals for driven diatomic molecules [11]. From condensed matter there is Anderson localization [18, 19] as well as proposals for examining the suppression of heating of a Bloch electron in an AC field [20] and for studying driven

Josephson junctions [21]. Examples from mesoscopic physics include magneto-conductance of electrons in billiard shaped structures [22]. Many of the above systems are very difficult to analyze and involve layers of interpretation. In addition certain parameters, such as the amount of dissipation, often cannot be fully controlled. The present work is a very simple one-dimensional system with a high degree of control over experimental parameters. It should be looked at as a textbook test case with which insight can be gained into this and other more complicated systems.

The general approach in the work presented here is to emphasize understanding in terms of simple physical arguments rather than brute force calculations involving minute experimental details. The universal aspects of the physics is emphasized, and the deviations merely lead to small fluctuations about some mean (this is different than the approach of Latka, *et. al.* [23]). Chapter 2 will present the experimental setup required for studying Hamiltonians of the form of Eq. 1.15 in an atom optics realization where time dependence is introduced in the form of either phase or amplitude modulation. Chapter 3 will discuss experimental and theoretical results of phase modulation studies, where the underlying classical phase space is composed of islands of stability and regions of chaos. By varying the modulation index the phase space goes from global stability to chaos and is mixed in between. These studies demonstrate the phenomenon of dynamical localization, which is a key manifestation of quantum mechanics in classically chaotic systems. This effect is a quantum suppression of diffusion in phase space in a classically chaotic system. It is thought to be responsible for many physical phenomena including suppression of ionization of atoms in strong fields. Chapter 4 will present the case of amplitude modulation in the form of succinct pulses. This is the first direct experimental realization of the quantum δ-kicked rotor. It is found that momentum spread of the atoms increases diffusively with every pulse until the "quantum break time" after which exponentially localized distributions are ob-

served. Quantum resonances are found for rational ratios of pulse period to natural period. Chapter 5 presents amplitude modulation, only this time in the form of a single pulse. One might ask, can a single-pulse standing wave induce chaos in atomic motion? The answer is yes, and as the duration of the pulse is changed several phenomena are observed including the effects of resonance overlap and the onset of dynamical localization. These effects have significant ramifications for many experiments where an interaction is turned on and off non-adiabatically (such as an atomic beam passing through a standing wave). An estimate for the adiabatic limit is also given for the case of a non-linear potential. Finally, Chapter 6 will discuss possibilities of future directions in the atom optics realization of quantum chaos, including preliminary studies of noise-induced delocalization.

Chapter 2

Experimental Realization

2.1 Overview

The experimental study of time-dependent interactions discussed in Chapter 1, consists of three important components: initial conditions, interaction potential, and detection of momentum, which will be described in Sec. 2.2, Sec. 2.3, Sec. 2.4, respectively. These steps occur as a computer controlled sequence, as shown in Fig. 2.1 and Fig. 2.2. The sequence in Fig. 2.2 measures the momentum of the atoms after the time dependent interaction. It is repeated with a different interaction pulse each time, alternating with the sequence of Fig. 2.1 with no interaction pulses as a monitor of the initial momentum distribution. Computer control will be discussed in Sec. 2.1.1.

The initial conditions consist of ultra-cold sodium atoms trapped and laser-cooled in a standard $\sigma^+ - \sigma^-$ magneto-optic cell trap (MOT) [3], which will be described in detail in Section 2.2. A single-mode dye laser (Coherent 899-21, shown in Fig. 2.3) is intensity stabilized and frequency servo-locked to the red of the D_2 transition in sodium at 589 nm. Optical pumping to the $F = 1$ ground state is prevented by a 1.712 GHz sideband. Approximately 10^5 atoms are trapped in a Gaussian distribution of position ($\sigma = 0.12$ mm) and momentum ($\sigma = 4.6\hbar k_L$ centered at $p = 0$). This is the initial condition for the phase modulated experiments of Chapter 3, where the atoms are in the $F = 2$ state. For the amplitude modulated experiments described in Chapters 4 and

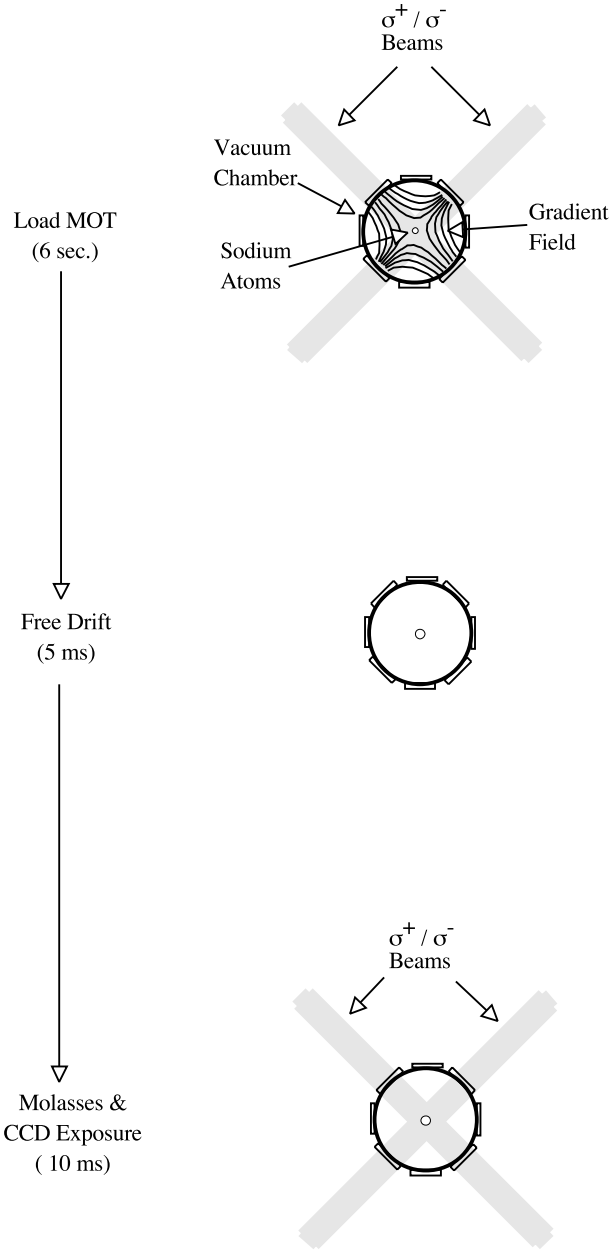

Figure 2.1: The time sequence for a temperature measurement of the initial condition consists of 3 steps: MOT load (about 6 seconds) during which a CCD exposure can be taken, free drift (about 5 ms), and freezing molasses and CCD exposure (about 10 ms).

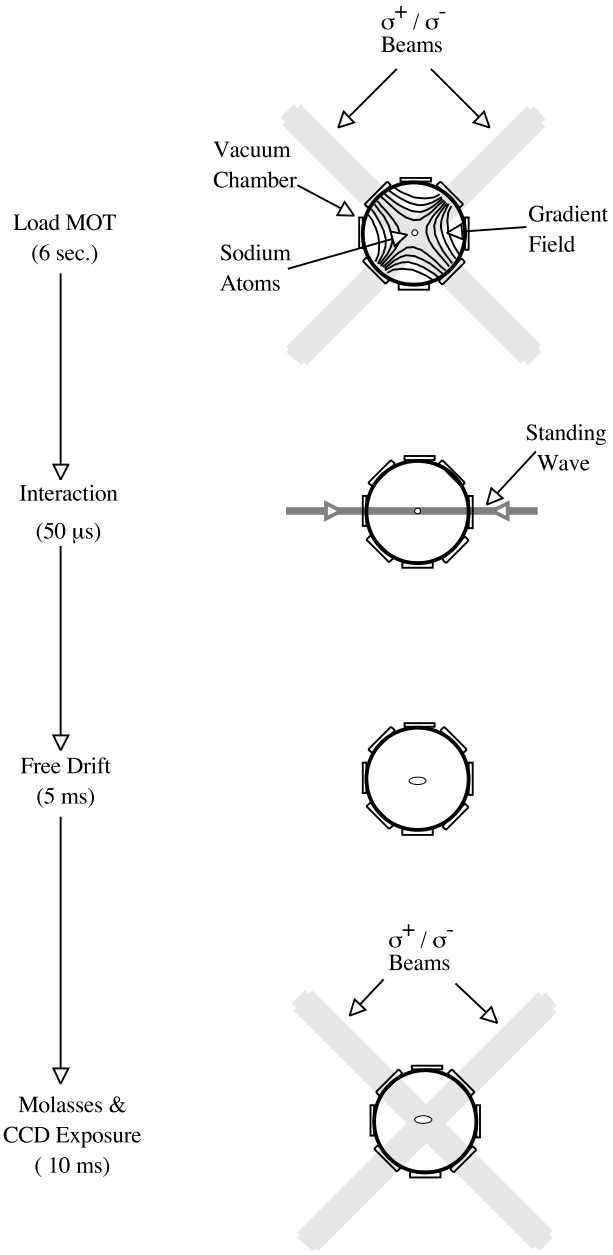

Figure 2.2: The time sequence for a momentum transfer measurement from a time-dependent interaction. The four steps include: MOT load (about 6 seconds) during which a CCD exposure can be taken, interaction with the standing wave (about 50μs), free drift (about 5 ms), and freezing molasses and CCD exposure (about 10 ms).

5, during the last 50 μs of the MOT the sidebands are turned off in order to pump the atoms into the $F = 1$ ground state. After the cooling and trapping stage, the MOT laser beams and gradient coils are turned off.

The interaction potential, which will be described in more experimental detail in Section 2.3, is provided by a second stabilized single-mode dye laser (home-built, shown in Fig. 2.3) which is configured to form a standing wave at the atoms. To ensure a uniform light field the beam is first spatially filtered, and is then focused to a waist ($1/e^2$ radius of intensity) large compared to the atomic sample. Acousto-optic and electro-optic modulators are used to control the amplitude and phase of the standing wave which results in the 1-dimensional Hamiltonian described in Chapter 1. A fast photo-diode detects the amplitude as a function of time, which is then digitized and stored. The low density of the initial condition ensures that the atoms do not interact significantly with one another. The observed effects, therefore, result from individual atoms interacting with the potential. The large number of atoms provides improved signal-to-noise and ensemble averaging.

The detection of momentum is by a novel time-of-flight measurement, which will be described in detail in Section 2.4.3. After the interaction pulse the atoms are left to expand freely for several ms, after which the $\sigma^+ - \sigma^-$ beams are turned back on, this time without the gradient magnetic field. This forms an optical molasses [3] which freezes in the position of the atoms with a strong viscous force, and the resulting atomic fluorescence is recorded in a short exposure on a thermoelectrically cooled charge-coupled device (CCD) as a 2-dimensional image. The image is integrated to form a 1-dimensional distribution along the interaction potential axis. The final spatial distribution, along with the initial spatial distribution and the free-expansion time enable the determination of the momentum distribution of the atoms.

The experiments described here could have been done as an atomic

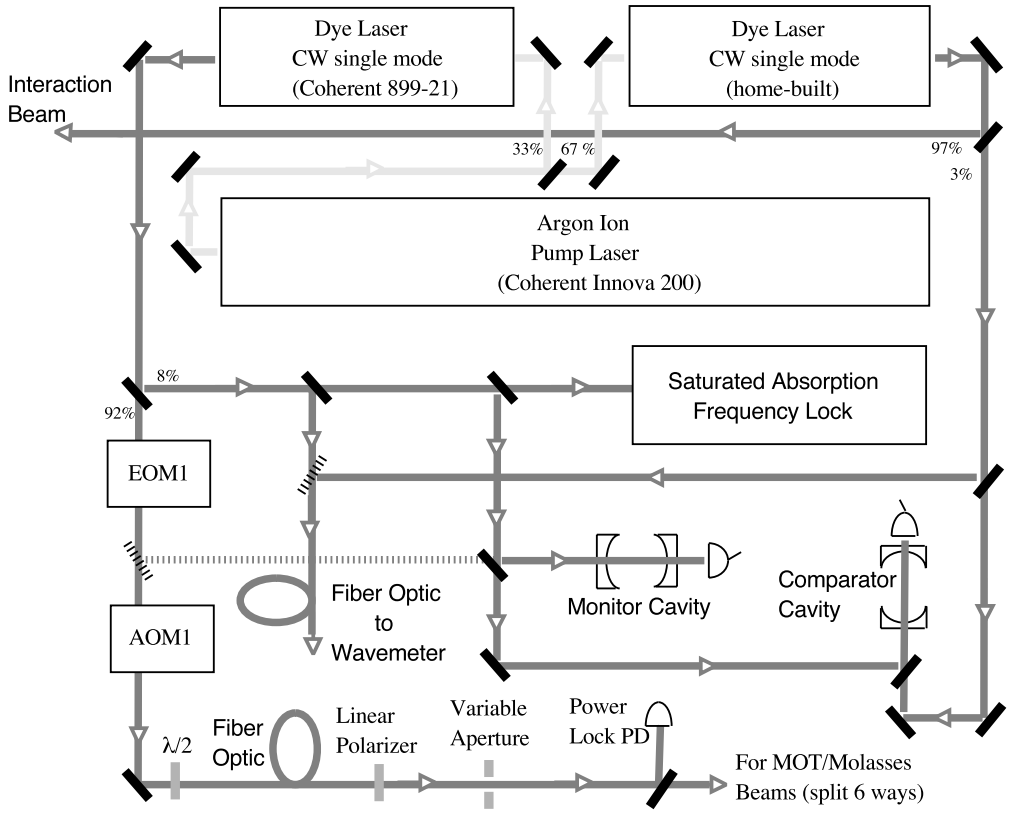

Figure 2.3: Schematic of the laser table. A single argon-ion laser pumps 2 cw single-mode dye lasers. The commercial dye laser (Coherent 899-21) provides the cooling and trapping beams. The home-built laser provides the time-dependent interaction beam.

beam experiment [1], as shown in Fig. 2.4. Initially attempts were made to develop a beam from a "moving molasses." By applying a constant magnetic field, or by frequency shifting one or several of the molasses laser beams, it is possible to create a molasses with a net velocity in the lab frame, which can be used as the source of an ultra-cold pulsed beam. Collimating the atoms in an aperture, the transverse momentum (initial condition) could be reduced significantly from that mentioned above, however, at the cost of signal-to-noise. For a beam experiment the time of interaction with the standing wave would be limited by the transit time of the atoms, necessitating the use of a slow beam. The resulting transverse spatial distribution could then be measured using a freezing molasses, for example. The spatial distribution, transit time, and transit distance could then be used to determine the momentum distribution. Of paramount importance was the realization that the entire experiment could be done in one location, rather than in a beam, with significantly improved signal- to-noise and ease of setup.

2.1.1 Computer Control

The entire experimental sequence (shown in Fig 2.1 and Fig 2.2) is computer controlled. Before the details of the optical setup are presented, a brief description of the computer control will be given. A 486-33 MHz PC is fitted with 3 general purpose National Instruments I/O boards: an AT-MIO-16F-5 board with A/D and D/A converters as well as TTL ports, a PC-DIO-24 board with TTL ports, and a GPIB-PCIIA board for general high-level (IEEE 488.2 standard) control of other devices. National Instruments Lab Windows-DOS compiler/debugger was used to aid in writing C programs. For an approximately 5-fold improvement in timing, the C codes were subsequently compiled with Microsoft C 6.0 into stand-alone executables. This approach proved to be extremely flexible and easy to use. With the use of "panels," control pa-

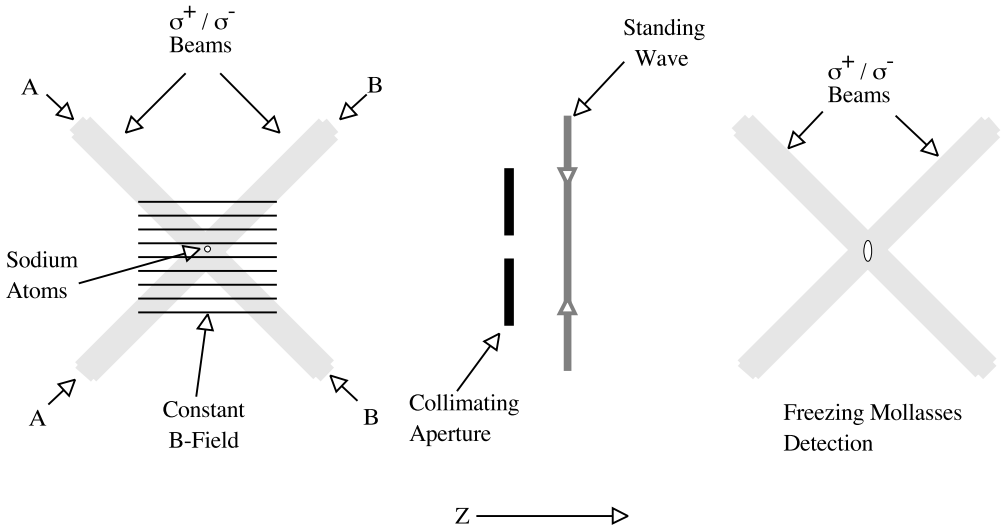

Figure 2.4: These experiments could be performed as a pulsed cold beam experiment. One possible version of this is shown. A MOT is launched either magnetically as shown, or by bringing beams A closer to resonance than beams B. A collimating aperture reduces the transverse momentum (initial condition), before the interaction with the standing wave. Detection could take the form of freezing molasses. The spatial distribution in the molasses could be imaged with the CCD camera and converted into a momentum distribution.

rameters and could be displayed and changed on the computer screen with mouse control. During non-critical points of the experimental sequence, for example during the 6 second loading of the MOT, the computer writes to disk collected data and control parameters from the previous experimental sequence and sets up other device parameters via the GPIB board for the next one. A rack mounted BNC connector patch panel was built to integrate the 50-pin ribbon connector outputs of the AT-MIO-16F-5 and PC-DIO- 24 boards with the experiment.

Timing in these experiments is difficult: control is needed for steps ranging from several nanoseconds to several seconds, including almost all time scales in-between. The counter/timer of the AT-MIO-16F-5 board provides timing. Since this timer is accessed through the C program, however, timing is limited by the time required to perform a single line of computer code, typically about 20μs. To make matters worse, there is timing jitter of order 10μs for a typical sequence of steps. For the phase modulation experiments of Chapter 3, the control hierarchy is shown in Fig. 2.5. For these experiments essentially all of the coarse timing was done by the computer. Fluke-Philips PM 5712/5715 pulse generators were used for finer timing (e.g. delay between AOM4 and AOM5), and to convert TTL pulses into pulses of the proper amplitude and to make them capable of driving 50Ω. For the amplitude modulation experiments of Chapters 4 and 5, the control is shown in Fig. 2.6. Here it was decided, in order to avoid the computer timing jitter problems, to use the computer as a trigger at the beginning of a sequence and then use pulse generators to perform the timing. The sequence of Fig. 2.1 and Fig. 2.2 are then alternated. The advantage of improved timing has to be weighed against the disadvantage of not being able to vary and record parameters automatically. For instance, one may want to vary the free drift time from shot to shot to keep the anticipated spatial extent of the final distribution within an acceptable range. Additionally, since the MOT/molasses conditions change slowly over time, un-

acceptable variations in initial conditions can occur during an experiment if parameters need to be changed by hand and checked on an oscilloscope. Better control of the computer (i.e. disabling the mouse, screen, keyboard, and disk updates during critical timing steps) and/or faster computers are needed. National Instruments' LabWindows-DOS does not support all standard ANSI C commands. LabWindows-CVI is now available which is fully ANSI C compatible, though it is somewhat slower. This should not be a problem, however, if programs are compiled independently as stand-alone executables as before. LabView, though convenient to use, has poor timing characteristics and was not used. Fluke-Philips PM 5712/5715 pulse generators were used for finer timing (e.g. 4 ns rise time to drive AOM6), and to convert TTL pulses into 50Ω pulses of the proper amplitude. Stanford Research Systems programmable DS345 arbitrary waveform generators and Tektronix AWG5105 programmable arbitrary waveform generators were used when programmability was needed, with 25 ns per point resolution. These arbitrary waveform generators were used in 'burst' mode. During non-critical times in the control sequence (during the 6 sec. MOT load time), GPIB programmable waveforms were downloaded into the arbitrary waveform generators. A TTL pulse triggered the pre-programmed burst to occur at a specific instant. If fast rise times are needed, the arbitrary waveform generator in turn triggers a Fluke-Philips 5712/5715 pulse generator. A generic idealized time sequence is shown in Fig. 2.7.

2.2 Initial Conditions: MOT

The initial conditions for these experiments consists of ultra-cold sodium atoms trapped and laser-cooled in a standard $\sigma^+ - \sigma^-$ magneto-optic [3] cell trap (MOT). Approximately 10^5 atoms are trapped in a Gaussian distribution of position $\sigma = 0.12$mm and momentum ($\sigma = 4.6\hbar k_L$ centered at $p = 0$). The photograph in Fig. 2.8 shows the trapped sodium atoms in the center of the

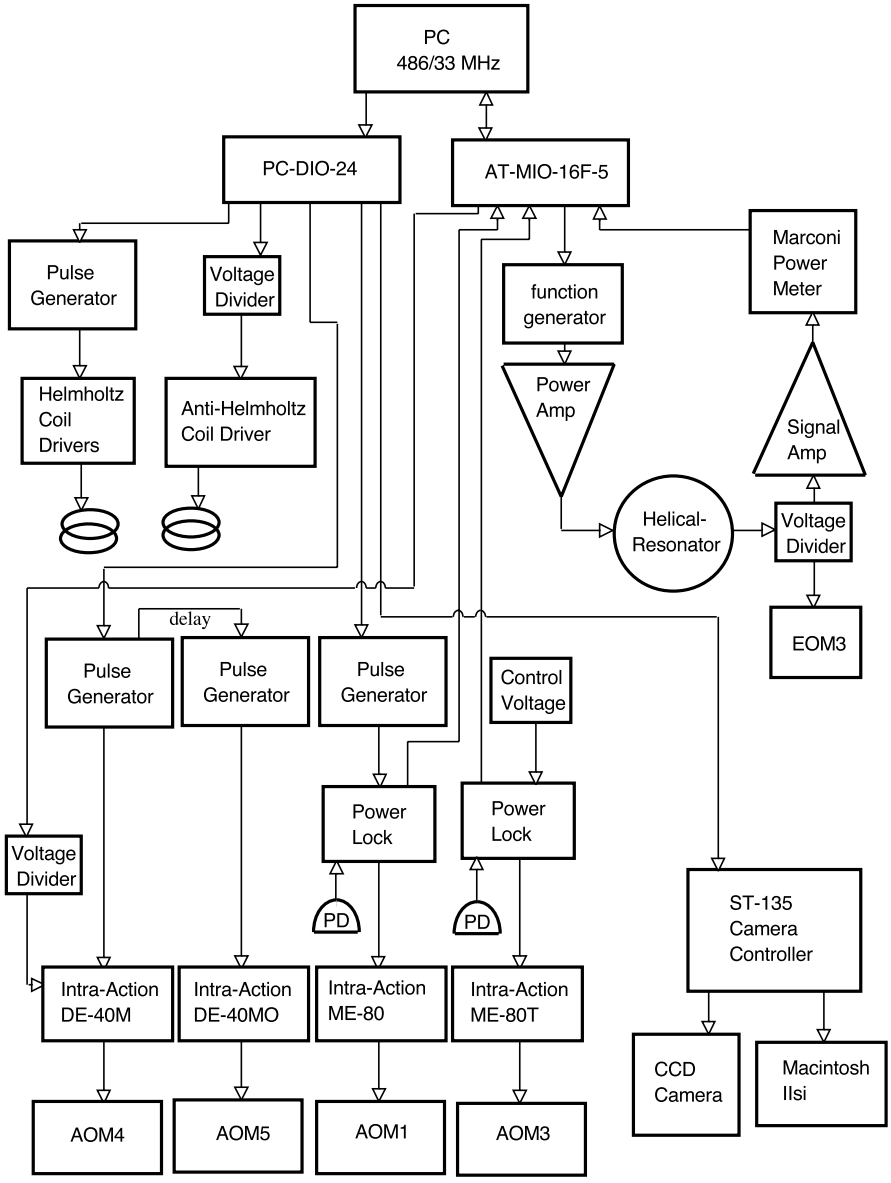

Figure 2.5: Schematic of the control electronics used in the phase modulation experiments of Chapter 3. A 486/33 MHz PC controls hardware and records data with PC-DIO-24 and AT-MIO-16F-5 I/O boards from National Instruments. A Macintosh IIsi controls the CCD that takes the fluorescence profiles of the atomic distribution.

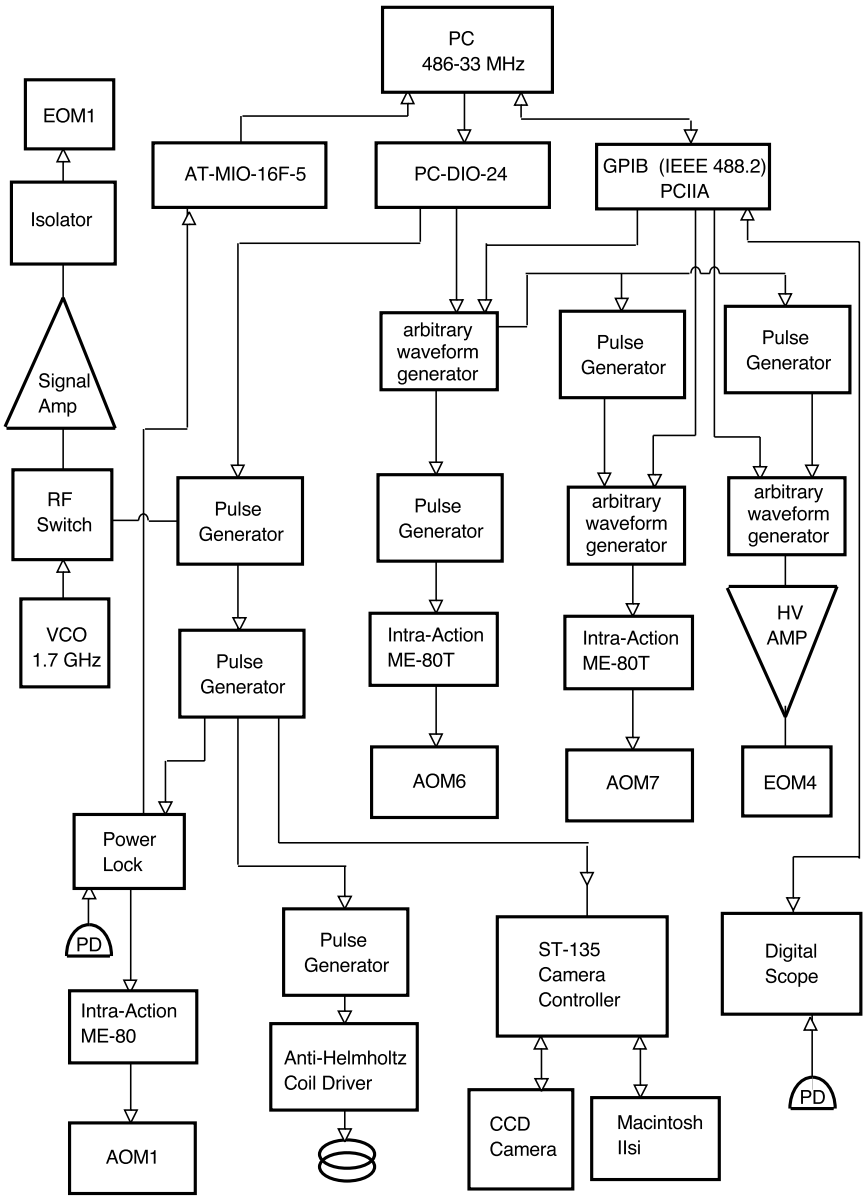

Figure 2.6: Schematic of the control electronics used in the amplitude modulation experiments of Chapters 4 and 5. A 486/33 MHz PC controls hardware and records data with PC-DIO-24, AT-MIO-16F-5, and GPIB I/O boards from National Instruments. A Macintosh IIsi controls the CCD that takes the fluorescence profiles of the atomic distribution.

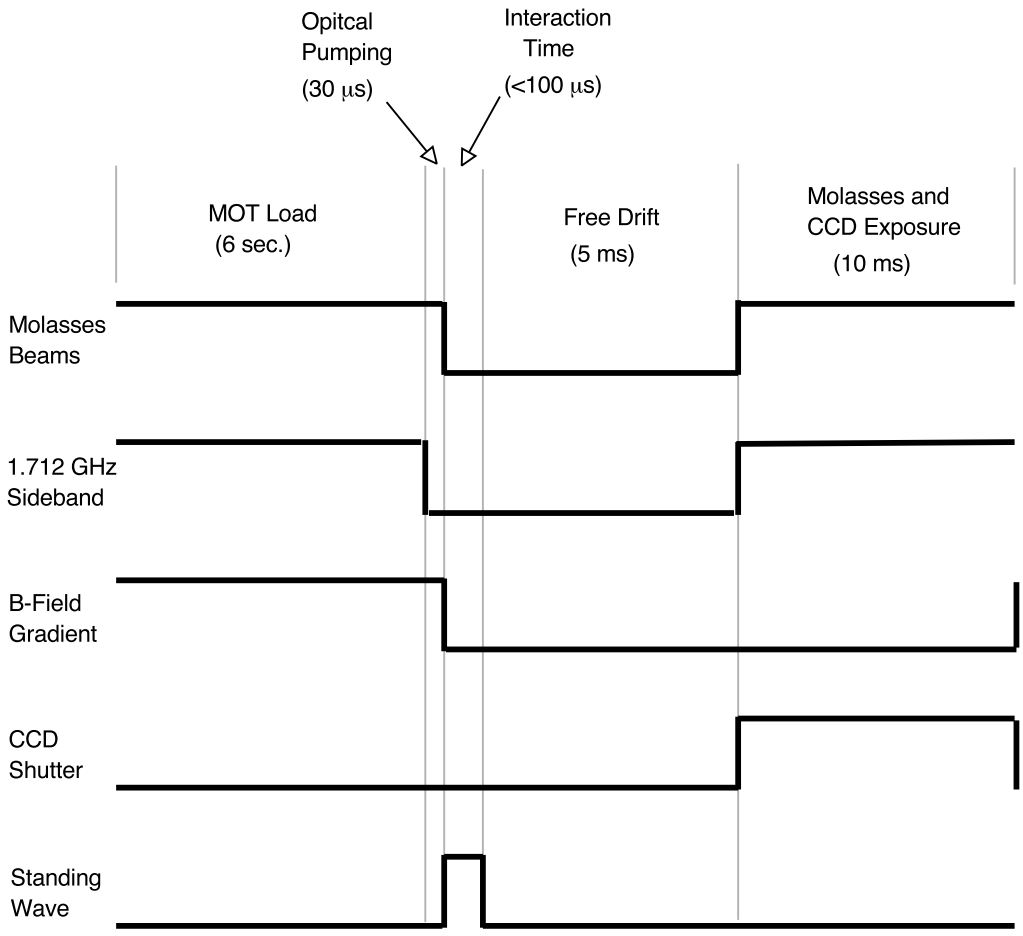

Figure 2.7: An idealized generic time sequence for the experiment. A sequence with the interaction with the standing wave is alternated with one without. This provides a constant check of the initial conditions.

1" front window. Optimization will be described in Section 2.4.2. Longer than minimal load times were used (typically 6 seconds) to ensure consistency from shot to shot. Of importance is the observation that with the proper conditions (low density) the MOT temperature is sufficiently cold that an additional cooling molasses step is not needed before the time dependent interaction beams.

The light for the MOT is produced by a Coherent 899-21 single mode cw dye laser which is pumped by 33% of the output of a Coherent Innova 200 argon ion laser in the multi-line visible mode (no internal prism), as shown in Fig. 2.3. The gain medium is Rhodamine-590 chloride dye pre-dissolved in methanol in ethylene glycol. Approximately 92% of the 800 mW output of the 899-21 is sent through a resonating electro-optic modulator (EOM1), which provides 1.712 GHz sidebands for optical pumping. An acousto-optic modulator (AOM1) is used to control the amplitude of the light which is sent through an Oz Optics polarization preserving single mode fiber. The fiber acts as a spatial filter, and is used to preserve alignment of the six MOT/molasses beams against occasional re-alignment of the laser. Feedback from a photodiode on AOM1 provides a power lock for light reaching the atoms. The circuit in Fig. 2.9 is used for the power lock, which is able to maintain power stability to within about 1%. A fast CMOS switch enables a fast turn on/off of the resonant light, within 40 μs. The laser beam is split six ways as three orthogonal counter-propagating pairs. Quarter-wave plates convert the linearly polarized light into circularly polarized light of the proper helicity (see Section 2.2.1) with a diameter of about 1" at the cell. Since a beam experiment was originally envisioned, independent control of the six beams was necessary. This also makes it easy to match intensities. One future improvement would be to split the power into three orthogonal beams that are retro-reflected back through the chamber.

Another Oz Optics polarization preserving single mode fiber optic brings

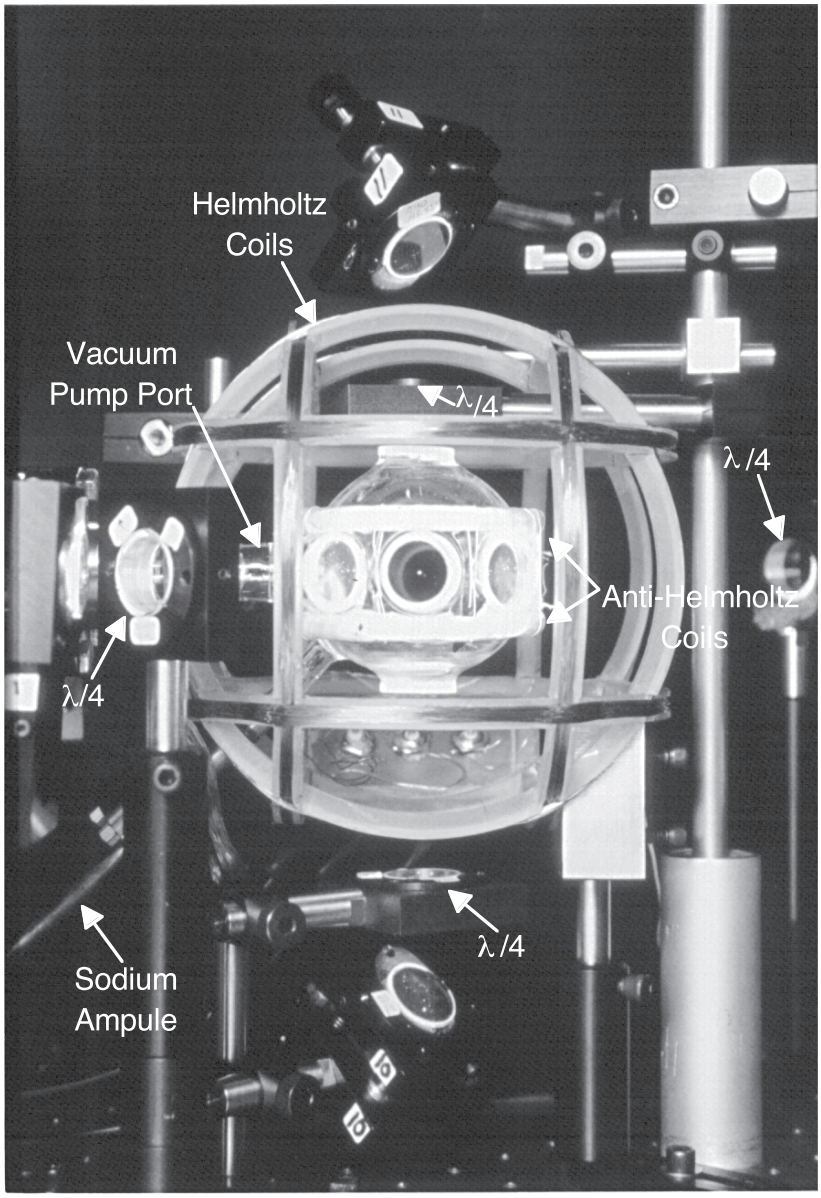

Figure 2.8: The vacuum chamber is a 3" diameter quartz sphere with nine 1" diameter windows. The spot in the center of the central window is the fluorescence from approximately 10^5 sodium atoms at the convergence of 6 circularly polarized laser beams and a magnetic field gradient.

a small portion of the laser light to a traveling Michelson interferometer wave-meter, which will be described in Section 2.3.2. Using the wave-meter, the frequency of the 899-21 is adjusted to within 50 MHz of resonance. FM saturated-absorption spectroscopy is used to fine tune and lock the laser to the proper frequency as discussed in Section 2.2.5.

2.2.1 MOT Theory

The most widely used trap for neutral atoms is the MOT or magneto-optic trap which involves both cooling and trapping effects. The cooling mechanism which enables the low-velocity tail of the room temperature Boltzmann distribution to be trapped, will be discussed in Sec. 2.4.1. The basic magneto-optic trap configuration is shown in Fig. 2.10. Three pairs of mutually orthogonal counter-propagating beams intersect at the center of a pair of anti-Helmholtz gradient magnetic field coils (see 2.2.3). The magnetic field gradient shifts the Zeeman sub-levels of the atoms and creates a spatially dependent imbalance in the scattering from the counter-propagating beams. The spontaneous-scattering imbalance imparts a net force on the atoms towards the center of the trap.

Consider an atom to the right of the origin along the x-axis in Fig. 2.10. The magnetic field Zeeman-shifts the otherwise degenerate sublevels. It can be seen that the beam coming from the positive x direction has angular momentum parallel to its direction of motion and, projected on the quantization axis of the atoms, acts as σ^- light. The Zeeman-shift is small compared to the red detuning of the lasers. Even still, this induces the beam coming from the positive x direction (indicated by thick σ^- arrow) to be closer to resonance and hence to scatter more than the beam from the opposite direction whose projection is σ^+. This scattering imbalance pushes the atom towards the center of the trap. If, on the other hand, the atom were to the left of the origin along the x-axis, the level shift is opposite. Now the beam coming from the

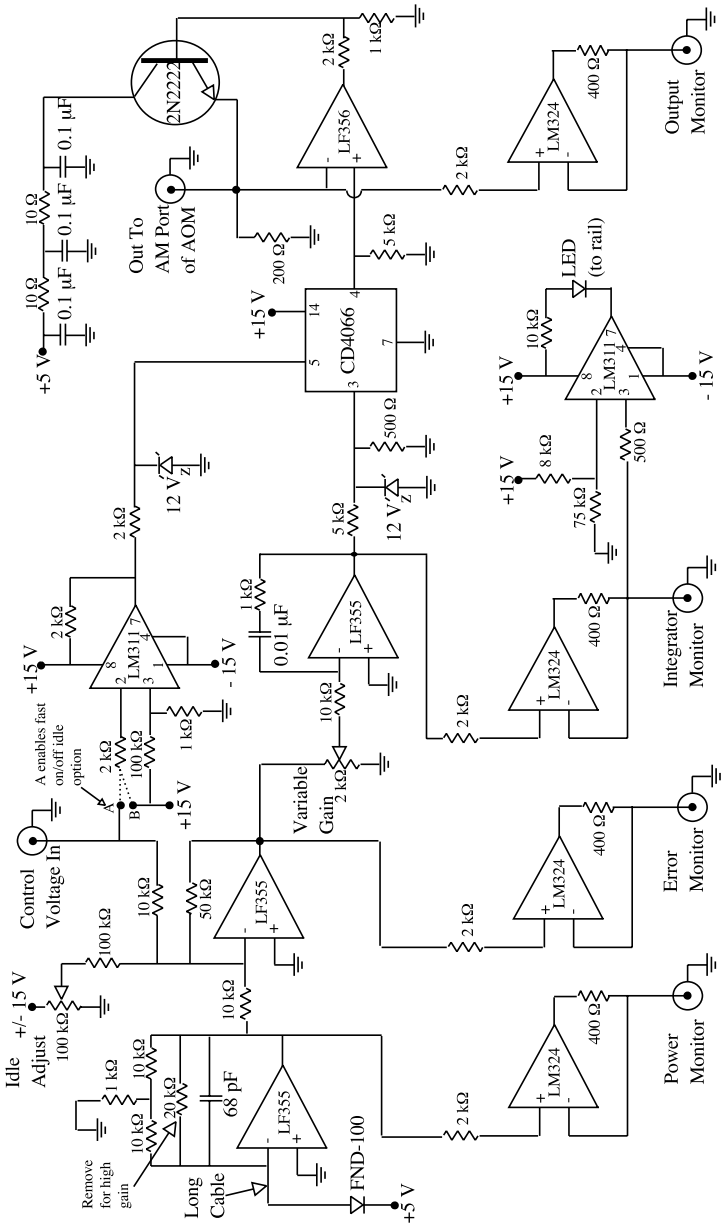

Figure 2.9: Schematic of the laser power lock circuit. The signal input is photocurrent from an FND-100. The output provides feedback to the amplitude modulation port of AOM1. A control voltage provides the level to lock to, and enables on/off control.

negative x direction (indicated by thick σ^+ arrow) scatters more strongly and the atom is again pushed towards the center of the trap. The same is, of course true for the y-axis. For the z-axis, the handedness of the light is switched (angular momentum antiparallel) since the direction of the magnetic field is opposite, and we find a similar restoring force towards the center of the trap. This configuration is often called $\sigma^+ - \sigma^-$ since each counterpropagating pair has this effect on the atoms along its axis when they are not at the center of the trap. The velocity dependent cooling effect that these beams have will be discussed in Sec. 2.4.1. Much theoretical and experimental work has been done to characterize MOTs by others. For the purposes of this work, however, the details are not important. It simply provides a cold, spatially localized initial condition for the experiment. Future improvements to these experiments should include the reduction of the initial spatial and momentum distributions. Laser cooling and trapping techniques for doing both are available.

2.2.2 Trap Envelope

The trap envelope, shown in Fig. 2.8 consists of a quartz sphere of diameter 3" with nine 1.0" diameter fused silica windows attached directly to the sphere by Gene Lutter of G. L. Glassblowers, Longmont, CO. It is done by heating a frit material made of fused silica powder with impurities to lower the melting point below that of fused silica (can be obtained from Vitta Corporation). A quartz-to-metal seal serves as a pump port and connects the sphere to a $2\frac{3}{4}$" Conflat section with a 20 l/s star-cell vac-ion pump and a nude Bayert-Alpert vacuum gauge. Another quartz-to-metal seal connects to a mini-Conflat with a copper pinch-off tube that has been pinched shut (visible in Fig. 2.8). Inside the copper tube is a sodium ampoule which has been vacuum distilled to remove the argon that comes with commercial pure sodium and to purify it further. The entire system was cleaned and then vacuum baked at 300 C for 3 days

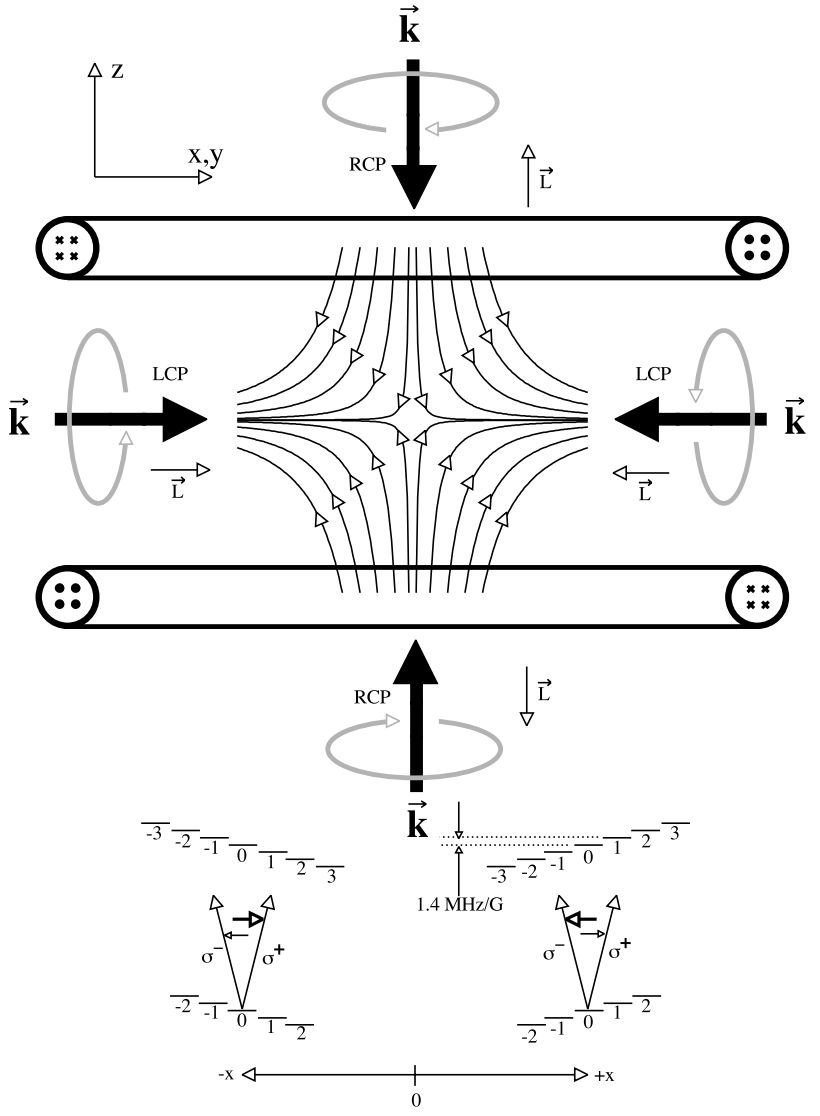

Figure 2.10: The MOT is formed by the combination of six circularly polarized laser beams and a magnetic gradient formed by an anti-Helmholtz coil pair. Wavevectors ($\vec{k}$) and angular momentum ($\vec{L}$) as well as the sense of rotation of the electric field for right circular polarized light (negative helicity) and left circular polarized light (positive helicity) are indicated. The gradient magnetic field lines from the anti-Helmholtz coil pair are shown as is the subsequent Zeeman shift of sodium's M_f magnetic sublevels (μ_B/h = 1.4 MHz/G).

into a 150 l/s vac-ion pump. After the bake, the copper tube containing the glass sodium ampoule was crushed from the outside with pliers, exposing the sodium to the ultraclean vacuum chamber. The entire system is then sealed off from the large pump. The chamber is maintained at a base pressure of $5\text{x}10^{-10}$ Torr. The partial pressure of sodium is roughly its room temperature vapor pressure of about 10^{-11} Torr. The advantages of this quartz sphere cell are ease of access, small size, and simplicity. Its primary disadvantage is that the 900 C frit process precludes the use of anti-reflection coated windows. The 4% per surface reflection caused fringes in the laser beams. In addition, spurious frit material caused light scatter from the windows. Efforts to make a new cell with indium-sealed 2" diameter anti-reflection coated windows is currently underway, and should provide substantial improvement in optical quality at the expense of higher base pressure.

2.2.3 Magnetic Field Coils

A magnetic field gradient is provided by the anti-Helmholtz (current in opposite directions) coil pair shown in Figs. 2.8 and 2.10. For a given coil radius r and current, the maximum magnetic field gradient occurs when the coil separation s is equal to the radius ($s = r$) called the 'anti-Helmholtz' configuration. Here $r = 4$ cm . If we call the coil axis the z-axis, then by symmetry we know that the gradient in the x and y directions at the center are equal

$$\frac{\partial B_x}{\partial x} = \frac{\partial B_y}{\partial y} \tag{2.1}$$

Since we know that $\vec{\nabla} \cdot \vec{B} = 0$ it follows that at the center, independent of coil separation

$$\frac{\partial B_z}{\partial z} = -2\frac{\partial B_x}{\partial x} = -2\frac{\partial B_y}{\partial y} \tag{2.2}$$

For the phase modulated experiments discussed in Chapter 3, $\frac{\partial B_z}{\partial z} = 10$ G/cm at the center of the coils. To increase the MOT depth, the gradient was increased

to about $\frac{\partial B_z}{\partial z} = 15$ G/cm for all of the amplitude modulation experiments of Chapters 4 and 5. Gradients steeper than this were not sought because the coils are directly against the quartz sphere, causing significant heating beyond 1.5 Amps. An obvious improvement would be to have some distance between the coils and the quartz cell. The current was locked via the circuit shown in Fig. 2.11 based on a Burr Brown OPA541BM high current (up to 10 Amp.) op-amp. The advantage of locking to the current rather than the voltage is that the magnetic field can be turned on and off rapidly (in 200 μs) without ringing. It is the current, after all, that is of importance for magnetic fields. A 20-turn pot is used for fine adjustment of the off state. Coils are switched on and off by an external signal, the level of which determines the current that the coils lock to. It is extremely important to ramp off the gradient fields in the absence of the MOT beams, otherwise unwanted spurious atomic motion occurs. It is not, however, necessary to delay the time dependent interaction beams until the gradient is entirely off, since the Zeeman shifts of sodium in these fields (1.4 MHz/Gauss, where the atoms experience less than 1 Gauss, typically) is small compared to the detunings of this light (several GHz).

Since both the MOT and molasses are extremely sensitive to magnetic fields, a constant magnetic field that nulls out any stray fields from external sources is provided by the three orthogonal pairs of Helmholtz (current in same directions) coils shown in Fig. 2.8. When two coils of radius r separated by a distance s are such that $r = s$ (the Helmholtz condition) then at the center

$$\frac{\partial B_z}{\partial z} = \frac{\partial^2 B_z}{\partial z^2} = \frac{\partial^3 B_z}{\partial z^3} = 0 \tag{2.3}$$

and similarly for B_x and B_y. Here $r = 8$ cm. The current lock is the same as that for the anti-Helmholtz coils (shown in Fig. 2.11). Here no signal is input and the 20-turn pot sets the constant value. Initial external field nulling to about the 1 mG level was done with the aid of a 3-axis Gauss meter (Barrington Model MAG-03MC) in the absence of the vacuum cell. Moving the vacuum

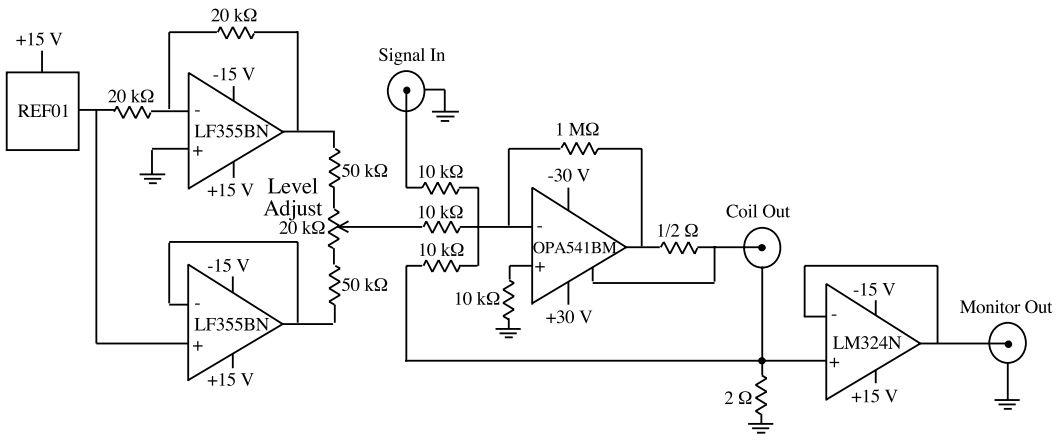

Figure 2.11: Schematic of the Helmholtz (current in same direction) and anti-Helmholtz (currents opposing) magnetic coil pairs. The circuit locks to current, not voltage, in the coils. The signal in and the level adjust voltages add. One driver is used per coil pair. The LF355BN voltage reference is common to all 4 (three Helmholtz pairs, one anti-Helmholtz pair) drivers used.

chamber back into place inevitably adversely affects the fields. Fine nulling based on an *in situ* measurement on the atoms will be described in Section 2.4.2. The novel freeze-in time-of-flight measurements described here would not be possible without this fine field nulling. This driver (Fig. 2.11) was designed with magnetic beam launching, in the form of a moving molasses, in mind (see discussion in Section 2.1). Therefore it has the capability of being pulsed rapidly. With the 0.5Ω current limiting resistor removed, up to 10 Amps could be switched rapidly. One improvement in field uniformity would be the use of μ-metal shielding.

2.2.4 1.7 GHz Sidebands

The electro-optic modulator shown in Fig. 2.3 which imposes 1.712 GHz sidebands for optical pumping uses a resonating microwave cavity to produce a large sinusoidal electric field across a 3x3x25.4 mm non-linear $LiTaO_3$ crystal,

as shown in Fig. 2.12. The crystal, from Crystal Technology, is broad-band anti-reflection coated. With 28 dBm of microwave power, up to 50% intensity sidebands could be induced, though 15% was found to be optimal for a cold MOT. The sidebands and carrier could be observed with a scanning Fabry-Perot cavity. Originally a smaller 1x1x25.4 mm crystal was used in a traveling wave modulator. The advantage of a smaller crystal is that a smaller voltage is required, and the crystal was simply part of a non-resonant 50Ω transmission line [24]. Unfortunately the smaller crystal also meant higher optical intensity, and as a consequence had an unacceptable amount of photo-refractive damage from the 800 mW of 589 nm light. One option would be to use MgO doped $LiNbO_3$, which is reported to be less susceptible to photo-refractive damage [25]. We opted to simply use a larger $LiTaO_3$ crystal. After about 1/2 year of use, mild photo refractive damage did occur in the larger crystal. Annealing with a U.V. lamp overnight corrected this problem.

The resonator was simply made from a piece of 0.13 mm thick copper foil that was bent to form a split-ring cylindrical resonator, and held in place around the crystal (see Fig. 2.12). A formula, which assumes that the resonator diameter is much larger than the crystal width (valid at lower frequencies), can be used to give the approximate diameter for the desired frequency [26, 27, 28, 29, 30]. The frequency can be fine tuned by sliding the crystal in and out radially, by bending the resonator slightly, or by inserting a small electrically isolated metal rod into the resonator. A loop antenna is used to couple power into the resonator. In order to achieve critical coupling, it was necessary to make the antenna slightly larger than the cross section of the resonator and crystal. By moving the antenna up to the resonator, it was possible to go from under coupled through critical coupling to over coupled. At the critical coupling, 35 dB of return loss (VSWR = 1.03) was achieved, which was measured using a directional coupler to look at the reflected rf power. The resonator used here has a Q of 170 which was measured by monitoring the

reflected rf power as a function of frequency with a Mini-Circuits ZFDC- 10-5 directional coupler, or by monitoring rf pick-up as a function of frequency on a 50Ω current loop weakly coupled to the resonator. To get a Q this high it was necessary to minimize the amount of lossy dielectric support structure present, and to partially enclose the modulator in a grounded copper box. Substantial heating occurred in the resonator, resulting in its deformation and frequency shifts. Forced-air cooling was used to minimize this effect. Significant improvements in Q may be possible if gold plated OFHC copper were used for the resonator. The rf signal is provided by an Avantek VTO-9130 VCO chip, which can be blocked in 2 μs with a Vortex SKW-A01 rf switch as shown in Fig. 2.6. This signal is amplified to 28 dBm by a Mini-Circuits ZHL-42 power amplifier. A Sierra Microwave Technology SMT 1CY63 isolator protects the amplifier against rf reflections in the event that the antenna is bumped out of position or if the frequency should drift off resonance. In its off state the rf switch could provide 30 dB power isolation, reducing the laser sideband power from 15% of the carrier to 10^{-4} of the carrier.

If the sidebands are left on for the duration of the MOT, the atoms were measured to be predominantly in the F=2 ground state sublevel. If, on the other hand, the sidebands are turned off 50 μs before the MOT light is turned off, the population is measured to be predominantly in the F=1 ground state (see Fig. 2.13). Population measurements were performed by observing the effect of a standing wave in heating an atomic sample. By trying several detunings the populations could be inferred. Another method was to monitor MOT spontaneous emission as a function of time after the sidebands have been turned off with a PMT.

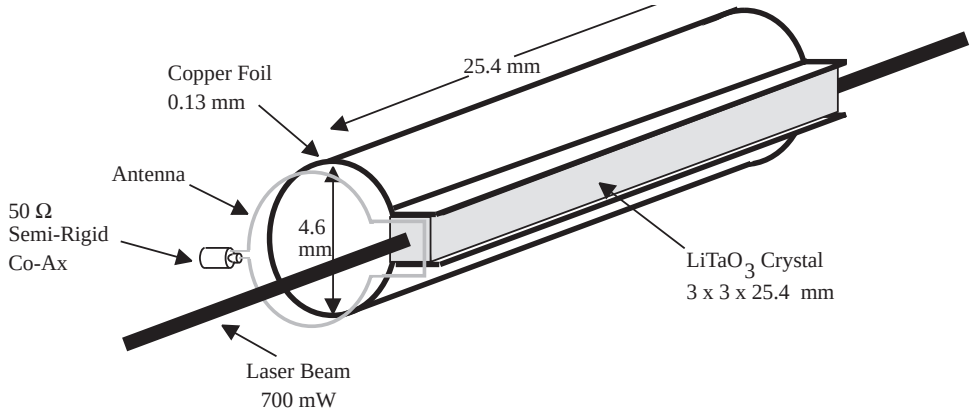

Figure 2.12: Schematic of the 1.7 GHz electro-optic modulator. A critically coupled antenna provides power for a resonating split ring rf resonator which provides an oscillating electric field for the $LiTaO_3$ crystal.

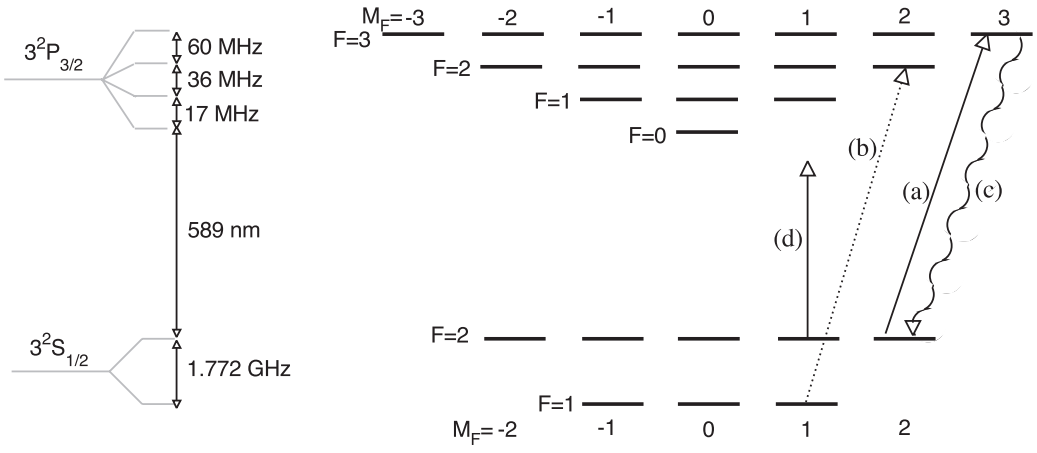

Figure 2.13: Term Diagram for the Sodium D_2 line. For the $3S_{1/2}$ state I = 3/2 and J = 1/2, and since F = J + I, F = 1,2. For the $3P_{3/2}$ state J = 3/2 so F = 0, 1, 2, 3. The magnetic sublevels are $-F \leq m_F \leq F$. Representative examples of (a) the cooling and trapping beams, (b) the optical pumping sideband, (c) spontaneous decay, and (d) the interaction Hamiltonian are shown.

2.2.5 Saturated Absorption FM Spectroscopy

The 899-21 laser was frequency locked 60 MHz to the blue of the $(3S_{1/2}, F = 2)$ to $(3P_{3/2}, F = 3)$ transition in sodium with a FM lock scheme [31, 32, 33] as shown in Fig. 2.14. Upon being downshifted 80 MHz by AOM1, the light impinging on the atoms is 20 MHz to the red of the transition. A probe beam at the laser frequency ν_L is frequency modulated at 5.646 MHz with a small modulation index by EOM2, which is a Con-Optics model 370 phase modulator driven by a magnetically coupled helical resonator of Q = 104 which is supplied with -4.1 dBm rf power. The probe beam counter-propagates with a saturating pump beam in a vapor cell. The probe beam is linearly polarized perpendicularly to the plane of the page, and is reflected by BS2 into a back-biased FND- 100 photo diode. The photo diode signal is amplified by two Mini-Circuits ZFL-500LN amplifiers. The saturating pump beam is reflected by BS2, is first-order downshifted by an 80 MHz Isomet 1205C-1 (AOM2) driven by an Isomet 232A-1 driver, passes through a quarter wave plate, is retro reflected, passes again through the quarter waveplate, and is again first-order down shifted by AOM2. The result is a pump beam which is linearly polarized parallel to the plane of Fig. 2.14 at ν_L - 160 MHz, which passes through BS2 and overlaps the probe beam in the vapor cell.

The beat note between the upper FM sideband and carrier is 180° out of phase with the beatnote between the lower sideband and carrier. When the laser frequency is far from a resonance of the vapor species the destructive interference between the sidebands results in no beatnote at 5.6 MHz. A slow (approx. 1 Hz) sweep was fed into the laser external scan, and the signal was observed on a scope. When the laser frequency is near a resonance the polarizability of the vapor is strongly dependent on frequency, and the balance between beat notes is lost. The result is a dispersive signal at 5.6 MHz that follows the broad Doppler profile. Very near resonance, the pump and probe

beam interact with the same velocity class of atoms and a strong feature with the width of the natural linewidth is seen. Dispersive lineshapes are obtained by using a Mini-Circuits ZP10514 mixer to mix to 23 kHz the photodiode output with the properly phase-shifted oscillator at 5.6 MHz, via a Mini-Circuits ZDC-10-01 coupler. The broad Doppler profile can be separated from the narrow dispersive lineshapes by chopping the pump beam at 23 kHz, and detecting the mixer output synchronously with the chop frequency by use of an EG&G Model 5204 lock-in amplifier to demodulate (mix to DC) the signal with a 0.1 Hz time constant. Because the pump is at ν_L and the probe is at ν_L - 160 MHz, the dispersive signal occurs at ν_L - 80 MHz. This was done to compensate for the frequency shift imparted by AOM1, which down-shifts the light to the atoms by 80 MHz. By locking to the proper dispersive lineshape's zero-crossing, and by choosing the proper frequency of AOM2 with respect to AOM1, a zero-crossing occurred 20 MHz to the red of the $(3S_{1/2}, F = 2)$ to $(3P_{3/2}, F = 3)$ transition in sodium. Slight adjustments could be made by setting a non-zero DC offset in the lock-in amplifier.

The phase of the 5.6 MHz reference frequency and the phase of the lock-in were adjusted to maximize the demodulated signal. Since the signal at 5.6 MHz is extremely small (of order -50 dBm), spurious electrical pick-up can be a problem. The 899-21 frequency was servoed to the zero-crossing of the saturated absorption feature by using the 'External Scan' on the laser controller, which feeds into the reference cavity servo. The lock circuit used is shown in Fig. 2.15. The time response of this lock scheme is limited by the speed of the 899-21 servo galvo. An improvement, which is planned, is to feed back into the high-speed 'tweeter' piezo in the laser cavity, which would greatly enhance the speed of the lock-loop [34].

For diagnostics, a room temperature iodine vapor cell was used. The cell is 10 cm long and 2.5 cm in diameter and was purchased from Opthos

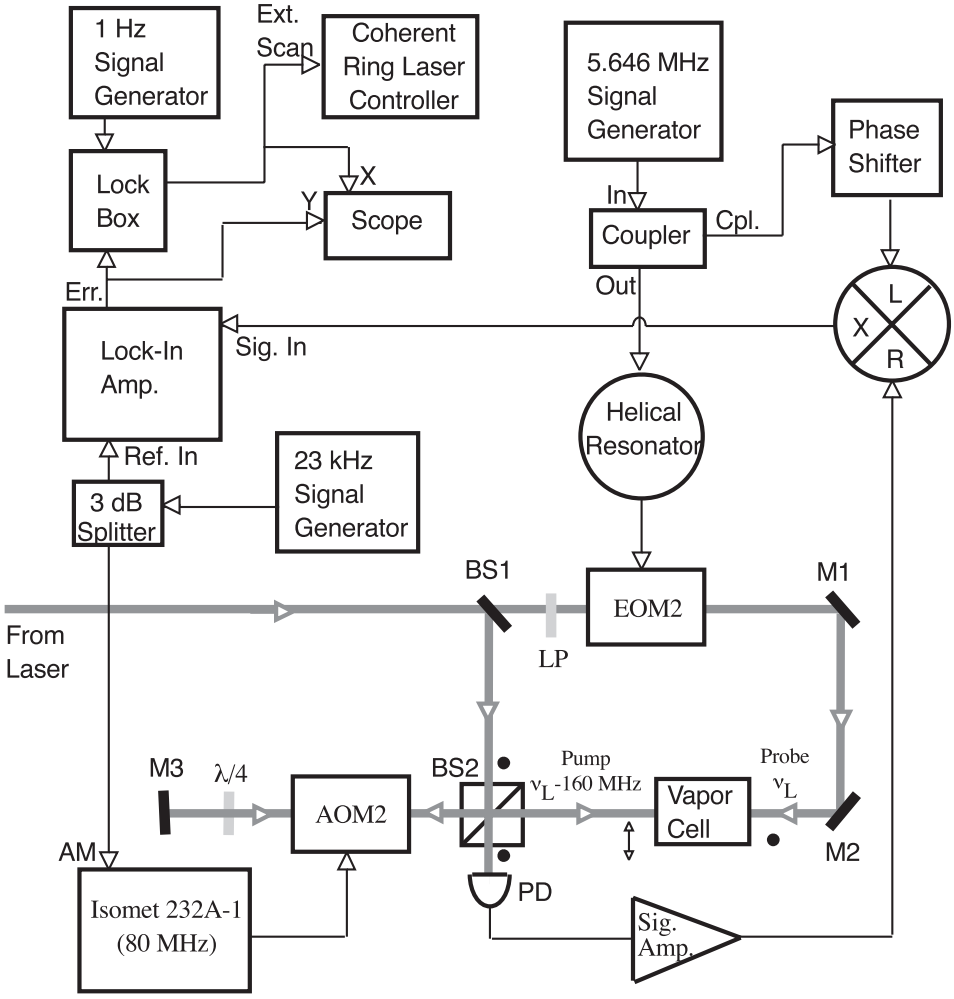

Figure 2.14: Saturated absorption FM spectroscopy frequency lock scheme. Counter-propagating pump and probe provide sub-Doppler frequency resolution. Note the overall shift in frequency of 80 MHz.

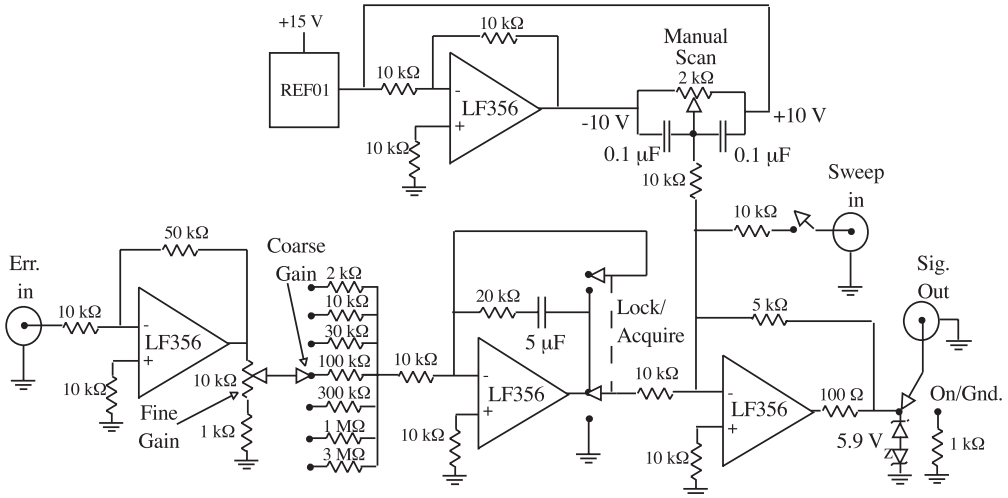

Figure 2.15: Schematic of the saturated absorption FM spectroscopy laser frequency lock box. The error signal comes from the lock-in amplifier. The lock signal output goes to the external sweep of the Coherent ring dye laser controller. A switch allows for the laser frequency to be slowly sinusoidally or manually swept for setup. Manual adjustment is used to center on the desired spectral feature.

Instruments along with an iodine absorption atlas [35, 36]. In this case the pump was 1.7 mW in a beam with a $1/e^2$ intensity radius of 0.33 mm, and the probe was 1.6 mW with the same radius. The advantage of iodine is its large signal and numerous spectral features. The sodium cell was used to lock the laser frequency for the experiments. The sodium cell was vacuum distilled from a commercial ampoule. The cell is similar in size to the iodine cell and was maintained at about 127 C. All but a small hole at each end was insulated to reduce sodium vapor condensation where the laser enters the cell. In this case the spot sizes remained the same, but the intensity was reduced to 0.47 mW in the pump and 0.42 mW in the probe to avoid power broadening the sub-Doppler features. To improve signal-to-noise, a larger laser spot size with more power, a longer vapor cell, or a hotter oven could be used. The intensity, however, cannot be increased or power broadening will wash out the sub-Doppler features.

2.2.6 Scanning Fabry-Perot Cavities

Two scanning Fabry-Perot cavities were used, as shown in Fig. 2.3. The monitor cavity was made from 2 mirrors with 99% reflectivity with a 5 cm radius of curvature adjusted to be confocal. Its cavity length was piezo-swept with a Trek model 601B-2 H.V. amplifier. The output was monitored with a photodiode on a dedicated scope. It has a 1.5 GHz free-spectral range (figure-8 or ring configuration) with a finesse of about 300. This cavity was extremely useful for laser diagnostics. A kinematic mount could be inserted to measure the relative intensity of the 1.7 GHz sidebands (shown as a dotted line in Fig. 2.3). The comparator cavity was similar to the monitor cavity but has 5 cm radius of curvature mirrors which were spaced by 1.8 cm (not confocal), resulting in a free spectral range of 8.3 GHz with a finesse of 200. Light from both the 899-21 and the home-built dye laser were simultaneously monitored by this

cavity. The 899-21 was servo locked 20 MHz to the red of the $(3S_{1/2}, F = 2)$ to $(3P_{3/2}, F = 3)$ transition in sodium. The home-built laser was brought within one free spectral range of the comparator cavity of the sodium transition with the aid of the wavemeter. Then it was possible to monitor relative detunings of the two lasers, if the non-linearity of the piezo scan was taken into account by scanning the 899-21 in calibrated amounts.

2.3 Interaction Potential

2.3.1 Home Built Dye Laser

The interaction potential beam was provided by a home-built dye laser based on a design by Jim Bergquist at NIST in Boulder, CO [2]. A schematic is shown in Fig. 2.16. This laser is designed for low pump threshold, high efficiency, and frequency stability. The cavity is supported by four 1" diameter 36" long Invar rods, whose centers are separated by 7.5" horizontally and 5.5" vertically. Optical elements are held in place by aluminum supports which are affixed to the rods. All optical adjustment screws are 1/4" - 80 screws made by Lees Optical. It is pumped by 66% of the output of a Coherent Innova 200 argon ion laser in the multi-line visible mode (no internal prism), as shown in Fig. 2.3. The gain medium is Rhodamine-590 chloride dye in ethylene glycol, pre-dissolved in methanol. The jet nozzle was purchased from Coherent. Typical output is 1 W single mode with 66% of 19 W multi-line visible pump power.

The optical cavity is a 4-mirror folded geometry, but unlike the Coherent 899-21 it does not need an astigmatic compensation rhomb. The optical diode, birefringent (Lyot) filter and intracavity assembly were purchased from Coherent and are identical to those in the 899-21 [37]. Like the Coherent, there is a fast scanning peizo. Unlike the Coherent, it uses a slow scanning piezo instead of a tipping Brewster plate. The thick etalon lock is similar to that used in the 899-21 where the intensity measured on PD1 is fed back into the thick

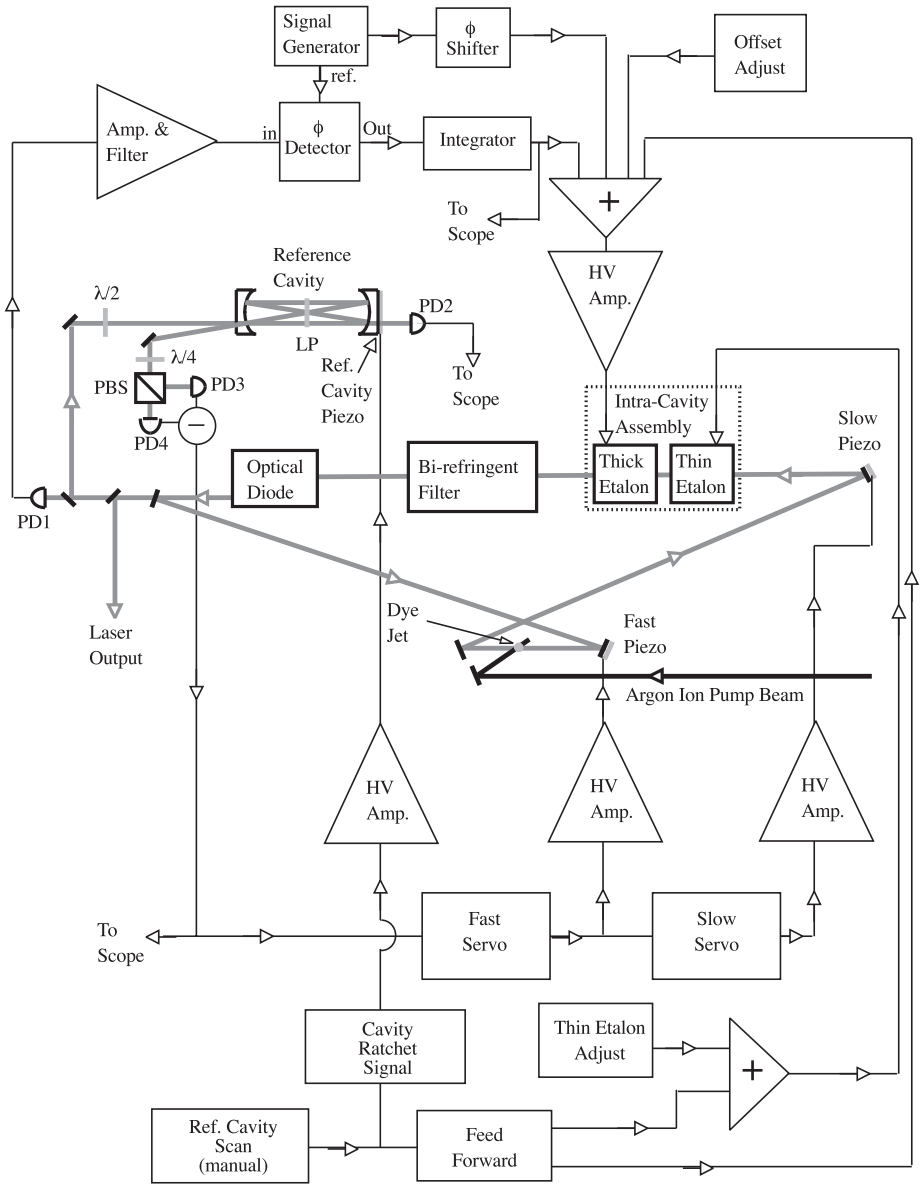

Figure 2.16: Schematic of the home-built dye laser pumped by an argon-ion laser based on a folded 4 mirror cavity. The thick etalon is locked to output power. The frequency is locked by a slow piezo, a fast piezo, and a thin etalon to an Invar reference cavity .

etalon to maximize power.

Optically, the frequency lock is quite different from that in the 899-21. Here we use the Hansch-Couillaud lock scheme [38]. A confocal reference cavity with a free spectral range of 1 GHz is used in a ring configuration. Photodiodes PD3 and PD4 together with polarizing elements measure the polarization ellipticity of light that is reflected from the cavity. The input laser beam is polarized at 45° with the axis of the cavity. The orthogonal component of the beam reflects off the front mirror of the cavity and serves as a phase reference. The other component of the beam resonates with the cavity and experiences a phase shift as the laser frequency scans across a mode of the reference cavity. The difference of photocurrent of PD3 and PD4 shows up as a dispersive lineshape. The laser frequency is locked [2] as shown in Fig. 2.16. This laser was not frequency locked to a saturated absorption feature, though such an option was explored. The Na lock point of the 899-21 is between lines #217 and #218 in the iodine atlas [35]. There are a number of nearby choices of absorption lines to lock to, each of which is composed of numerous sub-Doppler features spread over about 1 GHz. This was not necessary, however, due to the extreme stability of the home-built dye laser. Once brought to the desired frequency, it drifted less than 100 MHz per hour, which is small compared to the typical 5 GHz detuning.

2.3.2 Wavemeter

Laser frequency is measured with a Michelson interferometer with air-bearing translation as shown in Fig 2.17. Laser light is brought to a separate table via an Oz Optics single mode fiber. Originally, a NIST LM-10 wavemeter was used, with accuracy of a part in 10^6, corresponding to 474 MHz per unit in the last stable digit on the fringe ratio counter. Subsequently a NIST LM-11 wavemeter was used with an improved accuracy of a part in 10^7, corresponding to

47.4 MHz per unit of the last stable digit on the ratio counter (the substantial improvement is due to improved fringe counting electronics). The wavemeter is a scanning interferometer formed by corner cube reflectors that are translated via an air-bearing cart-track arrangement, in which the light of unknown frequency traverses essentially the same path as that of a laser of known frequency. As the corner cubes move, the interference pattern is scanned through successive fringes. The ratio of the interference fringes counted simultaneously for each laser yields the ratio of the laser wavelengths in air. The ratio of the wavelengths in vacuum can be extracted if the small correction for the dispersion of air between the reference wavelength and that of the unknown laser is taken into account.

The reference laser is a temperature stabilized HeNe laser [39, 40]. The tube is a Uniphase model 1003-1184. A proprietary mixture of gases is used to give a gain curve narrow enough that only two cavity modes will lase at one time. Adjacent cavity modes are linearly polarized orthogonally, and the Uniphase tube is built with an intentional asymmetry that fixes the direction of this polarization. Upon initial setup the tube is then rotated until BS1 completely reflects the light from the mode that is perpendicular to Fig 2.17. This can be done by measuring the output on a fast photodiode into a spectrum analyzer. A beat note occurs at 750 MHz between the two adjacent lasing modes. When the tube is rotated properly, the beat note disappears, and only one of the modes is transmitted. BS2 reflects some of the light from the mode that is polarized parallel to the figure. The difference of the photocurrent from the two photodiodes is fed back to a temperature controller which adjusts the length of the cavity such that the signals are balanced. This two-mode polarization stabilization scheme can lock to either the red or blue side of the Doppler broadened gain curve by a servo switch, and the lock points differ by 280 MHz. The individual side locks are not of the highest accuracy, but their

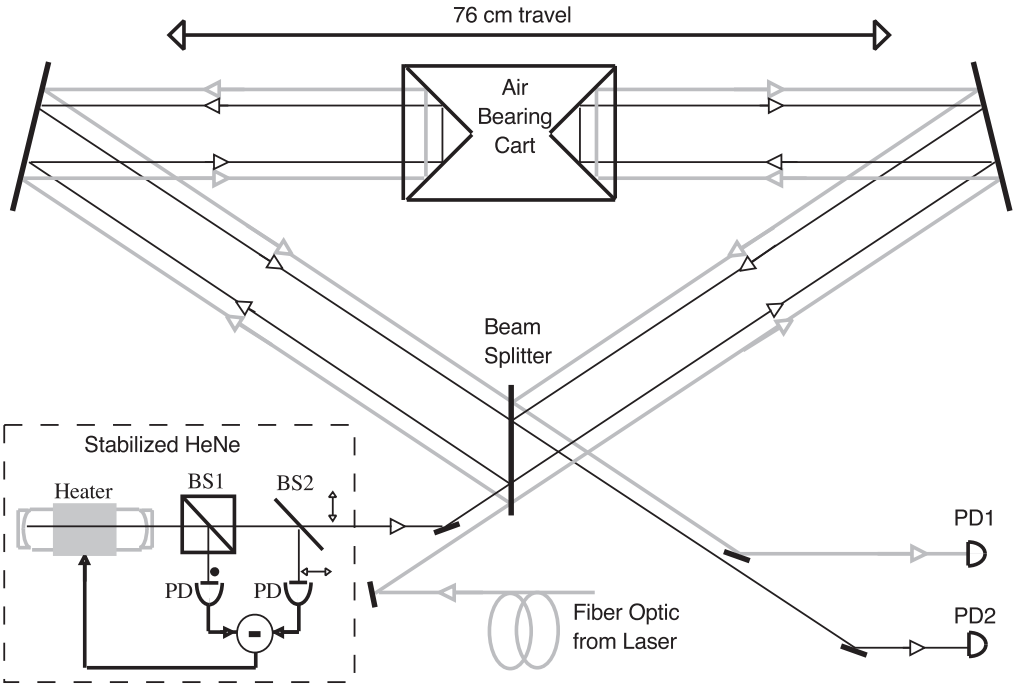

Figure 2.17: Frequency of the dye lasers is determined to 1 part in 10^7 by comparing interference fringes to those of a temperature stabilized HeNe laser. The light is coupled in by a single mode fiber optic. The cart travels along a granite bar on a cushion of N_2.

average is.

$$\nu_{HeNe} = 473\ 612\ 192\ \text{MHz}\ (\pm 30\text{MHz}) \tag{2.4}$$

Since the wavelength of the sodium D2 line in air is

$$\lambda^{air}_{NaD_2} = 588.9950\ \text{nm}, \tag{2.5}$$

the wavelength ratio in air is

$$\frac{\lambda^{air}_{HeNe}}{\lambda^{air}_{NaD_2}} = 1.074400 \tag{2.6}$$

In practice, rather than averaging the two we compared the reading of the 899-21 which is locked 20 MHz to the red of the $(3S_{1/2}, F = 2)$ to $(3P_{3/2}, F = 3)$ transition in sodium to that of the home-built laser all in a single servo position. The detuning from resonance, and not the absolute frequency is what is essential.

2.3.3 Time Dependent Optical Potential: Phase Modulation

Figure 2.18 shows the optical scheme used for the standing wave in the phase modulated experiments of Chapter 3. The associated control electronics are shown in Fig 2.5. Light from the home-built dye laser is power locked to within 1% by feeding back a signal from PD1 to AOM3 using the circuits shown in Fig 2.9 and Fig 2.5. BS1 is a 50/50 beam splitter. The beams are then recombined in a counter propagating fashion to form a standing wave at the MOT. AOM4 and AOM5 are used to turn the interaction beam on and off (with a 150 ns rise/fall time). Rather than using a retro-reflecting configuration as discussed below, this set-up was used so that AOM4 and AOM5 could impart a prolonged constant velocity on the standing wave. This feature was not used in the experiments described here, however, experiments were performed with this non-zero net velocity. Of paramount importance is adjusting the time delay between AOM4 and AOM5. Because of transit time issues with the acoustic

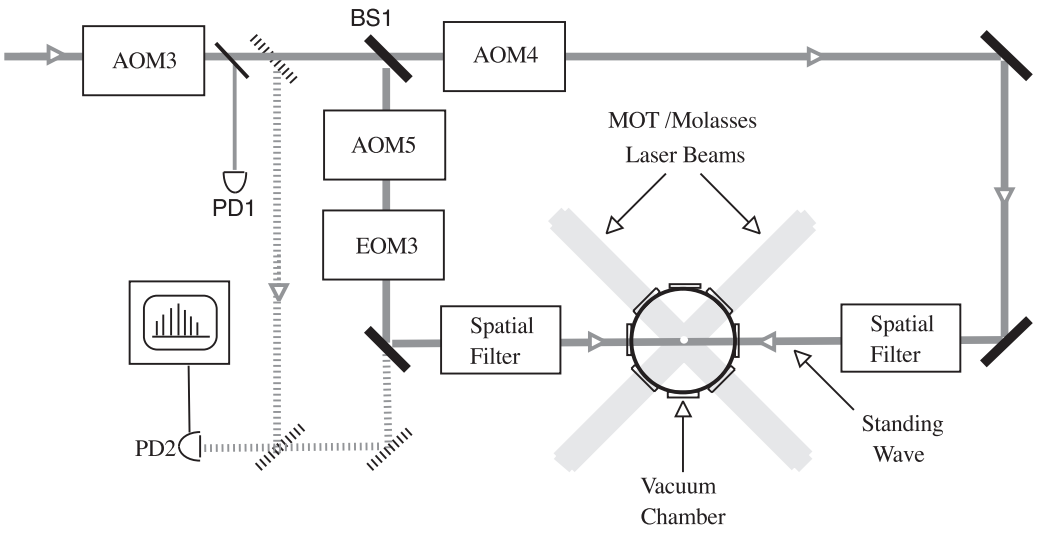

Figure 2.18: Experimental setup for the phase modulated experiments of Chapter 3. AOM3 provides a power lock with feedback from PD1. AOM4 and AOM5 provide of/off switching for the standing wave. EOM3 provides phase modulation of the standing wave, which is calibrated by an optical heterodyne measurement (dotted lines).

waves, an inadvertent relative delay of order 1μs can occur, which would reduce the duration of the standing wave.

EOM3 was used to provide phase modulation. A computer-generated analog signal controls the amplitude of a Stanford Research Systems DS345 synthesized function generator which is amplified by an Amplifier Research 15A250 amplifier that drives an rf helical resonator at a frequency of $\omega_m/2\pi$ = 1.3 MHz, and is described below. A resistive voltage divider enabled the real-time measurement of the rf level driving EOM3, as shown in Fig. 2.5. A small signal from the voltage divider is amplified by a Mini-Circuits ZFL-500LN amplifier to increase dynamic range for *in situ* calibration. The rf power is measured from the amplifier on Marconi 6960 power meter with a 6910 power head. The Marconi outputs a dc voltage proportional to the RF power which is recorded on the pc. The EOM is a Con-Optics Model 370 phase modulator.

At 589 nm the voltage required for a π phase shift is $V_\pi = 217$ V. Note that care is needed in aligning the axis of the EOM (to ensure a correct alignment, vary the input voltage while observing the power output of the EOM between crossed polarizers: no variation should be observed.) The modulation index is calibrated by an optical heterodyne measurement, shown as dotted lines in Fig 2.18. During the calibration, AOM5 imparts a 40 MHz frequency offset in the beam that passes through EOM3. The signal from photodiode PD2 is measured on a spectrum analyzer. A beat note at 40 MHz is seen, as well as frequency sidebands at plus and minus integer multiples of 1.3 MHz about 40 MHz. By varying the rf amplitude going to EOM3, the frequency sidebands go to zero as the corresponding Bessel function coefficient goes through a zero [41]. Between a modulation index of 0 and 14 (corresponding to the maximum allowed voltage of 1000 V suggested by the manufacturer), there are 23 zeros of Bessel functions available for calibration. Only a few are necessary in practice since the modulation index is very linear in the input voltage. By correlating the zeros with the corresponding modulation index, a calibration between applied voltage and modulation index is acquired. The light profile is spatially filtered, as described below, to provide a uniform intensity across the atoms.

The resonator is an air-core impedance matching transformer [42]. The coil is hand wound on thin Plexiglas strips, with a radius of 2.5 cm and a length of 20 cm with approximately 140 turns. This coil is in an enclosed copper cylinder of radius 5 cm and length 26 cm, and lossy dielectric material is kept to a minimum inside. The can was bright-dipped and coated with 'Q-Dope' (commercial form of polystyrene) to reduce lossy oxides. By directly tapping into the coil (at the third loop, approximately), the input has 50Ω impedance, with return reflected power down by 20 dB from the input. The output is high impedance with a voltage step up of 77, and a Q of 108. To provide 2000 Vpp at the EOM, 1.6 W rf power was required. Improved Q

(and hence voltage step-up) and reduced size could be achieved by the use of pre-wound high quality Miniductors from Barker and Williamson, for example.

2.3.4 Time Dependent Optical Potential: Amplitude Modulation

Figure 2.19 shows the optical scheme used for the standing wave in the amplitude modulated experiments of Chapters 4 and 5. The associated control electronics are shown in Fig 2.6. In the retro-reflected configuration shown here, the available power is effectively double that of the configuration in Fig 2.18, since the atoms are optically thin. The disadvantage is that the standing wave cannot be given a prolonged constant velocity. AOM6 is a fast IntraAction model AOM-80 with a 10% to 90% risetime of 25 ns with 80% power into the first-order spot. This was used to provide the amplitude modulation. For the fast pulse modulation experiments of Chapter 4, the pulse shape remains constant, but the number of pulses varies from shot to shot. A Fluke-Philips PM 5712/5715 pulse generator provided 4 ns rise/fall time pulses, in order to take advantage of AOM6's fast response time. The pulse generator was triggered by a Stanford Research Systems programmable DS345 arbitrary waveform generator which was run in burst mode. For each experiment, the PC downloaded the number of pulses that the arbitrary waveform was to trigger (see Fig. 2.6). The number of pulses would vary from shot to shot. For the varying pulse durations of Chapter 5, a single $\sin^2(\pi t/T_s)$ pulse was desired. The first order diffraction efficiency of an acousto-optic modulator is proportional to

$$\sin^2(\frac{\pi}{2}\frac{V}{V_{sat}}) \tag{2.7}$$

where V is the applied voltage, and V_{sat} the saturation voltage. Therefore a linear ramp up and down in voltage to the acousto-optic modulator produces the desired lineshape. The light amplitude was recorded on a Thorlabs PDA150 with amplifier (PD1), digitized on a Tektronix 524A Oscilloscope, transferred

to the computer via GPIB, and stored for later analysis. Small non-linearities in the amplified photodiode need to be taken into account when analyzing the stored traces. Since timing at the limit of the AOM is desired, it is important to realize that acoustic transit time across the laser beam reduces the standing wave duration that individual atoms experience. A 10% reduction from the whole beam measurement for 100 ns fwhm pulses is found. This was measured by expanding the laser spot size and measuring the temporal profile in small pinholes. AOM7 was used for amplitude noise experiments of Chapter 6, where the $\sin^2$ instrument function needs to be taken into account as well. The amplitude of this AOM is also recorded on PD1.

EOM4 (Con-Optics model 370LA, with an extra large area) was used for preliminary phase noise experiments described in Chapter 6, driven by an Apex Microtechnology PA85 amplifier capable of 1000 V/μs slew rate over a 400 volt range. The modulation index was calibrated with an optical homodyne measurement as shown in dotted lines on Fig 2.19. For this device, Con-Optics quotes a $V_\pi = 288$ V at 589 nm, which is consistent with our measurement. Since EOM4 is double-passed and since the periodic potential has period $\lambda_L/2$, then $V_\pi^{eff} = 288/4$ V $= 72$ V. The axis of the EOM must be carefully aligned by varying the input voltage while observing the power output with the EOM between crossed polarizers: no variation should be observed. No data from phase noise experiments will be shown here, because some as of yet uncharacterized difficulties occurred with the model 370LA in this configuration.

Since phase stability is of paramount importance, optical homodyne measurements were also performed in the absence of EOM4. Residual phase noise, well above the residual laser intensity noise, was found to monotonically fall off rapidly with increased frequency. From this it was determined that for reliable phase stability (within a few percent) for the standing wave experiments that the duration must be shorter than 100μs. By hydraulically floating the

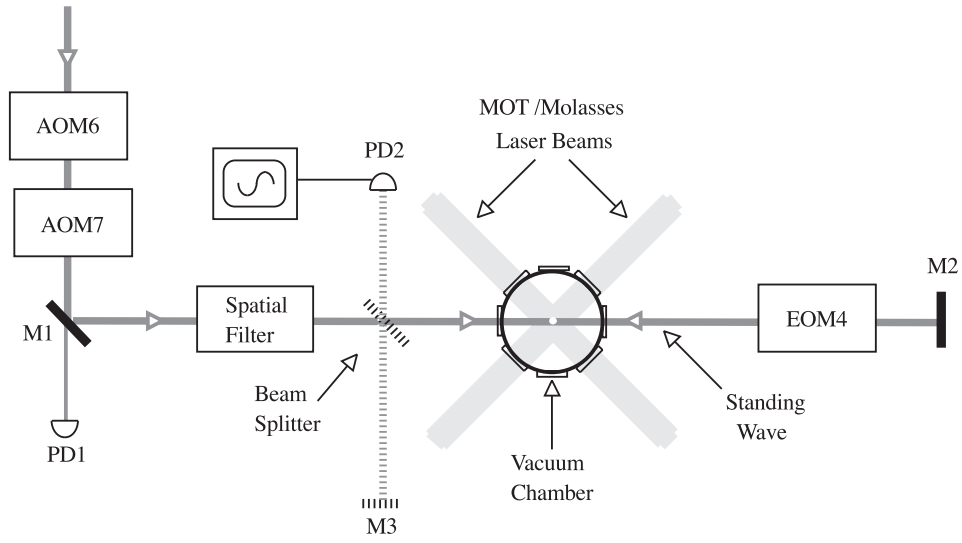

Figure 2.19: Experimental setup for the amplitude modulated experiments of Chapters 4, 5, and 6. AOM6 provides fast on/off. AOM7 and EOM4 provide amplitude and phase modulation, respectively. Standing wave amplitude is recorded via PD1 on a digitizing oscilloscope. Overall phase stability is measured by optical homodyne (dotted lines).

optical table and turning off fans modest improvements could be achieved, though this was not deemed necessary during experiments. In addition to cw measurements, pulsed optical-homodyne measurements with varied optical arm lengths determined that no spurious transient effects due to AOM6 occur. The light profile is spatially filtered to provide uniform intensity at the atoms, as described below.

2.3.5 Spatial Filter and Power Calibration

For a proper comparison of data to theory, it is necessary to know the laser intensity profile across the atoms. For this reason, the beams were spatially filtered by focusing through a 50 micron pinhole. The focus was such that 85% of the incident power is transmitted through the pinhole. Since the power is of order 1 Watt, standard stainless pinholes are easily destroyed. For this

reason, diamond aperture wire dies from Indiana Wire Die were used with good results. After the pinhole, a variable iris blocks all but the center lobe. To determine the field at the atoms, the total beam power was measured on a Coherent Fieldmaster power meter which was calibrated with respect to a NIST traceable Newport model 1825-C powermeter and model 818-UV head, which has an accuracy of $\pm 5\%$. The width of the beam was measured by moving a knife-edge across the profile in front of a detector. The distance between the 70% and 30% power points is measured. If the focus at the spatial filter is small compared to the aperture, then the output is Gaussian. A normalized Gaussian intensity distribution, characterized by a spot size w_o ($1/e^2$ intensity radius) is:

$$I(x,y) = \frac{2}{\pi \mathrm{w}_o^2} e^{-\frac{2(x^2+y^2)}{\mathrm{w}_o^2}}. \tag{2.8}$$

Integrating from the $x_{70\%} - x_{30\%} = d$ power points with an knife edge

$$0.70 - 0.30 = \int_{-d/2}^{d/2} dx \int_{-\infty}^{\infty} dy I(x,y) \tag{2.9}$$

results in

$$\frac{2}{5} = \mathrm{erf}(\frac{d}{\sqrt{2}\mathrm{w}_o}), \tag{2.10}$$

where erf is the error function. By solving numerically, the measured value d is related to the spot size w_o by $\mathrm{w}_o = 1.91\ d$. A Gaussian profile was assumed for the experiments reported here. If, on the other hand, the focus is large compared to the aperture, the output profile is instead:

$$I(x,y) = I_o \left[\frac{J_1(\frac{\sqrt{x^2+y^2}}{c})}{\frac{\sqrt{x^2+y^2}}{c}} \right]^2 \tag{2.11}$$

where J_1 is the first order Bessel function. Evaluating numerically, the measured value d gives $c = 0.758\ d$. Fig. 2.20 shows an ideal Gaussian and Bessel pattern with the same measured parameters, compared to the spatial distribution of the atoms. The actual profile is probably somewhere in between the

two extremes. There is, unfortunately about a 6% discrepancy at the center, where the majority of the atoms are. A better way in the future may be to measure the peak spatial power through a small, well characterized pinhole in the beam center, to use a commercial beam profiler, or to use a beam flattener.

The field strength E_o, must be determined to connect to Eq. 1.4. For now the profile is assumed to be Gaussian. The beam is experimentally characterized by the total power ($\langle P \rangle$) and the $x_{70\%} - x_{30\%} = d$ power points. From this, $\mathrm{w}_o = 1.91\ d$ is determined as described above. A 'flat,' linearly polarized traveling Gaussian beam has the form

$$\vec{E}_{Gauss} = \hat{y} E_0 e^{-(\frac{\sqrt{x^2+y^2}}{\mathrm{w}_0})} \cos(\omega_L t + k_L x). \tag{2.12}$$

The time-averaged intensity has the form

$$\langle I \rangle = \frac{1}{2} c \epsilon_o E_o^2. \tag{2.13}$$

The integrated power can then be calculated

$$\langle P \rangle = \int \langle I \rangle dA \ = \pi \mathrm{w}_o c \epsilon_o E_o^2 \int_0^\infty dr e^{-2\frac{r}{\mathrm{w}_0^2}} \ = \frac{\pi c \epsilon_o \mathrm{w}_o^2 E_o^2}{4}\ , \tag{2.14}$$

where $r = \sqrt{x^2 + y^2}$, which gives us

$$E_o = \sqrt{\frac{4\langle P \rangle}{c \epsilon_o \pi \mathrm{w}_o^2}}. \tag{2.15}$$

This gives the expression for field strength used in Eq. 1.4 in terms of experimentally measured quantities. It is important to note that $\langle P \rangle$ is the time-average power in one of the two beams. In fact $\langle P \rangle$ should be the power in the lesser of the two beams (being sure to compensate for window losses) assuming the spot sizes are the same. Any excess field strength in one beam over the other does not contribute to the standing wave field.

Even if the exact laser profile is known, other uncertainties in the standing wave field strength at the atoms include interference fringes caused by the

windows, wavevector mismatch and misalignment between the two counter-propagating beams. Ideally one should have an *in situ* measurement of the power on the atoms by analyzing the effect on the atoms, such as the Mollow triplet. Uncertainty in the intensity is the largest experimental uncertainty.

In any case, there is a variation in intensity across the atoms, as shown in Fig. 2.20 due to the limited amount of total laser power available. When comparing to theory, one can characterize the sample by a spatial rms value, or one can accurately account for the spatial variation in a simulation. Both approaches have been used here. To make contact with the Hamiltonian described in Sec. 1.1, the effective Rabi frequency, Ω_{eff}, needs to be determined. For this, the dipole moment is needed. The dipole moment can be calculated from the Einstein A coefficient [43].

$$d = \sqrt{\alpha_c}\sqrt{\frac{3\epsilon_o \hbar \lambda^3}{8\pi^2 \tau}} = 1.71\text{x}10^{-29}\ \text{Cm} \tag{2.16}$$

where $\tau = 1/\text{A} = 16.6$ ns is the excited state lifetime, and $\alpha_c = 2/3$ to account for the ratio of the Clebsch-Gordon coefficients between linearly and circularly polarized transitions.

2.3.6 Spatial Overlap

Spatial overlap of the interaction laser with the atoms is extremely important. Figure 2.20 shows a realistic spatial atomic distribution characterized by an rms of $\sigma = 0.15$ mm, compared to a typical laser field and intensity distribution, characterized by a $\text{w}_0 = 1.2$ mm ($1/e$ radius of field, or equivalently the $1/e^2$ radius of the intensity). For good spatial overlap, the interaction laser beam was first tuned closer to resonance. The first pass is adjusted for maximum deflection of the atoms while the MOT is on. Then the return pass is then overlapped spatially with the first pass. Another method used computer control. The MOT was turned off and the first pass of the interaction beam

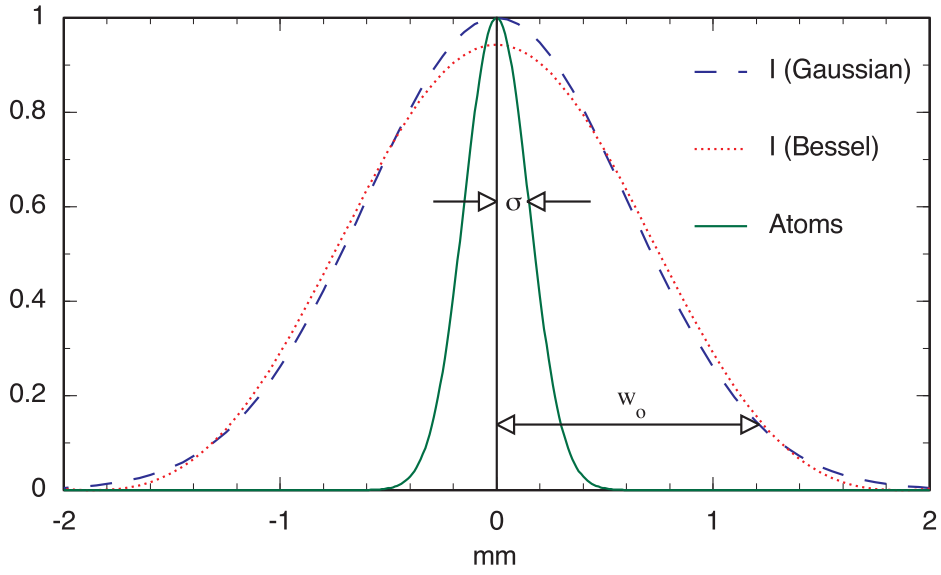

Figure 2.20: An idealized Gaussian laser intensity (w_o = 1.2 mm) compared to an idealized Gaussian atom distribution (σ = rms = 0.15mm) with realistic parameters. A Bessel intensity distribution ($c = 0.48$) is also shown that has the same total power and 30%/70% knife edge integrated power points as the Gaussian.

was pulsed on for a controlled duration. After a free drift time, the molasses was turned on and a CCD image was taken. The first pass was adjusted for maximum deflection. The return path was then overlapped with the first pass.

2.4 Detection of Momentum Transfer

2.4.1 Molasses

Optical molasses forms a viscous environment for the sodium atoms that is used to freeze-in the position of the atoms and provide spontaneous emission for detection. The same viscous forces are responsible for the cold initial conditions that are present in the MOT (see Sec. 2.2.1). Consider first the Doppler cooling mechanism [44]. Suppose an atom is at rest in a pair of counter-propagating laser beams which are detuned to the red of the atomic resonance. The radiation pressures exerted by the two beams exactly balances, and the total force averaged over a wavelength vanishes. If, on the other hand, the atom is moving along the standing wave, the counterpropagating waves undergo opposite Doppler shifts. The beam opposing the atom's motion gets closer to resonance and this wave exerts a stronger radiation pressure than its counterpart. This imbalance gives rise to an averaged net frictional force that always opposes motion and provides viscous confinement. A 3-dimensional optical molasses is formed when three orthogonal counterpropagating pairs are used.

The Doppler force is not the only mechanism at work. Each pair of beams in the laser configuration shown in Fig. 2.10 provides a local polarization that is linear everywhere with a direction of polarization that rotates a full turn every wavelength (a helix of pitch λ). The corkscrew polarization gives rise to a mechanism called polarization rotation cooling [45] (which is quite distinct from the Sisyphus effect [46]). An atom at rest is optically pumped into a distribution of ground m states having alignment (different populations for states with different $|m|$) along the polarization axis but no net orientation

(asymmetry between positive and negative m levels). When the atom moves (non-adiabatically) parallel to the laser propagation axis, an orientation develops along the axis. The population asymmetry is such that the most populated state is the one that absorbs light most strongly from the circularly polarized wave opposing its motion. This asymmetry in the absorption accounts for the damping force in polarization-rotation cooling and allows for much colder temperatures than the Doppler mechanism alone. For the purposes of this work, however, the details are not important. Optical molasses simply provides a cold initial condition and a strong viscous environment with which the atomic motion is frozen-in during detection of fluorescence.

2.4.2 Optimizing the MOT/Molasses

In addition to viewing by eye and the CCD camera (see Section 2.4.4) an inexpensive Panasonic WV-BL204 camera with an Ikegami PM-930A monitor was used for diagnostics. The view of this camera was 90° from that of the CCD, so together information for all 3 axis was available.

A great deal of time in setting up experiments with this set-up was spent optimizing the MOT and molasses. First it is necessary to balance the optical power in the 6 beams with the appropriate choice of ND filters. It is essential that each counter propagating pair be matched to within a few percent. Some mismatch (up to 10 %) between orthogonal pairs is acceptable. The variable aperture shown in Fig 2.3 is extremely useful in alignment. It is closed to its smallest opening in order to overlap counter-propagating beams and to insure that all 6 beams intersect at a point. Each beam must be made colinear with its counter beam. This was done by overlapping spots on a piece of paper outside the cell while taking advantage of as much lever-arm as possible. The three pairs of beams must overlap at one point. This was done by gently heating the cell with a heat gun to increase the amount of sodium vapor while the

vacuum pump is valved off. By locking the laser to the sodium transition, scatter from the beams is used as a diagnostic in alignment. When all six beams are properly aligned, the glass cell is moved until the overlap of the six beams is at the center of the gradient coils. This was necessary since the coils are rigidly affixed to the cell. Then the variable aperture is alternately opened and closed. A MOT is formed when the aperture is open. The gradient coils are translated until the MOT is centered on the intersection of the six beams. One improvement would be to set-up the gradient coils to move independently of the vacuum cell for ease of adjustment. The above procedure was typically only necessary every few months.

On a daily basis, fine adjustments were necessary. The beams are kept on (except for the extremely small gradient field ramp-down time), and the gradient coils are chopped on and off. With the gradient on, a MOT is formed. With the coils off, the atoms spread diffusively in the viscous optical molasses. The field nulling Helmholtz coils are fine adjusted by repetitively taking two-dimensional CCD images of the atoms as they expand diffusively. The expanding cloud of atoms is centered on the initial MOT and is spherical when the fields are properly adjusted. It is essential that this expansion be symmetric and well centered for short and long diffusion times. Since the windows of the cell are not anti-reflection coated, there are intensity fringes which also cause asymmetric expansion. For this reason it is necessary to fine adjust the optical beams as well as the magnetic nulling fields. Intensity fringes also occur due to diffraction from dust on the optics, from the edges of the variable aperture, and from overfilling optics. When the MOT is spherical and compact, and the diffusive expansion is uniform and well centered, then the beam intensity, RF sideband intensity, and frequency detuning are adjusted to minimize the MOT temperature. This is done by the time of flight measurement shown in Fig. 2.1. Typically the best operation occurred with 6 mW/cm^2 per beam at the atoms, detuned by 20 MHz, with 15% intensity sidebands. The above op-

timization procedures often need to be done iteratively, and the process does not always rapidly converge to an optimal case largely because spurious fringes in the optical power need to be balanced. Future improvements should include anti-reflection coatings of the cell windows, larger optics so that beams do not overfill them resulting in diffraction. Magnetic field uniformity could also be improved with a μ-metal shield.

2.4.3 Time of Flight

The detection of momentum that is transferred to the atoms is done by a time-of-flight followed by freeze-in technique first developed in our laboratory (to our knowledge). Other time-of-flight techniques have been used [47, 48]. With our technique, first a CCD image of the MOT is taken. The molasses beams are then turned off, allowing the atoms to drift freely. After a well defined free-drift period, these beams are turned back on (without the gradient magnetic field). This creates a strong viscous environment for the atoms, and their motion is rapidly damped in 10's of microseconds. The atoms do continue to diffuse, but at a very slow rate. During this time the atoms fluoresce, and another CCD image is taken. For a time-of-flight measurement to make sense, the interaction time with the far-detuned laser must be much smaller than the free drift time, so that essentially all of the macroscopic atomic motion is free ballistic motion during the drift. In addition, there must not be significant motion during the freeze-in; see Fig. 2.21. The CCD image is a two-dimensional projection of the atomic distribution, as shown in Fig. 2.22. Each image is subtracted from a background image where the laser is either detuned from resonance or the gradient coils are turned off. This leaves the laser light background but not the atomic signal. The CCD image is integrated transverse to the interaction beam, since expansion in this direction is only a result of thermal initial conditions. This gives a spatial distribution. Typical spatial distributions are shown in

Fig. 2.23. The drift time must be long enough that the final distribution is significantly larger than the initial distribution, but not so long that the atoms extend spatially beyond the region where the molasses is well characterized. One indication that the distribution is extended too far is the reduction of area under the curve. Another method to determine the useful molasses area is to launch atoms and probe the distribution area as a function of excursion from center. Generally the distribution should not exceed a spread of about 1 cm. One important advantage of a computer controlled drift time is that the drift time can be varied as the anticipated final spread varies. When the time of flight is taken into account, the final momentum distribution can be inferred. Ideally the initial spatial distribution should be deconvolved. In practice this is difficult, and in fact is not necessary when the structure of interest in the final distribution is large compared to the initial distribution. No momentum distributions presented in this work are deconvolved. When rms values are calculated, however, the initial spatial spread was subtracted in quadrature.

$$\sigma_{decon} = \sqrt{\sigma_f^2 - \sigma_i^2} \tag{2.17}$$

For the case of Gaussians, this is the correct deconvolution. When the final distribution is large compared to the initial distribution this subtraction makes no perceptible difference. For all cases presented in this work, when the initial distribution is small enough for this subtraction to make a noticeable change, the distribution was roughly Gaussian and hence the rms momentum is correctly deconvolved. The initial momentum distribution is not deconvolved in either case. Instead, the theoretical simulations take into account the initial momentum, though the simplistic model curves do not.

2.4.4 CCD Camera and Data Analysis

The CCD camera is a Peltier cooled (-40 C) Princeton Instruments TE/CCD-576EMUV camera with 576 x 384 pixels, 22 x 22 μm each. This camera is run

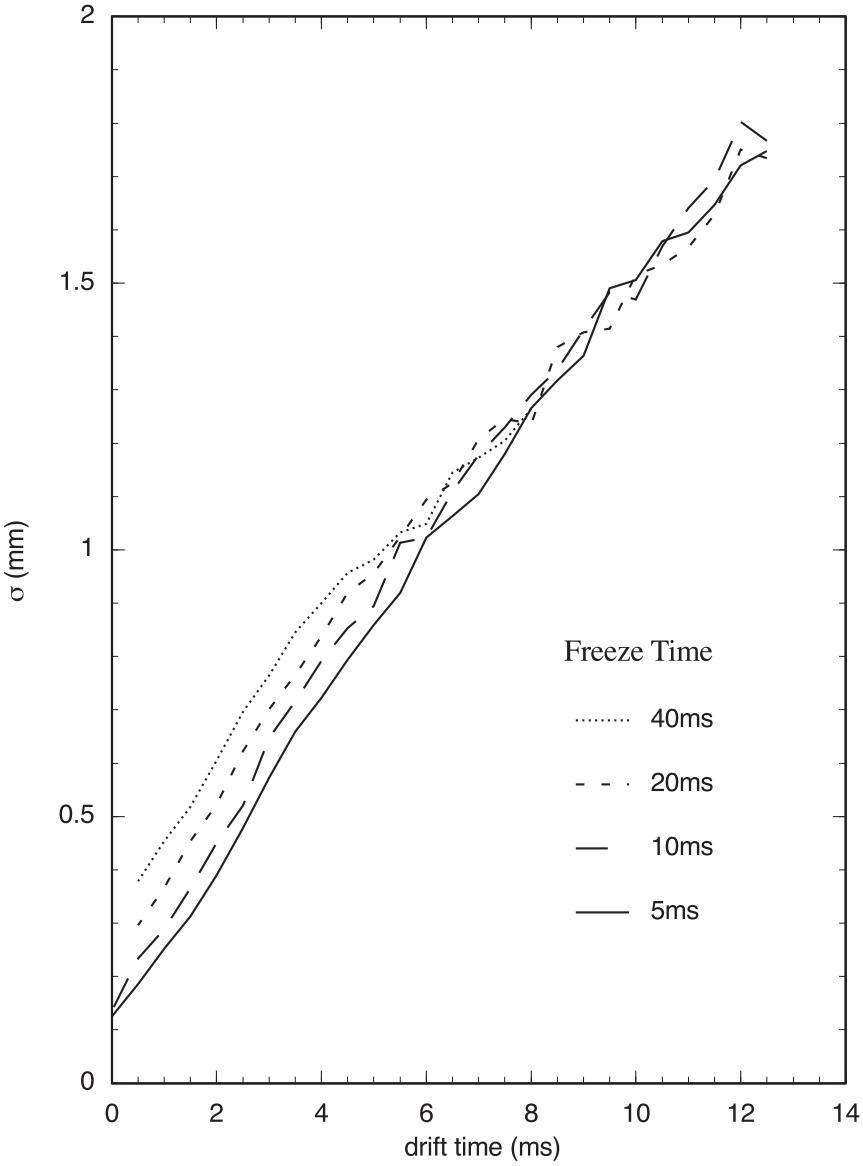

Figure 2.21: RMS momentum as a function of free drift time. For freeze-in times of 5 to 10 ms, the slope of the strait line gives the momentum and demonstrates the validity of the freeze-in technique. For longer freeze-in times, there is significant atomic motion and the line does not extrapolate to the initial condition. For this reason, CCD exposures were limited to 10 ms.

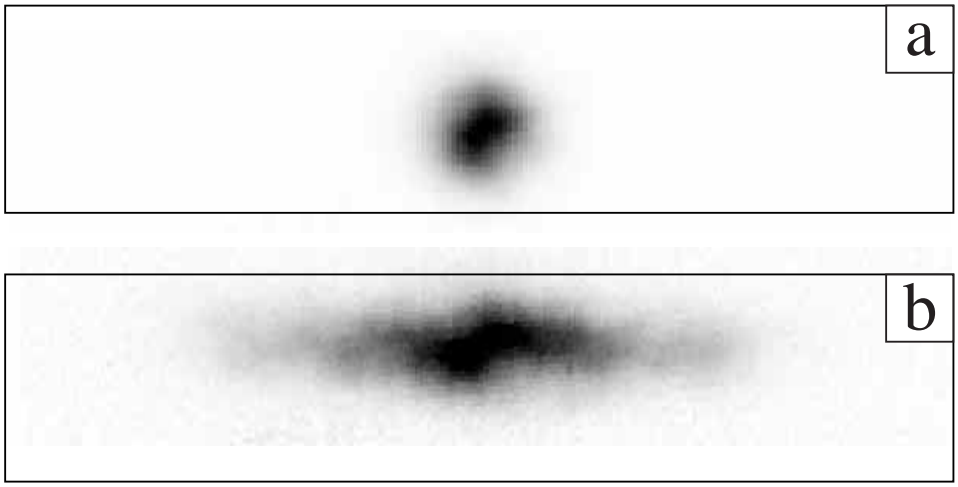

Figure 2.22: A 2 dimensional projection of the atomic fluorescence distribution taken with the CCD camera. (a) shows a distribution after a 2 ms free drift. (b) shows increased spread due to the interaction with a time dependent standing wave after the same drift time.

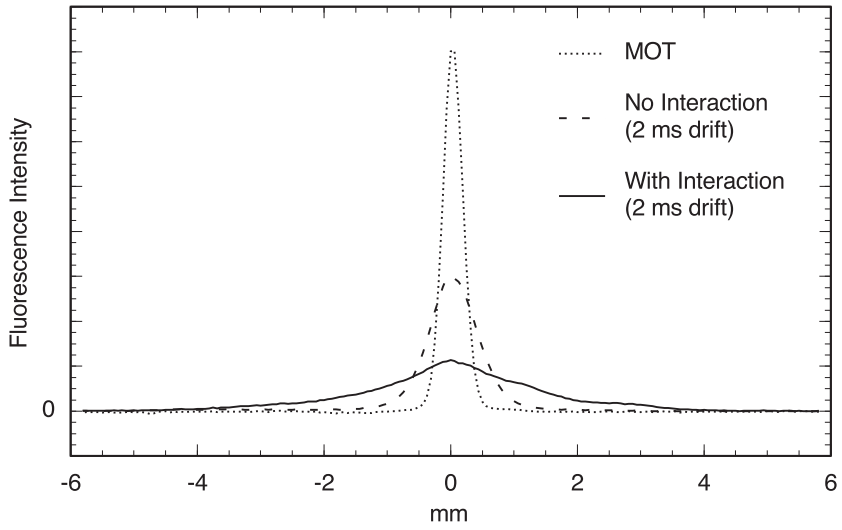

Figure 2.23: An integrated CCD image showing only spatial spread along the axis of the standing wave. The MOT profile is taken before the free drift time. Drift time is ideally set so that the final distribution is large compared to the initial MOT spatial distribution but still within the usable molasses region

by a ST135 camera controller which is operated by Macintosh IIsi computer through a National Instruments GPIB board and Nu-Bus adapter. A TTL trigger from the 486-33 PC initiates an exposure. The CCD chip is about 40 cm from the MOT/molasses, a Sigma 90/2.8 Macro lens with a Nikon bayonet compatible mount forms an image on the CCD. For the phase modulated data, the lens aperture was set at its smallest value f/22 to achieve the best depth of focus. Later it was determined that with a larger aperture, better signal-to-noise could be achieved at the cost of reduced depth of focus. The largest aperture setting of f/2.8 gave the best signal to noise and a depth of focus of about 2 cm was still deemed adequate, since the atomic sample never exceeded this range. Spatial dimensions were calibrated by imaging a machinist's ruler in front of and behind the glass cell and taking the average, or equivalently by pivoting the camera away from the cell and placing a ruler at the distance of the atomic sample. A value of 16 pixels/mm is typical. By imaging a ruler on the far side of the cell, it was determined that the curved glass surface through which the image is taken does not cause significant distortion on the length scales of interest. The lens was focused on the atoms in-situ, by taking repeated images of the MOT. Detector efficiency was determined by directly exposing the CCD chip to a highly attenuated but well characterized laser beam. It was determined that there are about 0.026 counts/photon. Discrepancies of this measurement, taking electronic gain into account, with manufacturer specs were never resolved. Exposure timing is controlled with a Uni-Blitz mechanical shutter between the lens and the CCD chip. Exposure times for these experiments are at the limit of what the shutter can do. The shutter was examined by removing the shutter housing from the camera and testing its timing with a light source and a fast photodiode. If an exposure time of 10 ms is set, there is about a 3 ms delay from the trigger, and the exposure varies from 14 ms at the center to 8 or 10 ms at the sides of the shutter depending on the photodiode location with respect to the geometry of the shutter blades. One improvement

to the experiment would be to open the shutter for a longer duration and to simply strobe the light on for a well defined period of time. A more expensive approach is to use a faster shuttered ICCD camera. The data acquisition software is Rhea Corporation's KestrelSpec by George Ritchie. While this package does not have extensive post acquisition processing capabilities, its real-time acquisition capabilities such as background subtraction were significantly better than other available software. The entire CCD chip was not needed for data collection. A region of interest of 200 x 200 pixels corresponding to field of view at the atoms of 12.5 x 12.5 mm. For this smaller region, the timing variation across the shutter is reduced. Integration to a 1-dimensional distribution can be done on the chip or in software. By binning on the chip, superpixels of 1 x 200 pixels can be used. The advantage of this approach is faster read-out and less read noise. This experiment is laser light scatter limited, however, so neither read noise nor dark noise were a limiting factor. Another approach is to integrate the 2-dimensional image in software. While this approach is slower, it has the advantage of easily switching between 2 and 1 dimensional viewing. One feature which was not exploited is the fact that KestrelSpec is Apple Event scriptable, allowing custom features to be written. It would be ideal, however, if a LabWindows type approach were taken where the end user could write C code to make fully custom acquisition and processing software. After acquisition, data were analyzed with C programs written in the Symantec C environment on the Macintosh. Each one dimensional curve f(i) has approximately N=200 points corresponding to 200 pixels. The norm, mean, and standard deviation were calculated as

$$\text{norm} = \sum_{i=1}^{N} f(i) \tag{2.18}$$

$$\text{mean} = \frac{\sum_{i=1}^{N} i f(i)}{\text{norm}} \tag{2.19}$$

$$\text{variance} = \frac{\sum_{i=1}^{N} i^2 f(i)}{\text{norm}} - \text{mean}^2 \tag{2.20}$$

$$\text{standard deviation} = \sqrt{\text{variance}} \tag{2.21}$$

Due to reasons described previously (molasses laser beams overfilling the windows, frit material on the windows, etc.), a great deal of scattered light needs to be subtracted in the image. So even though the power level is locked, often times it is necessary to numerically shift the baseline to zero when background subtraction is insufficient. The norm and mean of each curve are typically consistent (within a few percent) with that of the initial MOT and of the temperature measurement (MOT after a free drift), otherwise the data is rejected. Calculation of the standard deviation of a distribution assumes an always positive distribution function, therefore points below zero were set to zero. The standard deviation calculation heavily weights the far wings of a distribution, so because of noise in the far wings of distributions, they had to be truncated where the signal becomes lost in the noise. An improved vacuum chamber with enlarged antireflection coated windows for both the laser beams and the CCD camera should drastically reduce background scatter, which is by far the largest source of noise in the data.

Chapter 3

Modulated Standing Wave (Phase Modulation)

3.1 Introduction

We now look at the Hamiltonian of equation 1.15, and consider the case of sinusoidal phase modulation:

$$H = \frac{p^2}{2M} - \frac{\hbar\Omega_{eff}}{8}\cos\left[2k_L(x - \Delta L\sin(\omega_m t))\right] \tag{3.1}$$

where ΔL is the modulation amplitude and ω_m is the modulation frequency. This system is a realization of the periodically driven rotor [49] where the underlying classical phase space goes from stable to chaotic as the modulation amplitude is varied. The experimental results are in good absolute agreement with a quantum Floquet analysis and with a quantum simulation. The underlying classical dynamics in this mixed phase space regime can be related to the quantum evolution. While this general topic has been the focus of much theoretical work, previous experimental progress has been more limited [50], and many key predictions have yet to be verified. This problem was also addressed theoretically by Schleich [51].

To connect with previous theoretical work we convert Eq. 3.1 to scaled dimensionless variables $\tau = \omega_m t$, $\phi = 2k_L x$, $\rho = (2k_L/M\omega_m)p$ and $\mathcal{H} = (4k_L^2/M\omega_m^2)H$, to obtain

$$\mathcal{H} = \frac{\rho^2}{2} - k\cos(\phi - \lambda\sin\tau) \tag{3.2}$$

which is the dimensionless Hamiltonian for a periodically driven rotor. The amplitude is $k = \omega_r \Omega_{eff}/\omega_m^2$, where $\omega_r = \hbar k_L^2/2M$ is the recoil frequency and $\lambda = 2k_L \Delta L$ is the modulation amplitude. Experimentally λ is equivalent to the modulation index of EOM2. In this system of scaled units the commutator becomes $[\phi, \rho] = i\bar{\hbar}$, where $\bar{\hbar} = 8\omega_r/\omega_m$. Obviously the scaling that is chosen has no effect on the physics involved.

Our initial momentum spread is Gaussian distributed with $\sigma = 4.6\hbar k_L$. We have measured the momentum distributions for λ from $0 \rightarrow 7$ in order to cover the full range of mixed phase space dynamics. The measured rms momenta vs. λ are shown in Fig. 3.1 (diamonds). The empty diamonds are for an interaction time of 10 μs and the solid diamonds are for 20 μs showing that these results are close to saturation for the range of λ that is shown. The probability of a spontaneous emission event during a modulation period is below 1.0% in this case.

The width of the atomic momentum distributions show oscillations as a function of the modulation amplitude, both in the classical as well as in the quantum analysis. Certain values of the modulation amplitude show dips classically, associated with almost regular motion, which are in reasonable agreement with the quantum prediction. At values of the modulation amplitude where peaks are predicted classically, however, the quantum mechanical momentum distribution is much narrower. Here the classical motion is chaotic, but quantum mechanically dynamical localization manifests itself showing characteristic exponential lineshapes.

3.2 Classical Analysis

The simplest understanding of this Hamiltonian is in terms of resonant kicks (RK). When the velocity of the atom does not match that of the standing wave, the time average force is very small. When the velocity of the atom equals that

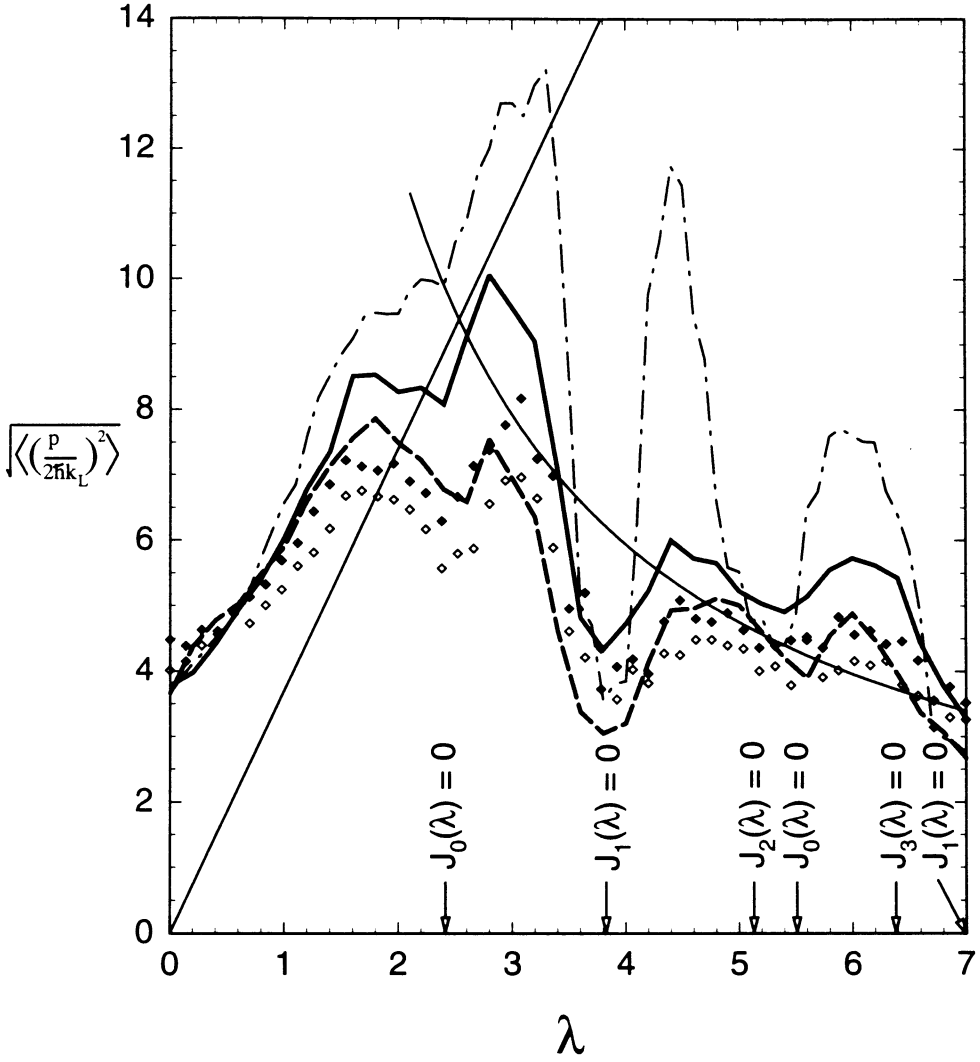

Figure 3.1: The rms momentum width as a function of the modulation amplitude λ. Experimental data is denoted by diamonds. The empty diamonds are for an interaction time of 10 μs and the solid diamonds are for 20 μs; classical simulation for 20 μs (dash-dot line); quantum Schrödinger for 20 μs (heavy dashed line); quantum Floquet for long-time limit (heavy solid line). The light solid lines denote the RK boundary and the curve proportional to λ^{-1} is a simple localization length estimate. $k_{av} = 0.37$, $\bar{k} = 0.16$, $\omega_m/2\pi = 1.3$ MHz. The dominant experimental uncertainty is a 10% systematic in k due to laser power calibration [52].

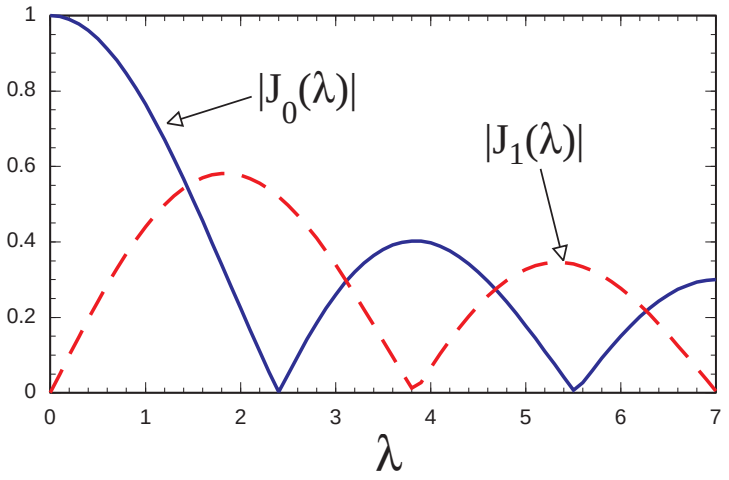

Figure 3.2: The absolute value of $J_0(\lambda)$ and $J_1(\lambda)$.

of the modulated standing wave the atom receives a large kick in momentum. This condition $\rho = \dot{\phi} = \lambda \sin(\tau)$ (called the stationary phase condition) occurs twice during each modulation cycle, however, not at evenly spaced intervals. There is a limit to this process: when the atom velocity exceeds the maximum velocity of the standing wave the stationary phase condition cannot be satisfied and the atom receives no more resonant kicks. The result is a boundary in momentum. For sufficiently many kicks, an ensemble of atoms spreads diffusively over the entire phase space up to $|\rho| \leq \lambda$. This would result in a square distribution in momentum centered at $\rho = 0$ with a width of 2λ. The corresponding rms momentum width in experimental units using the fact that $\rho/\bar{k} = p/2\hbar k_L$ is

$$\sigma_{RK} = \frac{\sqrt{\langle p^2 \rangle}}{2\hbar k_L} = \frac{\lambda}{\sqrt{3}\bar{k}} \tag{3.3}$$

This simple minded curve is plotted in Fig. 3.1, and represents an effective boundary in momentum space. It is not, however, a hard boundary. A naive analogy is the sport of surfing. On average there is very little horizontal momentum transfer to the surfer until she catches a wave (stationary phase condition). The maximum velocity that she can achieve is slightly larger than the

velocity of the fastest wave, by starting at the top of a wave and working her way down as the wave progresses. The momentum distribution can thus exceed the simple limit of Eq. 3.3 for other reasons as well. Near $\lambda = 0$, the initial condition of $\sigma/2\hbar k_L = 2.3$ already exceeds the simple boundary. In addition, the non-adiabatic turn on of the well also imparts momentum which is not accounted for by this simple boundary. The actual momentum distribution may not reach the boundary. As λ is increased, the duration of a resonant kick is reduced (keeping the modulation frequency constant). Thus the number of kicks, and hence cycles, required to reach the boundary increases with λ. Most importantly, that boundary does not take into account the complications of islands of stability which will be discussed below.

This problem has been analyzed in terms of the delta kicked rotor and the standard map [1, 11]. The great utility of the standard map is in the fact that any non-linear system can be locally approximated by it. The major difficulty with this approach is that for this system there are two kicks per cycle that are not equally spaced in time. The amplitude modulated case discussed in Chapter 4 is much more amenable to this analysis, so it will not be done here.

For a more realistic understanding, it is instructive to look at the Fourier expansion of the interaction Hamiltonian

$$\mathcal{H} = \frac{\rho^2}{2} - k\cos\left(\phi - \lambda\sin\tau\right) = \frac{\rho^2}{2} - \sum_{m=-\infty}^{\infty} kJ_m(\lambda)\cos\left(\phi - m\tau\right) \qquad (3.4)$$

where $J_m(\lambda)$ are ordinary Bessel functions of integer order. Each term of this expansion represents a pendulum (equivalent to Eq. 3.2, with $\lambda = 0$) centered at $\rho = \dot{\phi} = m$ (resonance condition). In physical units, each term has a stable point with $p/2\hbar k_L = m/\bar{k}$. This results in a chain of islands of stability, separated by integer multiples of $1/\bar{k}$ in momentum, some of which can be seen in Fig 3.3. The mth term in Eq. 3.4 has a depth in energy of $2k|J_m(\lambda)|$.

By equating this to $\rho^2/2$ we see that each island has an approximate width in momentum W given by

$$\frac{W}{2\hbar k_L} = \frac{4}{k}\sqrt{k|J_m(\lambda)|} \tag{3.5}$$

in units of $2\hbar k_L$. Chaos occurs when two islands of stability overlap in phase space. Resonance overlap will be discussed in more detail for a more simple system in Chapter 5, but provides a simple estimate of the range of λ for which the classical particle diffuses in momentum. Initial conditions inside an island of stability remain there classically. Islands serve to reduce momentum diffusion for initial conditions that are not inside them.

For a more quantitative understanding we numerically integrate Hamilton's equations

$$\frac{\partial \mathcal{H}}{\partial \phi} = -\dot{\rho} = k \sin\left[\phi - \lambda \sin \tau\right] \tag{3.6}$$

$$\frac{\partial \mathcal{H}}{\partial \rho} = \dot{\phi} = \rho \tag{3.7}$$

Numerical integrations shown here use two different sets of initial conditions. The first is a grid in (ϕ, ρ) space from which phase portraits (also known as stroboscopic maps or Poincaré sections) are constructed. The system is evolved for each point on the grid and the location in in (ϕ, ρ) is recorded once each cycle. A Poincaré section contains the space of all solutions, and is extremely useful to gain insight into the physics. The second mimics the experimental conditions where the ρ are Gaussian distributed while the ϕ are uniformly distributed in the interval $[0, 2\pi]$ and are used for the lineshapes and rms calculations. The uniform distribution in ϕ is justified because the 0.12 mm rms atom cloud size is much greater than one period of the standing wave.

The variation of the classical rms momentum width as a function of λ is shown in Fig. 3.1 (dash-dot line). Momentum transfer in this problem occurs primarily when the velocities of the atom and the standing wave are matched. At small λ, the distribution quickly saturates near the RK boundary. As λ is

increased oscillations occur with the dips corresponding to zeros of the Bessel functions. The overall amplitude of the oscillations decreases as λ is increased due to the reduction of the size of each RK. The classical simulation for different times shows that the peaks grow until the RK boundary, while the dips grow at a much slower rate. This difference in rates is explained by the phase portraits shown in Fig. 3.3. The peaks are predominantly chaotic while the dips are nearly integrable, corresponding to the majority of the initial condition inside an island of stability. Classically, once inside an island, the particle can never escape. The classical lineshapes in Fig. 3.3 (middle panel) clearly show these features as well as the effect of the RK boundary. Initial conditions contained within an island remain trapped, while those in the chaotic domain diffuse up to the boundary, leading to "boxlike" distributions. A clear example of the stability at the dips is at $\lambda = 3.8$ where J_1 has its first zero (see Fig. 3.2). The final momentum spread in this case is governed by the surviving island due to J_0 and the system is nearly integrable. Note that the oscillations of the Bessel functions are reflected in the exchange of the location of unstable (hyperbolic) and stable (elliptic) fixed points, which is relevant in the context of scarring which will be discussed in Chapter 6. This is clearly visible on contrasting the phase portraits for $\lambda = 0$ and $\lambda = 3.0$, which is beyond the first zero of J_0 at $\lambda = 2.41$.

3.3 Quantum Analysis

The behavior is quite different in the quantized system. Dynamical localization occurs, which corresponds to quantum-mechanical destructive interference of the transition amplitudes with large changes of momentum [1]. For early times the system diffuses at a rate predicted by classical analysis as if the system were continuous. The system locks into dynamical localization, characterized

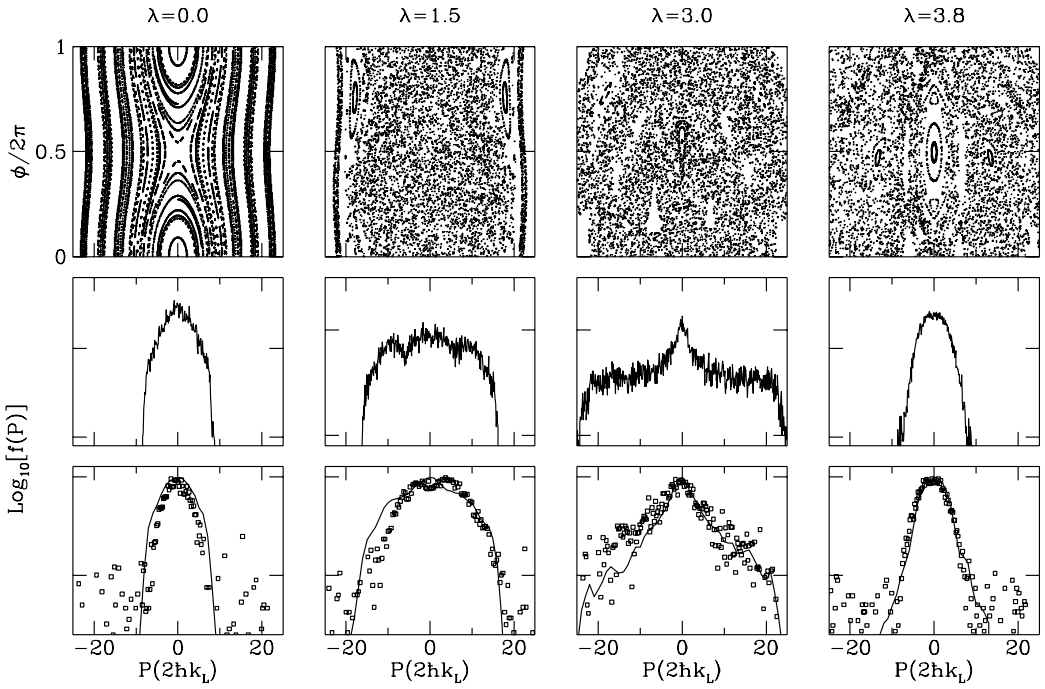

Figure 3.3: Phase portraits (upper panel), classical momentum distributions (middle panel), and experimentally measured momentum distributions with Floquet theory (bottom panel, theory marked by lines) for $\lambda = 0, 1.5, 3.0, 3.8$. The initial conditions are described in text. The vertical scales for the distributions are logarithmic and are marked in decades [52].

by an exponential momentum distribution

$$\Psi^*\Psi = e^{-\frac{|\rho|}{l_{loc}}} \tag{3.8}$$

with a localization length l_{loc}. This occurs at a time determined approximately by the time/energy uncertainty relation: the larger the mean energy level separation the shorter the timescale. The characteristic time scale for this to occur is called the quantum break time. As discussed above, the classical diffusion rate goes as $1/\lambda$, from which it follows that the localization length also goes as $1/\lambda$. For an exponential distribution, the rms is $\sigma_{loc}/2\hbar k_L = \sqrt{2}l_{loc}/\hbar$

$$\sigma_{loc} = \frac{\sqrt{\langle p^2 \rangle}}{2\hbar k_L} = \frac{\pi\sqrt{2}k^2}{\lambda\hbar^2} \tag{3.9}$$

This simplistic curve is also plotted in Fig. 3.1. This argument will be developed more fully in Chapter 4. This curve can also be understood in terms of Floquet theory [1]. It provides a simplified estimate of localization length, and is shown in Fig. 3.1, but leaves out a great deal of the physics.

Though naive, Eq. 3.3 and Eq. 3.9 are extremely useful. These two curves intersect at a point called the "quantum crossover" (see 3.1):

$$\lambda_{qc} = (\sqrt{6}\pi)^{\frac{1}{2}}\frac{k}{\sqrt{\hbar}} \tag{3.10}$$

$$\sigma_{qc} = \left[\frac{\sqrt{\langle p^2 \rangle}}{2\hbar k_L}\right]_{qc} = (\frac{2}{3})^{\frac{1}{4}}\frac{\sqrt{\pi}k}{\hbar^{\frac{3}{2}}} \tag{3.11}$$

For initial conditions that are not significantly affected by islands of stability, the saturated momentum distribution is more boxlike if $\lambda < \lambda_{qc}$ and has an exponential characteristic otherwise. In addition, these expressions are useful for exploring parameter space to find realizable experimental conditions. By keeping track of where this crossover occurs, how long it takes to diffuse in momentum space, and how much spontaneous emission occurs, realistic experimental parameters can be found. A more detailed description of the types of constraints will be given in Sec. 4.6.

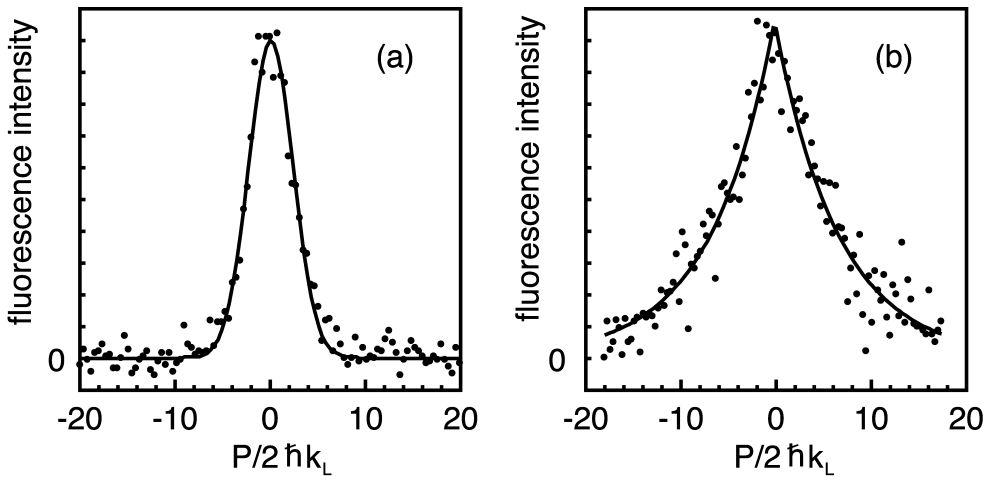

Figure 3.4: The initial condition and an exponentially localized lineshape data (dots) fitted to a Gaussian and exponential, respectively [53].

To realistically compare with experiment, in a collaboration with Dr. Bala Sundaram, we have performed a space-time integration of the Schrödinger equation

$$i\bar{k}\frac{\partial\Psi}{\partial t} = \left[-\bar{k}^2\frac{\partial^2}{\partial\phi^2} - k\cos\left(\phi - \lambda\sin\tau\right)\right]\Psi \tag{3.12}$$

using a standard two-sweep method [54] (we have also used the time-slice method [55]). The variation in k associated with the spatial variation in laser intensity is taken into account. Note that $\bar{k}$ is the scaled Planck's constant. A single particle wavepacket initial condition mimics the ensemble of independent atoms in the experiment for which the width in ρ is Gaussian while the spatial width in ϕ is limited by the spread of the MOT. In our system of scaled units these widths are related by the commutator $[\phi, \rho] = i\bar{k}$, where $\bar{k} = 8\omega_r/\omega_m$. Our choice was a 'squeezed' wavepacket given by

$$\psi(\phi) = (2\pi\mu)^{-1/4} exp\Big[i\left(A(\phi-\phi_0)^2 + \rho_0(\phi-\phi_0)/\bar{k}\right)\Big] \tag{3.13}$$

where (ϕ_0, ρ_0) are the centroid (mean) values and the variances (with respect to (ϕ_0, ρ_0)) are $\langle\Delta\phi^2\rangle = \mu$, $\langle\Delta\phi\Delta\rho + \Delta\rho\Delta\phi\rangle = \alpha\bar{k}$,and $4\mu\langle\Delta\rho^2\rangle = \bar{k}^2(1+\alpha^2)$, from which we get that $A = (i+\alpha)/4\mu$. The widths in ρ and ϕ are independently

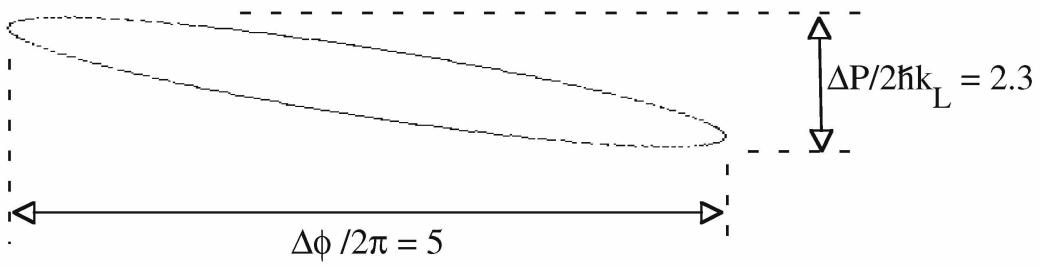

Figure 3.5: The mixed state ensemble initial conditions are mimicked by a pure state squeezed wavepacket of minimal uncertainty. The projection on the momentum axis is $\Delta p/2\hbar k_L = 2.3$ which equals the ensemble initial momentum spread. The ϕ projection is $\Delta\phi/2\pi = 5$. The results do not significantly change as long as $\Delta\phi/2\pi \gg 1$

determined by adjusting α to maintain the minimum uncertainty condition as shown in Fig. 3.5. This initial condition is evolved under the Schrödinger equation for fixed interaction time and $p_{\rm rms}$ is computed. The results are shown by the heavy dashed line in Fig. 3.1 and are in close absolute agreement with experiment with no adjustable parameters. While the ensemble average initial conditions are known, the individual atomic initial conditions are not. Ideally, however, a density matrix approach should be taken. This was not done here due to the intensive computational requirements. In addition, one sees that essentially all of the dynamics can be understood in terms of a single particle wavefunction.

Note that for small values of λ there is good agreement with the classical prediction. At $\lambda = 0$ the system is integrable and momentum is trivially localized. As λ is increased the phase space becomes chaotic, but growth is limited by the RK boundary. Our measured momentum distributions (in Fig. 3.3, bottom panel) are characteristically "boxlike" in this regime. As λ is increased beyond a critical value there are oscillations in localization with an rms spread that deviates substantially from the classical prediction at the peaks. For those values of λ the classical phase space is predominately chaotic, and exponentially

localized distributions are observed because the quantum break time occurs before the RK boundary is reached. This is shown in Fig. 3.3 for $\lambda = 3.0$. At the dips in oscillation, as in the case $\lambda = 3.8$, the classical phase space that overlaps with the initial condition becomes nearly integrable and the measured momentum is close to the classical prediction. In the intermediate regime the phase space is mixed and the momentum distributions exhibit features which can be clearly identified with the underlying classical phase space. In Fig. 3.6a, there is a boxlike distribution with a Gaussian-like peak in the center. This corresponds to part of the initial conditions that are trapped in an island of stability and part that diffuses out to uniformly fill the chaotic phase space within the RK boundary. In Fig. 3.6b λ is larger and the RK boundary is farther away. Now the part of the initial conditions contained in the chaotic domain becomes exponentially localized, while the island structure leads to a similar effect as in Fig. 3.6a. Both figures illustrate the unique potential of this experiment to study issues of structure and transport in a mixed phase space.

To gain further insight into this problem, in a collaboration with Professor Qian Niu and his students Georgios Georgakis and Bob Jahnke, we have also done a quantum Floquet analysis. A Floquet analysis is mathematically equivalent to a Bloch state analysis in a periodic lattice. For this time dependent Hamiltonian, neither energy nor momentum of the particle is conserved. But, since it is periodic in time and space, the eigenstates of our Hamiltonian are most naturally represented using a 2D Floquet state basis,

$$\{\psi(\phi,\tau) = e^{iq\phi}e^{-i\epsilon\tau}u(\phi,\tau)\}. \tag{3.14}$$

Here $u(\phi,\tau)$ reflects the periodic structure of the Hamiltonian; that is,

$$u(\phi+2\pi,\tau) = u(\phi,\tau+2\pi) = u(\phi,\tau). \tag{3.15}$$

q is the quasi-momentum and ϵ is the quasi-energy [56]. Expanding $u(\phi,\tau)$ in a Fourier series, in both the space and time variables, allows us to write the

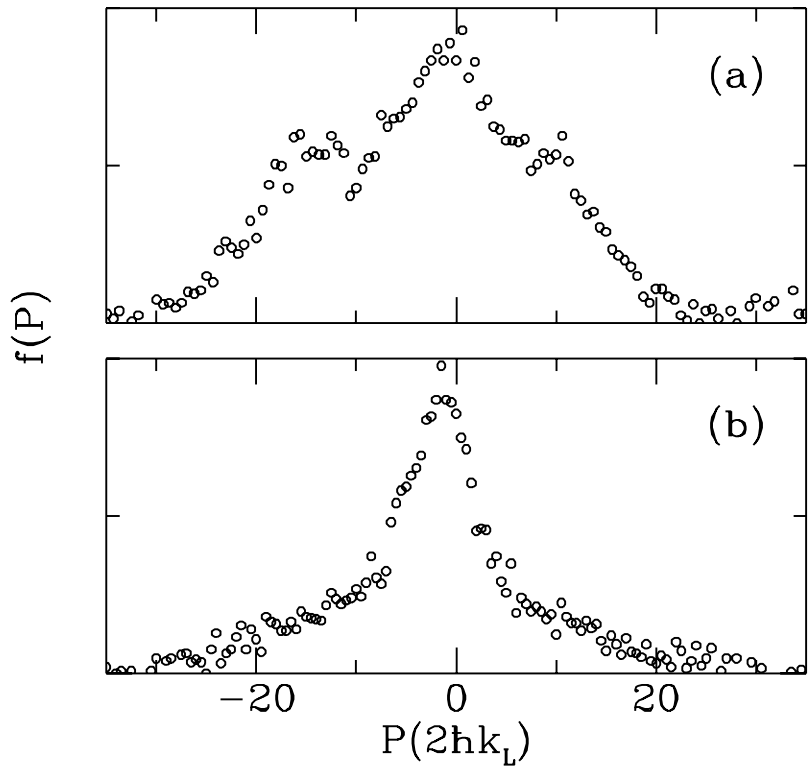

Figure 3.6: Experimental momentum distributions for two cases in a mixed phase space regime. In (a) λ is below the crossover, and growth is limited at the RK boundary. In (b) λ is above the crossover and initial conditions in the chaotic regime are exponentially localized. In both cases initial conditions in islands of stability remain trapped. Note that the vertical scale here is linear [52].

quasienergy-momentum states in the form

$$\psi_\epsilon(\phi,\tau) = \sum_{mn} \psi^\epsilon_{mn}\, e^{i(q+n)\phi}\, e^{-i(\epsilon+m)\tau}, \tag{3.16}$$

where n and m are the integer portions of the quasi-momentum and quasi-energy, respectively. The Schrödinger equation in this representation is then

$$\epsilon\ \psi^\epsilon_{mn} = (-m + \frac{\hbar(n+q)^2}{2})\psi^\epsilon_{mn} - \frac{k}{2\hbar}\sum_{l=-\infty}^{\infty} J_l(\lambda)(\psi^\epsilon_{m-l,n-1} + \psi^\epsilon_{m+l,n+1}) \tag{3.17}$$

For each q, the set of quasienergies and corresponding quasienergy-momentum states are obtained by numerically solving Eq. 3.17. To make contact with the experiment, we use appropriate initial conditions and find the Floquet basis representation. Floquet states that overlap with the initial condition are the only ones that become populated during the time evolution. All of the dynamics of the problem can be understood in terms of these states. The quantities $\hbar(q+n)$ and $\hbar(\epsilon+m)$ are identified respectively with momentum and energy. The solution is then averaged in time to give the long-time results. Since the experimental values are close to saturation, it is valid to compare them with this long-time result. To simplify the Floquet analysis, the small spread in k proportional to laser intensity variations across the ensemble of atoms is approximated by the use of an rms k. The rms momentum spread from the Floquet analysis is shown in Fig. 3.1 (heavy solid line) and the lineshapes are given in Fig. 3.3 (bottom panel). For both cases there is good agreement with experiment over the range of λ with no adjustable parameters.

The Schrödinger equation has the form of a two-dimensional tight-binding "eigenenergy" (ϵ) equation with "site energy" $-m + \hbar(q+n)^2/2$ and hopping terms of energy $k/2\hbar$. For a given state, the "site energy" can not differ from the "eigenenergy" by much more than the "hopping energy". Since we can choose both ϵ and q to be within the interval [-1/2, 1/2], each wavefunction is confined to a parabolic strip centered about the curve $(\epsilon+m) = \hbar(q+n)^2/2$ as shown in Fig. 3.7. The points along the parabola denote the expectation

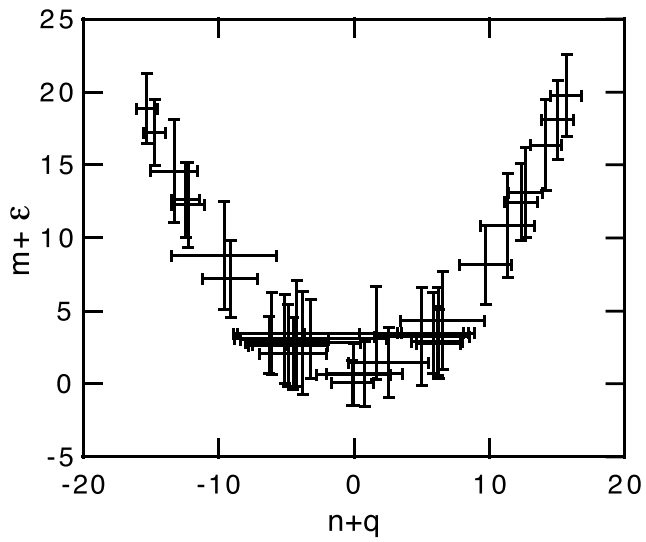

Figure 3.7: Positions and rms widths of the Floquet states in the $(\epsilon+m, q+n)$ space for $\lambda = 5.0$, $k = 0.37$, $\bar{k} = 0.16$ [52].

values of $\epsilon + m$ and $q + n$ for each Floquet state. The error bars denote the corresponding rms widths. With the locus of states confined to a region about the parabola the problem is essentially reduced to one dimension. Furthermore, along this quasi-1D array of points there is no apparent order, which is reminiscent of the disordered lattice underpinning the theory of Anderson localization [57]. Beyond this connection to condensed matter physics, our system is directly analogous to the current-driven Josephson junction [21], and heating of a Bloch electron in an AC field [58], and can serve as a testing ground without the complications of impurities, multi-particle interactions, and thermal effects. The measured localized distributions can represent an individual atomic wave packet which was generated by the time dependent Hamiltonian. Generation of such "Floquet packets" constitutes a new direction in coherent atom optics using tailored time dependent potentials. Future directions will be discussed in Chapter 6.

Chapter 4

δ-Kicked Rotor (Amplitude Modulation)

4.1 Introduction

The classical kicked rotor and the equivalent standard mapping is a textbook paradigm for Hamiltonian chaos [59]. The quantum δ-kicked rotor (QKR) has played an equally important role for the field of quantum chaos, and a wide range of effects have been predicted [60]. This work is the first direct experimental realization of the QKR, and the first observation of the onset of dynamical localization in time, the quantum break time, and quantum resonances.

To understand the model of the δ-kicked rotor, consider a particle of mass M that is free to rotate in a plane at a fixed distance from a pivot point (see Fig 4.1). The rotor is kicked periodically with an impulse in a fixed direction. This kick could be thought of as periodically turning on the force of gravity, for example. The projection of the force along the direction of the motion provides a nonlinear (cosine) potential. Depending on the parameters, this system can exhibit classical chaos. It is an extremely simple system, and yet displays a rich variety of phenomena. The atom-optics realization is obviously not a rotor but is similar in that its phase space is periodic in position and the interaction produces only quantized momentum changes.

Consider again the conservative Hamiltonian for the ground state

$$H = \frac{p^2}{2M} - f(t)\frac{\hbar\Omega_{eff}}{8}\cos 2k_L x \tag{4.1}$$

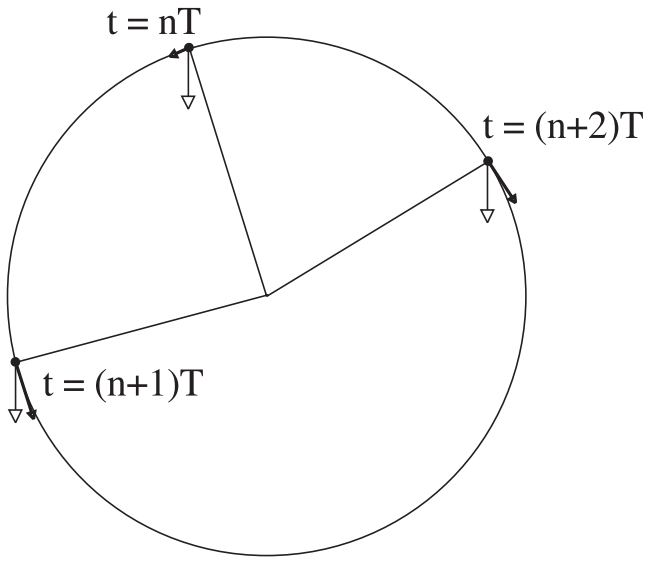

Figure 4.1: The kicked rotor.

We now assume that the potential term in the Hamiltonian is multiplied by $f(t)$, a train of N pulses with unit peak heights and period T (see Fig 4.2). To make a connection with the δ-kicked rotor, these pulses should ideally be in the form of Dirac-δ functions. Obviously this is not possible experimentally, but if the atoms do not move appreciably during the pulse the system is a good approximation to the δ-kicked rotor. This limitation simply puts an upper limit on momentum that can be considered. The nonzero pulse widths lead to a finite number of resonances in the classical dynamics [61], which limits the diffusion resulting from overlapping resonances to a band in momentum. Resonance overlap will be discussed in more detail in Chapter 5. By decreasing the pulse duration with constant area, however, the width of this band can be made arbitrarily large, approaching the δ- function pulse limit. We illustrate this by considering a train of Gaussian pulses. The Hamiltonian is given by

$$\mathcal{H} = \rho^2/2 - k\cos\phi \sum_{n=0}^{N} e^{-(\tau-n)^2/2\alpha^2} \,, \tag{4.2}$$

where the scaled variables are $\phi = 2k_L x$, $\rho = (2k_L T/M)\, p$, $\tau = t/T$, $\mathcal{H} =$

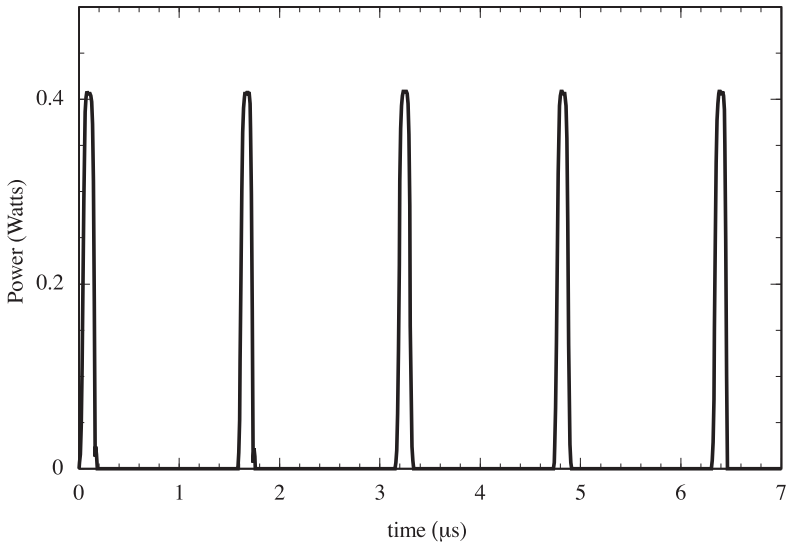

Figure 4.2: Digitized temporal profile of the pulse train measured on a fast photo-diode. The vertical axis represents the power in one laser beam of the standing wave. $f(t)$ and Ω_{eff} are derived from this scan [62].

$(4k_L^2T^2/M)\,H$; T is the spacing between the pulses; α is the pulse width and $k = \Omega_{\text{eff}}\omega_r T^2$ where $\omega_r = \hbar k_L^2/2M$ is the recoil frequency. In the quantized model ϕ and ρ are the conjugate variables satisfying the commutation condition $[\phi, \rho] = i\bar{k}$, where $\bar{k} = 8\omega_r T$. This scaling is identical to that of Chapter 3 with the replacement of ω_m by $2\pi/T$.

4.2 Standard Map Analysis

Hamilton's equations of motion for Eq. 4.1 are

$$\frac{\partial \mathcal{H}}{\partial \rho} = \dot{\phi} = \rho \tag{4.3}$$

$$\frac{\partial \mathcal{H}}{\partial \phi} = -\dot{\rho} = k \sin\phi \sum_{n=-\infty}^{\infty} e^{-\frac{(\tau-n)^2}{2\alpha^2}} \tag{4.4}$$

integrating Eq. 4.3 over one period gives

$$\Delta\phi = \int_{n-\frac{1}{2}}^{n+\frac{1}{2}} d\tau\rho = \rho \int_{n-\frac{1}{2}}^{n+\frac{1}{2}} d\tau = \rho \tag{4.5}$$

which is valid assuming that ρ does not change appreciably except during the kick. Integrating Eq. 4.4 over one period gives

$$\Delta\rho = -\int_{n-\frac{1}{2}}^{n+\frac{1}{2}} d\tau k \sin\phi \sum_{n=-\infty}^{\infty} e^{-\frac{(\tau-n)^2}{2\alpha^2}}. \tag{4.6}$$

If ϕ does not change appreciably during during a kick and $\alpha \ll 1$,

$$= -k \sin\phi \int_{-\frac{1}{2}}^{\frac{1}{2}} d\tau e^{-\frac{\tau^2}{2\alpha^2}}. \tag{4.7}$$

If we define $\zeta = \tau/\sqrt{2}\alpha$, then

$$= \sqrt{2\pi}\alpha k \sin\phi \left[\frac{2}{\sqrt{\pi}} \int_0^{\frac{1}{2\sqrt{2}\alpha}} d\zeta e^{-\zeta^2}\right], \tag{4.8}$$

where we recognize the quantity in square brackets as the error function (erf)

$$= \sqrt{2\pi}\alpha k \sin(\phi) \mathrm{erf}\left(\frac{1}{2\sqrt{2}\alpha}\right) \tag{4.9}$$

for narrow pulses ($\alpha \ll 1$) we find

$$\Delta\rho = \sqrt{2\pi}\alpha k \sin(\phi) \tag{4.10}$$

The discretized version of Eq. 4.5 and Eq. 4.10 gives us:

$$\phi_{n+1} = \phi_n + \rho_{n+1} \tag{4.11}$$

$$\rho_{n+1} = \rho_n - K \sin\phi_n \tag{4.12}$$

Where $K = \sqrt{2\pi}\alpha k$ is identified as the classical stochasticity parameter, and Eq. 4.11 and Eq. 4.12 as the Taylor-Chirikov or 'standard' map [63], which has been studied extensively. For small K the motion in phase space is bounded and chaotic in some regions. If K is above 1 global diffusion in phase space takes place. If K is above 4 islands of stability vanish and global chaos occurs [59]. In the limit of large K, angular correlations can be ignored after one kick, and

one can easily iterate the map to estimate the diffusion constant. Iterating over τ kicks,

$$\langle(\rho_\tau - \rho_0)^2\rangle = K^2 \sum_{m=0}^{\tau-1} \langle \sin \phi_m{}^2 \rangle + K^2 \sum_{m \neq m'}^{\tau-1} \langle \sin \phi_m \sin \phi_{m'} \rangle \quad (4.13)$$

$$= \frac{K^2}{2}\tau \quad (4.14)$$

Where the diffusion constant D is identified as

$$D = \frac{K^2}{2} \quad (4.15)$$

Thus for diffusion in momentum:

$$\langle \rho^2 \rangle = D\tau \quad (4.16)$$

In units of $2\hbar k_L$ the diffusion constant becomes $K^2/2\hbar^2$, and is divided by 2, since what is plotted is actually energy ($\langle\rho^2\rangle/2\hbar^2$), as shown in Fig. 4.7. Classically this diffusion continues indefinitely in the limit that $\alpha \to 0$ and $k \to \infty$ such that αk remains finite (the δ-kicked limit). The effect of finite-width kicks, however, produces an effective reduction in K as ρ increases (see Sec. 4.3), because if the particle moves significantly with respect to the spatial period of a well during a pulse, the average force is greatly reduced.

Quantum mechanically the situation is quite different. Chirikov, Izrailev and Shepelyansky [64], showed that classical diffusion is suppressed after the time that is required to resolve the discrete nature of the eigenstates. One assumes that classical diffusion takes place on scales smaller than the localization length ξ. After the wavepacket spreads over ξ momentum states, quantum suppression due to dynamical localization takes place. Eq. 4.16 gives us

$$D\tau^* = (\xi\hbar)^2 \quad (4.17)$$

where τ^* is called the quantum break time. Since $\Delta\omega\tau^* \approx 1$, where $\Delta\omega \approx 1/\xi$ is the separation between quasienergies, it follows that $\tau^* = \xi$, from which

Eq. 4.17 gives $D\xi = \xi^2\bar{k}^2$. So one finds that ξ is equal to $D/\bar{k}^2$ up to a constant. The heuristic nature of this argument cannot predict the constant. Shepelyansky numerically found this constant to be 1/2 for all the models that he studied [65], consequently

$$\xi = \frac{D}{2\bar{k}^2} \tag{4.18}$$

In dimensionless momentum units this gives $\rho^* \equiv \xi\bar{k}$, and in units of $2\hbar k_L$ the localization length becomes

$$\frac{p^*}{2\hbar k_L} = \frac{K^2}{4\bar{k}^2}. \tag{4.19}$$

and the break time in units of periods is

$$\tau^* = \frac{K^2}{4\bar{k}^2} \tag{4.20}$$

The localization length denotes the $1/e$ point of $\Psi^*\Psi$ for an exponential distribution, but the experiment measures rms momentum, it is therefore better to compare $\sigma^* = \sqrt{2}p^*$ which results in

$$\frac{\sigma^*}{2\hbar k_L} = \frac{K^2}{2\sqrt{2}\bar{k}^2} \tag{4.21}$$

4.3 Effect of Pulse Shape

In these units, the time dependent potential of Eq. 4.1(for an infinite train of pulses) can be rewritten as a discrete Fourier series, leading to

$$\mathcal{H} = \frac{\rho^2}{2} - \sqrt{2\pi}\alpha k \sum_{r=-\infty}^{\infty} e^{-2\pi^2\alpha^2 r^2} \cos\left(\phi - 2\pi r\tau\right), \tag{4.22}$$

In the limiting case of zero width such that the area under the pulse remains fixed, i.e. $\alpha \to 0, k \to \infty$ such that αk remains finite, all the Fourier weights are equal and using the Poisson sum rule, one gets

$$\mathcal{H} = \frac{\rho^2}{2} - K\cos\phi \sum_{n=-\infty}^{\infty} \delta(\tau - n) \tag{4.23}$$

which is the kicked rotor with classical stochasticity parameter $K = \sqrt{2\pi}\alpha k$.

Looking at Eq. 4.22, the resonances are located at $\rho = d\phi/d\tau = 2\pi r$ and the widths

$$K_{eff} \equiv \sqrt{2\pi}\alpha k e^{-2(\pi\alpha r)^2} \tag{4.24}$$

of successive resonances fall off because of the exponential factor, thus defining the borders to diffusion as KAM curves (quasi-integrable behavior). The fall-off is governed by the pulse width, parametrized by α. Successive resonances are affected by the temporal pulse shape though K in the central region depends only on the integrated area of the pulse. The actual digitized pulse profile is numerically integrated to provide K. If Gaussian pulses are assumed, then the effective stochasticity parameter falls off as p increases. From Eq. 4.22

$$K_{eff} = \sqrt{\frac{\pi}{4\ln 2}}\frac{\Delta T_{\rm fwhm}}{T}k \exp -(\frac{2\omega_r}{\sqrt{\ln 2}}\Delta T_{\rm fwhm}\frac{p}{2\hbar k_L})^2 \tag{4.25}$$

where $\Delta T_{\rm fwhm}$ is the full-width-half-maximum duration of the pulse. If, on the other hand, the pulse was modeled as a square pulse, then

$$K_{eff} = \frac{\Delta T_{\rm fwhm}}{T}k\frac{\sin{(4\omega_r\Delta T_{\rm fwhm}\frac{p}{2\hbar k_L})}}{(4\omega_r\Delta T_{\rm fwhm}\frac{p}{2\hbar k_L})}. \tag{4.26}$$

An actual temporal pulse shape is shown in Fig. 4.3. The experimental rolloff in K is somewhat different than for an ideal Gaussian or square pulse (see Fig 4.4). The details of the rolloff are not important. To make the connection with the δ-kicked rotor it is only important that K is roughly constant over the region of interest.

4.4 Quantum Break Time and Dynamical Localization

We show results for $\Omega_{eff}/2\pi = 75.6$ MHz, and $T = 1.58$ μs. Each pulse has a rise and fall time of 25 ns and a temporal full width at half maximum of $\Delta T_{\rm fwhm} = \alpha T/2\sqrt{2\ln 2} = 98$ ns. The effective impulse corresponds to $K = 11.6$ and the corresponding classical phase portrait is shown in Fig. 4.5 with the classical boundary at $p/2\hbar k_L \approx 45$ (which is consistent with the estimated

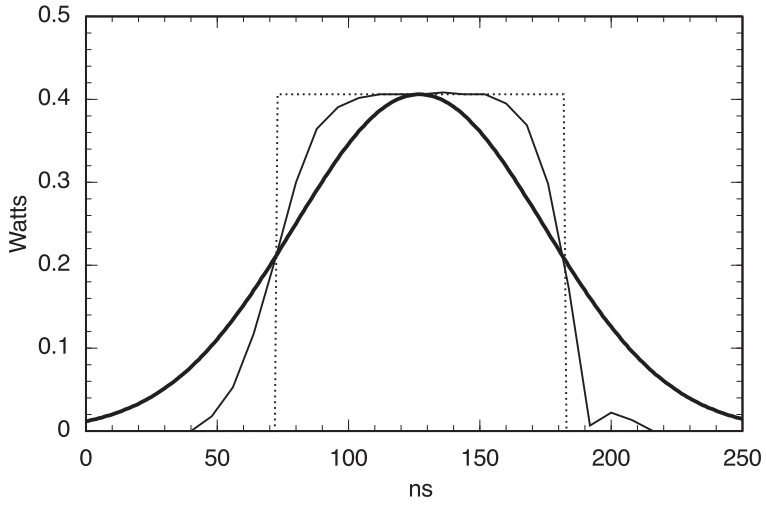

Figure 4.3: Digitized temporal profile of one pulse from Fig. 4.2 measured on a fast photo-diode, compared to an ideal Gaussian and square pulse with the same FWHM and peak height. The vertical axis represents the power in one laser beam of the standing wave. $f(t)$ and Ω_{eff} are derived from this scan.

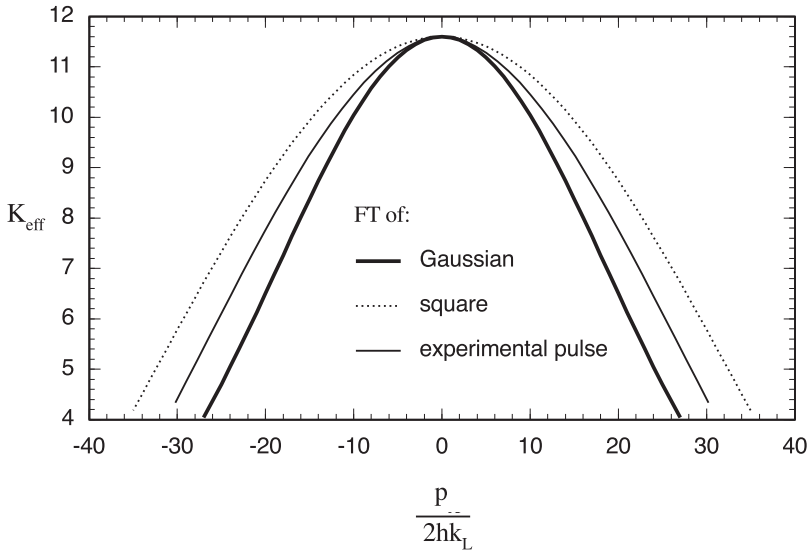

Figure 4.4: The Fourier transform of the temporal profiles shown in Fig. 4.3, showing the falloff of K for the various cases. Note that the falloff in K is small over the localization length ($\sigma^*/2\hbar k_L = 11.6$)

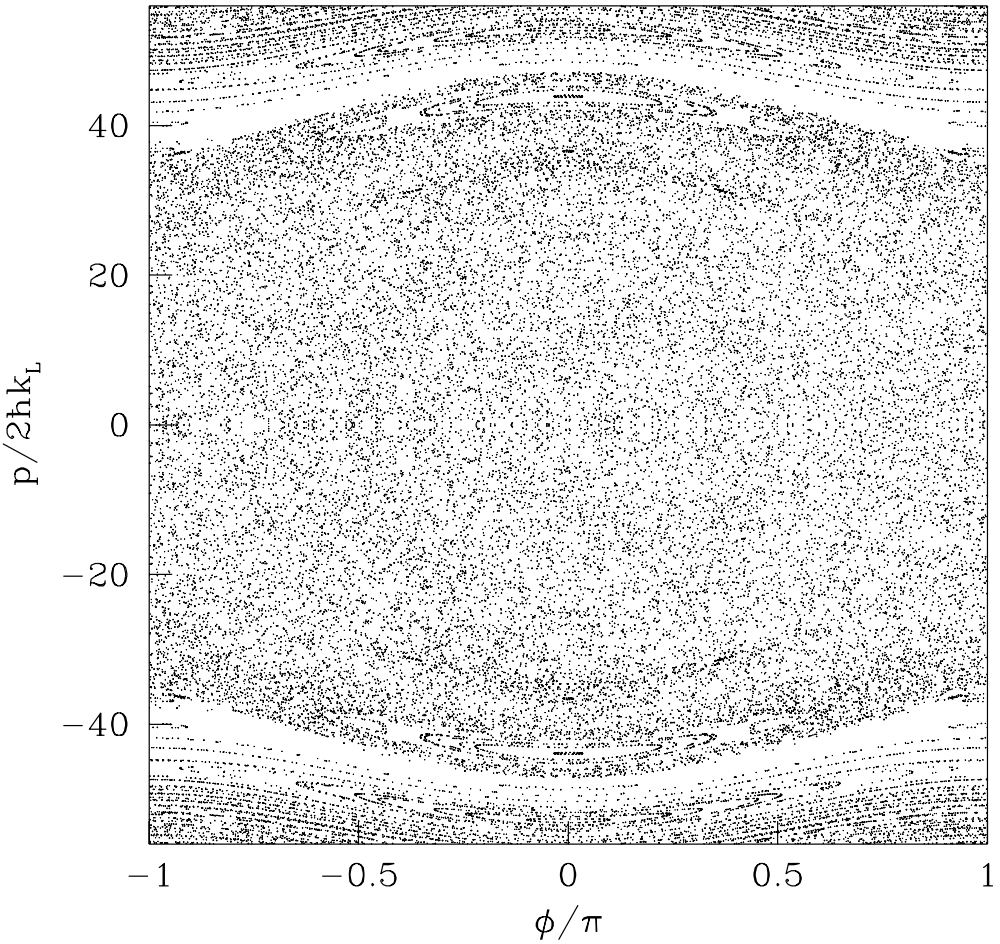

Figure 4.5: Classical phase portrait for the pulsed system using a train of Gaussians to represent the experimental sequence. The integrated area under a single pulse is taken to be the same as in the experiment. The standing wave has a spatial rms value of $\Omega_{eff} = 75.6$ MHz. $T = 1.58$ μs, and $\Delta T_{\text{fwhm}} = 98$ ns leading to $K = 11.6$ [62].

rolloff in K falling below 1, indicating the appearance of KAM surfaces). The variation in K in the vicinity of the boundary depends on the exact pulse shape, while the central chaotic domain (where the impulse approximation is valid) is sensitive only to the area of the pulse. The scaled Planck's constant $\bar{k}$ equals 2.0. For these experimental parameters, the theoretical estimate of the localization length ξ (the $1/e$ point of the momentum distribution) is 8.3 in units of $2\hbar k_L$. The fall-off in K over the localization length is small, $\approx 15\%$. Thus, the experimental conditions are in a regime well-described by the QKR.

The momentum distributions were measured for an increasing number of kicks (N), with the pulse height, period, and pulse duration fixed. The lineshapes shown in Fig. 4.6 clearly evolve from an initial Gaussian distribution at $N = 0$ to an exponentially localized distribution after approximately $N = 8$. We have measured distributions out until $N = 50$ and find no further significant change. Since the atoms in the ensemble are independent, these results should represent the single-atom wave function. The growth of $< (p/2\hbar k_L)^2 > /2$ as a function of the number of kicks was calculated from the data and is displayed in Fig. 4.7. It shows diffusive growth initially until the quantum break time, after which dynamical localization is observed [60]. The calculated classical diffusion rate and localization are also plotted. Classical and quantum calculations (not shown here) both agree with the data over the diffusive regime. Beyond the quantum break time, the classical energy continues to increase diffusively while the measured lineshapes stop growing, in agreement with the quantum prediction. The localized lineshape observed is shown (Fig. 4.7 inset), and is clearly exponential. These results are the first experimental confirmation of the quantum break time.

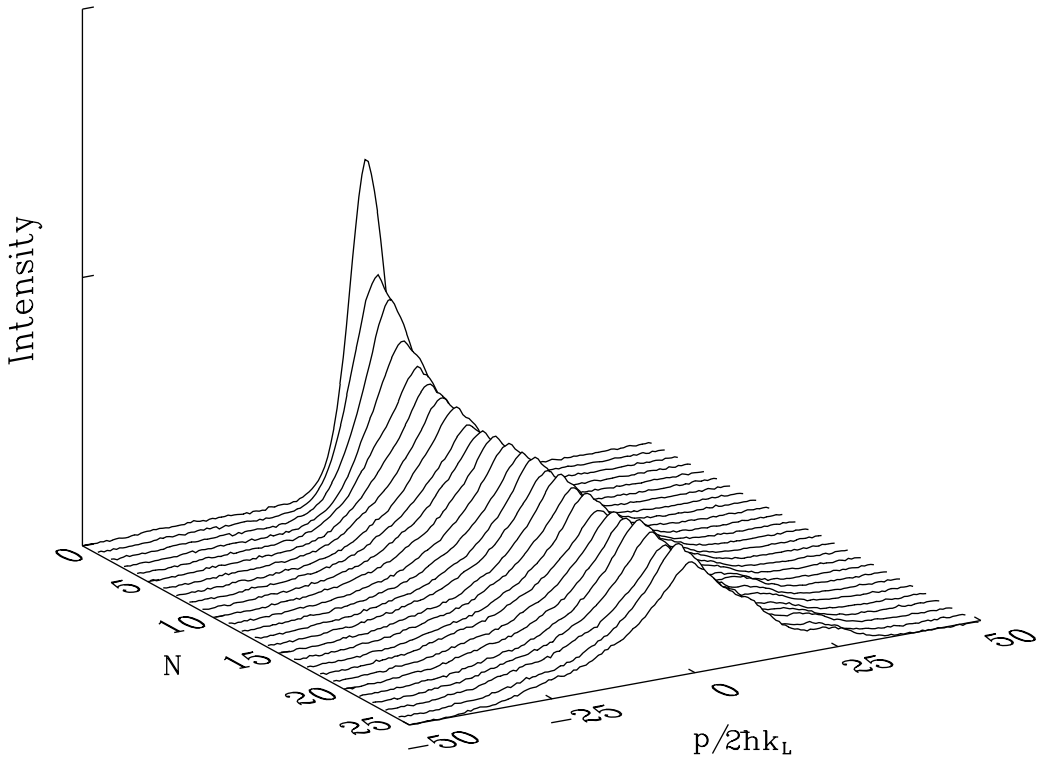

Figure 4.6: Experimental time evolution of the lineshape from the initial Gaussian until the exponentially localized lineshape. The parameters are the same as Fig. 4.5 with $\bar{k} = 2.0$. The break time is approximately 8 kicks. Note that a small intensity variation due to spatial overlap of atoms and laser profile results in a somewhat smaller K than at peak field. The vertical scale is measured in arbitrary units and is linear [62].

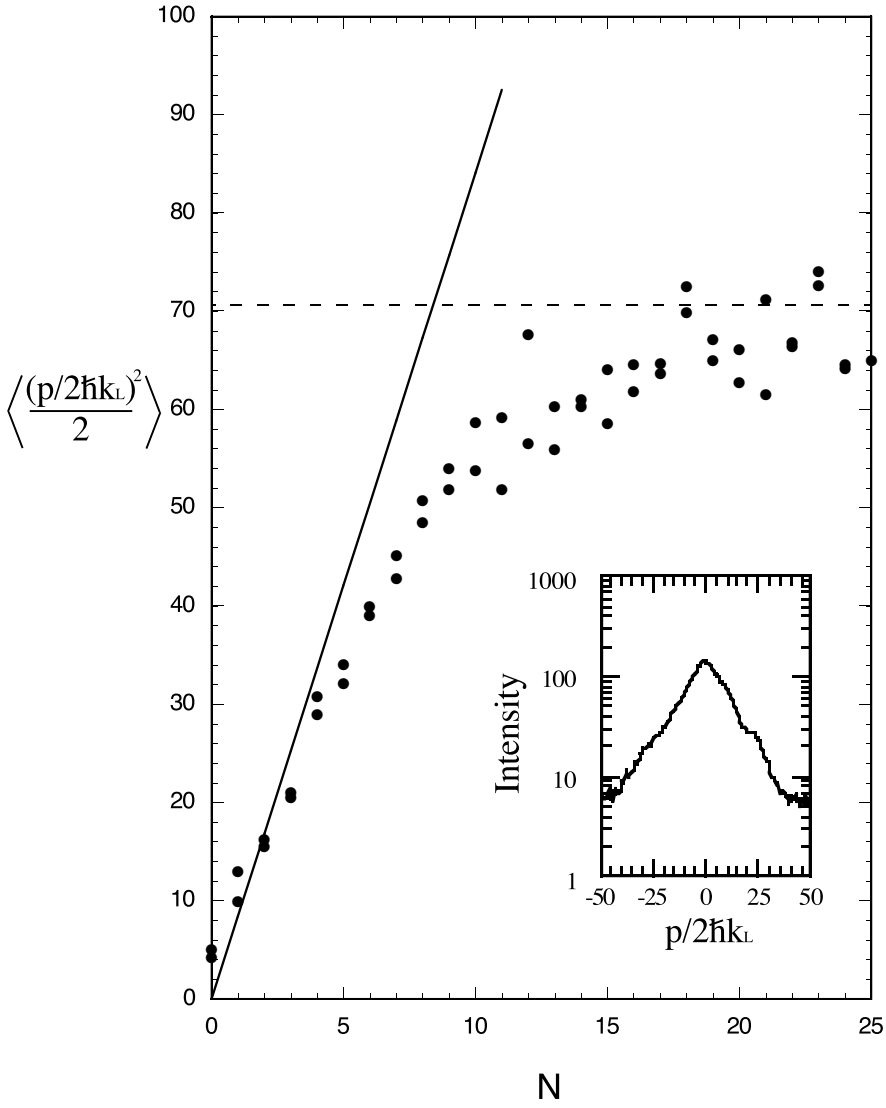

Figure 4.7: Energy $< (p/2\hbar k_L)^2 > /2$ as a function of time. The solid dots are the experimental results. The solid line shows the linear growth proportional to the classical diffusion constant $K^2N/4k^2$. The dashed line is the saturation value computed from the theoretical localization length ξ which in these units is $K^4/16k^4$. The inset shows an experimentally measured exponential lineshape on a logarithmic scale which is consistent with the prediction $\xi = K^2/4k^2 \approx 8.3$ [62].

4.5 Quantum Resonances

Between kicks the atoms undergo free evolution for a fixed duration. The quantum phase accumulated during the free evolution is

$$e^{-ip^2T/2M\hbar} = e^{-i\rho^2/2\hbar} = e^{-in^2\hbar/2}, \tag{4.27}$$

where $n = \rho/\hbar$ labels the plane-wave basis. A *quantum resonance* occurs when $\hbar/2$ $(= 4\omega_r T)$ is chosen to be a rational multiple of 2π. We have scanned T from 3.3 μs to 50 μs in 150 steps and find quantum resonances when the quantum phase is an integer multiple of π. Other resonances should occur for $\hbar = 2\pi r/s$ but these are not resolved experimentally.

For even multiples, the free evolution factor between kicks is unity, and for odd multiples, there is a flipping of sign between each kick [66]. Quantum resonances have been studied theoretically, and it was shown that instead of localization, one expects energy to grow quadratically with time since the atom has the same phase for each kick and hence they all add [67]. This picture, however, is only true for an initial plane wave. A general analysis of the quantum resonances shows that for an initial Gaussian wavepacket, or for narrow distributions not centered at $p = 0$, the momentum distribution is actually smaller than the exponentially localized one, and settles in after a few kicks [68]. Our experimental results are shown in Fig. 4.8. Ten quantum resonances are found for T ranging between 5 μs (corresponding to a phase shift of π) and 50 μs (10π) in steps of 5 μs. The saturated momentum lineshapes as a function of T are shown in Fig. 4.9. The narrower, non-exponential profiles are the resonances between which the exponentially localized profiles are recovered. The time evolution of the lineshape at a particular resonance is shown in Fig. 4.8 from which it is clear that the distribution saturates after very few kicks. We also observe the difference in early time evolution ($2-3$ kicks) when $\hbar/2$ equals odd multiples of π, arising from the alternating sign between kicks.

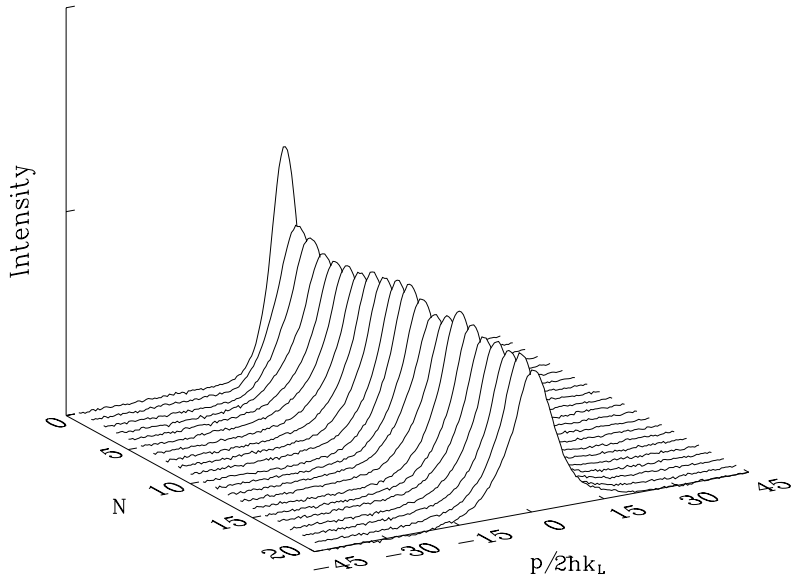

Figure 4.8: Time evolution of a particular resonance ($T = 10$ μs corresponding to $\bar{k} = 4\pi$). The parameters ΔT_{fwhm} and $\Omega_{eff}/2\pi$ are the same as in the other figures. [62]

4.6 Selecting Experimental Parameters

Simple algebraic expressions for physical quantities are extremely useful in designing experiments, because numerical simulations are too time consuming to explore parameter space. Limitations on the input parameters greatly reduce the search. Laser power (P) available at the atoms, taking into account AOM and spatial filter losses, is limited to about 0.4 W which can be retro-reflected to form the standing wave. In general, more power is better, since it allows one to detune further and reduce spontaneous emission for a given well depth. The laser detuning ($\delta_L/2\pi$) should be much greater than 1.7 GHz so that effect of incomplete optical pumping is minimized, but much less than 500 GHz if detuned to the red to avoid the sodium D_1 line. The laser spot size (w_o) must be much larger than the spatial spread of the atoms but cannot be too large due to limited available laser power. The pulse period (T) must be chosen to avoid or match the quantum resonance condition depending on the experiment.

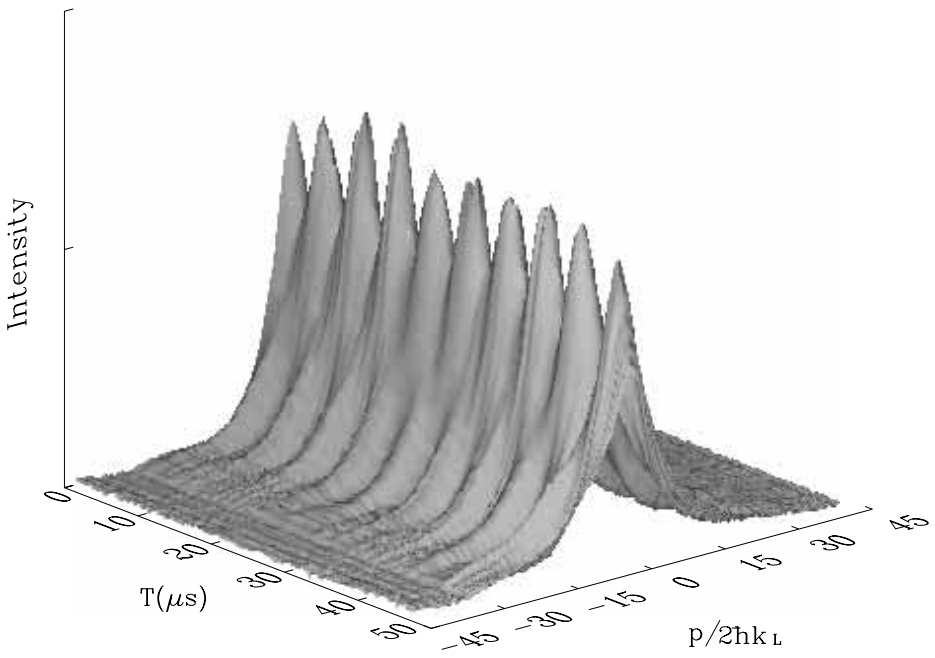

Figure 4.9: Experimental observation of quantum resonances as a function of the periodicity of the pulses. The surface plot is constructed from lineshapes corresponding to 150 different values of T, after 25 kicks. This value of N ensures that the lineshapes are saturated for the entire range of T shown. At resonance, the profiles are non-exponential and narrower than the localized shapes which appear off-resonance. Note that the vertical scale is linear. [62]

The fwhm of the pulse (τ) can be no less than 50 ns without a large cost in peak power with available AOMs. Finally, the angle between the beams (θ) that make up the standing wave is limited to values set by the geometry of the vacuum chamber, but was kept at 180° (counterpropagating) for simplicity.

For $\theta < 180°$, the periodicity of the standing wave is increased. The result is a smaller wavevector $k'_L = k_L \sin(\theta/2)$ that leads to a reduced recoil momentum $\hbar k'_L$. The classical stochasticity parameter for a Gaussian pulse characterized by $\Delta T_{\text{fwhm}} = \alpha T/2\sqrt{2\ln 2}$ is

$$K_{Gaussian} = \frac{\sqrt{\pi}}{2\sqrt{\ln 2}}\Omega_{eff}\omega_r \Delta T_{\text{fwhm}} T \sin^2(\frac{\theta}{2}) \tag{4.28}$$

For a square pulse characterized by a width ΔT_{fwhm} it is 6% less, due to the difference in integrated area of the two pulses, and hence has a stochasticity parameter of

$$K_{square} = \Omega_{eff}\omega_r \Delta T_{\text{fwhm}} T \sin^2(\frac{\theta}{2}) \tag{4.29}$$

Though an experimental pulse is neither Gaussian nor square, the square K is used because the integrated area of an experimental light pulse matched that of a square pulse with the same peak and fwhm to within a percent. To avoid complications of KAM surfaces and islands of stability, peak K must be larger than 4. The scaled Planck's constant is

$$\bar{k} = 8\omega_r T \sin^2(\frac{\theta}{2}) \tag{4.30}$$

The initial condition rms is $\sigma_{ic} = 2.3\hbar k_L$. If the angle of the beams were other than 180°, the initial condition projected onto the reduced effective recoil would be

$$\frac{\sigma_{ic}}{2\hbar k'_L} = \frac{2.3}{\sin(\frac{\theta}{2})} \tag{4.31}$$

Note that this expression does not have the quadratic dependence on $\sin(\theta/2)$. The different functional dependence on θ makes it a useful tool in designing an

experiment. From Sec. 4.3, the break time measured in periods is

$$\tau^* = \frac{K^2}{4\bar{k}^2}. \tag{4.32}$$

The rms momentum corresponding to the localization length is

$$\frac{\sigma^*}{2\hbar k'_L} = \frac{K^2}{2\sqrt{2}\bar{k}^2} \tag{4.33}$$

This quantity must be much larger than the rms initial condition ($\sigma^* \gg \sigma_{ic}$) for good signal to noise. Since the pulses are of finite width, the effective stochasticity parameter is reduced as momentum increases. The simplest estimate for the maximum allowable momentum is when an atom travels one period of the well while the pulse is on (reducing the force dramatically by averaging). This gives

$$\frac{p_{max}}{2\hbar k'_L} = \frac{2\pi T}{\Delta T_{\text{fwhm}}\bar{k}} = \frac{\pi}{4\Delta T_{\text{fwhm}}\omega_r} \tag{4.34}$$

A better estimate is based on Eq. 4.25. From this, we see that the effective stochasticity parameter falls below 4, resulting in islands of stability, when the momentum exceeds

$$\frac{p^{(4)}}{2\hbar k'_L} = \frac{\sqrt{\ln(2)\ln(\frac{K}{4})}}{2\omega_r \Delta T_{\text{fwhm}}} \tag{4.35}$$

A more accurate formula can be derived using island overlap criterion, but as it turns out, this one is suffices. In addition, the actual functional form of the pulse would be needed if more accuracy is required. When the momentum exceeds

$$\frac{p^{(1)}}{2\hbar k'_L} = \frac{\sqrt{\ln(2)\ln(K)}}{2\omega_r \Delta T_{\text{fwhm}}}, \tag{4.36}$$

the stochasticity parameter is less than 1, and KAM surfaces start to appear, blocking momentum diffusion altogether. For the δ-function approximation to be valid, it is necessary to have $p_{max} \gg \sigma^*$. When dissipation is not desired it is necessary to keep the probability of spontaneous emission (N) much less than 1 per break time. This probability is

$$N = \frac{\Omega_{eff}\delta_L \gamma \Delta T_{\text{fwhm}} \tau^*}{4\left[(2\delta_L)^2 + \gamma^2\right]} \tag{4.37}$$

where $\gamma/2\pi = 10$ MHz is the natural linewidth. The total duration of the interaction needs to be kept below about 100 μs for two reasons. First, due to phase instability of the standing wave, there is about 100 mRad. drift in 100 μs. Second, for a time-of-flight measurement to be valid, the particle motion during the interaction must be much less than during the free drift time. Unfortunately there are more constraints on the parameters than there are free parameters, so some compromise is always necessary in designing an experiment.

Chapter 5

Single Pulse (Amplitude Modulation)

5.1 Single Pulse

As we have seen, time-dependent Hamiltonian dynamics exhibit a wide range of novel effects in both classical and quantum domains [59, 60]. Possibly the simplest time-dependent potential is the turning on and off of an interaction. Even here, our intuition is clear only for the two extreme cases of fast passage and adiabatic interactions. However, the majority of cases fall between these limits and it is therefore important to develop intuition and simple physical pictures at these intermediate timescales. One question that comes to mind is: can a single-pulse standing wave induce chaos in atomic motion? It is shown here that when the interaction is nonlinear, the mere act of turning on and off a potential in this intermediate regime can lead to classical chaos. Further, a clean experimental demonstration of the classical mechanism of resonance overlap [69, 70, 71] is given which leads to classically diffusive growth. When quantum mechanics is included, the chaotic growth is ultimately suppressed due to the quantum effect of dynamical localization, though for short times classical and quantum analyses agree.

The nonlinear interaction considered here is a single pulse of a one-dimensional standing wave of light. This type of time-dependent interaction is ubiquitous and occurs, for example, whenever an atomic beam passes through

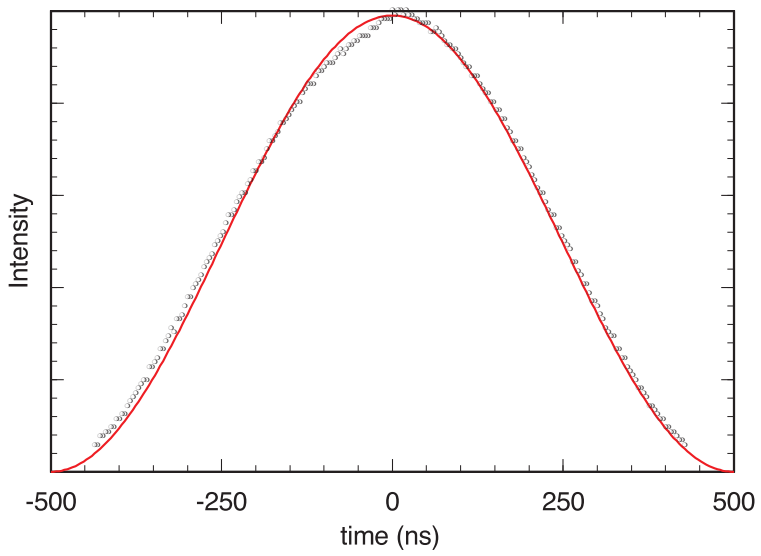

Figure 5.1: Experimentally measured $f(t) = \sin^2 \omega_m t/2$ pulse profile corresponding to $T_s = 2\pi/\omega_m = 1\mu$s together with a fit to an ideal $\sin^2$ pulse.

a standing wave of light. Consider again Eq. 1.15

$$H = \frac{p^2}{2M} - \frac{\hbar\Omega_{eff}}{8} f(t) \cos 2k_L x \tag{5.1}$$

We consider here the case where

$$f(t) = \sin^2 (\frac{\omega_m t}{2}) \tag{5.2}$$

where ω_m is a radio frequency. In the experiment, only a single pulse of duration $T_s = 2\pi/\omega_m$ is used. The exact form of $f(t)$ is measured on a fast photo-diode giving the amplitude as a function of time, which is then digitized and stored (see Fig. 5.1). The profile was also checked on an electronic spectrum analyzer to determine spectral purity. The spectrum consists of the fundamental at a frequency of $1/T_s$, and the second harmonic is 20 dB lower. The effect of the second harmonic on the analysis of nonlinear resonances is small and is within our experimental uncertainty. Higher harmonics are negligible. For the purposes of this analysis it can thus be considered a pure $\sin^2$ pulse.

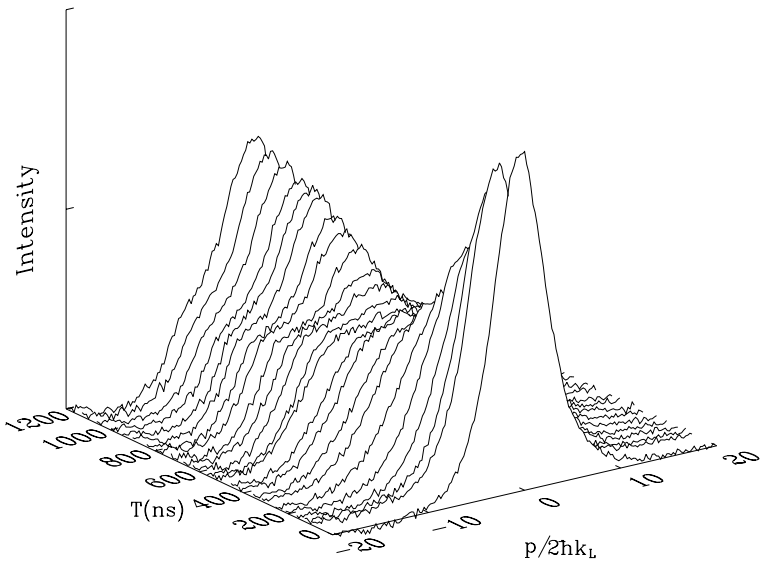

Figure 5.2: Experimentally measured momentum lineshapes as a function of pulse duration. The curve at time zero corresponds to the initial condition. The spatial RMS value of $\Omega_{eff}/2\pi = 50.7$ MHz [72].

The measured atomic momentum distributions as a function of pulse duration T_s are shown in Fig. 5.2. For short interaction times, the final distribution is nearly identical to the initial one ($T_s = 0$) indicating the fast passage limit. With increasing pulse duration the lineshape broadens, and undergoes a transition to a flat, broad lineshape. For a pulse duration of 1 μs the lineshape becomes exponential which is a signature of dynamical localization within a bounded region of momentum. For even longer times the distribution becomes narrow and asymptotically approaches the initial lineshape as expected in the adiabatic limit.

At first sight the dependence of momentum spread on pulse duration appears counterintuitive, and clearly points to new physics that is occurring at intermediate time scales between the limits of fast passage and adiabatic interactions. As will be show below, this behavior is strongly correlated with changes in the classical dynamics. To analyze our problem, we Fourier expand

the Hamiltonian

$$H = \frac{p^2}{2M} - \frac{\hbar\Omega_{eff}}{8}\sin^2\left(\frac{\omega_m t}{2}\right)\cos 2k_L x \ , \tag{5.3}$$

and obtain

$$H = \frac{p^2}{2M} - \frac{\hbar\Omega_{eff}}{16}\left[\cos 2k_L x - \frac{1}{2}\cos 2k_L(x - v_m t) - \frac{1}{2}\cos 2k_L(x + v_m t)\right] \ , \tag{5.4}$$

where $v_m = \lambda_L\omega_m/4\pi$. The effective interaction is that of a stationary wave with two counter-propagating waves moving at $\pm v_m$.

It is convenient to switch to scaled variables $\tau = \omega_m t, \quad \phi = 2k_L x$, $\rho = (2k_L/M\omega_m)p, \quad$ and $\mathcal{H} = (4k_L^2/M\omega_m^2)H$ in terms of which

$$\mathcal{H} = \frac{\rho^2}{2} - k\left[\cos\phi - \frac{1}{2}\cos(\phi + \tau) - \frac{1}{2}\cos(\phi - \tau)\right] \ , \tag{5.5}$$

where $k = \omega_r\Omega_{eff}/2\omega_m^2$ [1, 53, 52], and $\omega_r = \hbar k_L^2/2M$. Note that in our system of scaled units, the commutator $[\phi, \rho] = i\hbar$, where $\hbar = 8\omega_r/\omega_m$.

5.2 Resonance Overlap

There are three resonances which (from the stationary phase condition) are centered at $\rho/\hbar(= p/2\hbar k_L) = 0, \pm\omega_m/8\omega_r$. The associated widths are determined by the well depth as we have already seen in Sec. 3.2. For the island centered at $\rho = 0$ the well depth is $2k$. Equating this to $\rho^2/2$ gives an approximate momentum width of

$$\frac{\Delta\rho_0}{\hbar} \approx \frac{4\sqrt{k}}{\hbar} = \sqrt{\frac{\Omega_{eff}}{8\omega_r}}. \tag{5.6}$$

The other resonances have half the well depth and hence

$$\frac{\Delta\rho_\pm}{\hbar} \approx \frac{2\sqrt{2k}}{\hbar} = \sqrt{\frac{\Omega_{eff}}{16\omega_r}}. \tag{5.7}$$

When the condition

$$\frac{\Delta\rho_0 + \Delta\rho_+}{2} > \frac{2}{3} \tag{5.8}$$

is met [69, 70], neighboring resonances overlap and the particle can now classically diffuse in momentum via dynamical chaos over a bounded region demarcated by confining KAM surfaces. Operationally, this condition is reached either by increasing the pulse duration (decreasing the frequency) for fixed laser intensity, as in our experiments, or by increasing the laser intensity for fixed pulse duration. Substituting for the widths provides an estimate of the time scale τ_{cr}

$$T_s > \tau_{cr} = \frac{2\sqrt{2}}{3(2+\sqrt{2})} \frac{2\pi}{\sqrt{\omega_r \Omega_{eff}}} , \tag{5.9}$$

beyond which the resonances overlap. On recognizing

$$\tau_{HO} = \frac{2\pi}{\sqrt{\omega_r \Omega_{eff}}} \tag{5.10}$$

to be the period of the small oscillation limit to the pendulum (harmonic oscillator), the threshold for overlap is given by

$$T_s > 0.28 \tau_{HO}. \tag{5.11}$$

The three rows of panels in Fig. 5.3 display the classical phase portraits (top), final momentum distributions calculated from the classical dynamics (middle), and the experimental results together with a quantum simulation (bottom). Each column corresponds to a different single pulse duration. In both the classical and quantum calculations, the initial momentum spread is taken from the temperature measurements in the experiment. The quantum calculation is a space-time integration of the Schrödinger equation starting from a squeezed wave-packet initial condition (see Sec. 3.3).

At these parameter values, resonance overlap is predicted to occur approximately at $\tau_{cr} = 245$ ns. As illustrated in the first column of panels, for durations less than this value the classical phase space consists of three isolated resonances and the initial distribution remains trapped within the central island. Some 'heating' of the initial condition can occur as the distribution

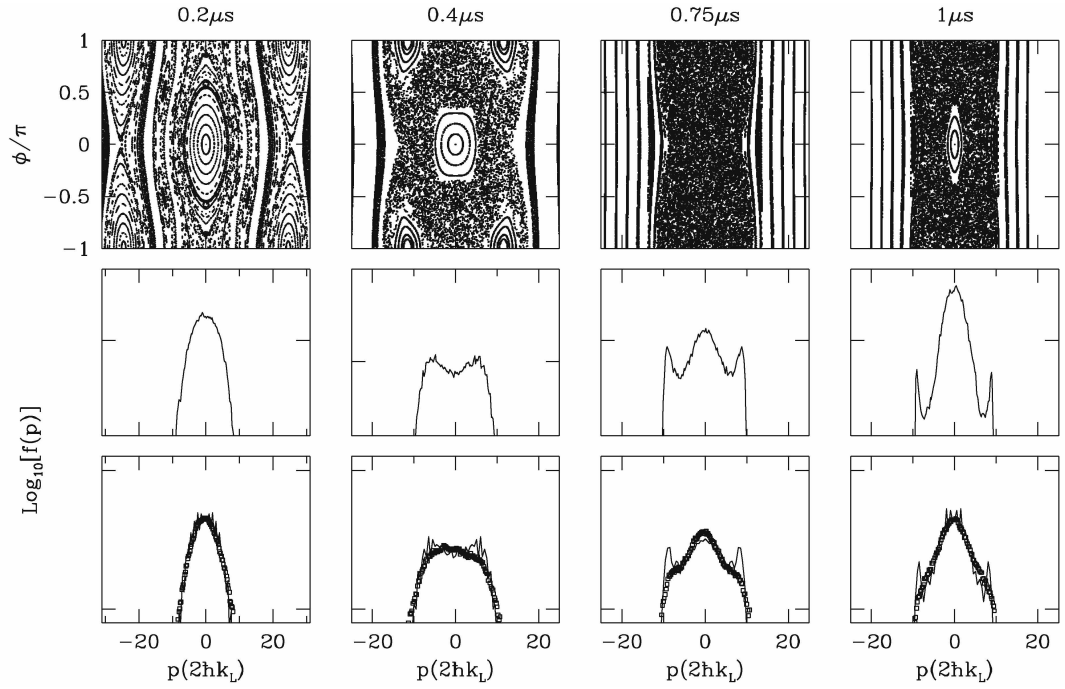

Figure 5.3: Classical phase portraits (upper panel), classical momentum distributions (middle panel), and experimentally measured momentum distributions with quantum theory (bottom panel, theory marked by lines) for $T_s = 0.2,\ 0.4,\ 0.75,\ 1.0\ \mu$s. $\Omega_{eff}/2\pi = 50.7$ MHz and the initial momentum distribution has a width of 2.9 in $2\hbar k_L$ units. The vertical scales for the distributions are logarithmic and are marked in decades [72].

spreads within this island. On crossing the threshold for overlap, a chaotic band appears over which the classical particle can diffuse. Quantum effects usually suppress this behavior and lead to the dynamical localization [1, 53, 52]. However, for interaction times short compared to the quantum break time [60, 62], classical and quantum simulations agree, even in the presence of chaos, as evident in the second and third columns. For a pulse duration of $T_s = 1$ μs quantum effects suppress diffusion, and an exponential lineshape associated with dynamical localization is seen [53, 52, 62].

Both classical and quantum simulations display peaks near the momentum boundaries which show up as less pronounced shoulders in the experimental distributions. This regime of short interaction times in the presence of nearby momentum boundaries is particularly sensitive to variations in Ω_{eff} present in the experiment due to the intensity variation across the laser beam. The experimental variation in Ω_{eff} across the atomic sample is typically 10 %. In the work of Chapters 3 and 4, the longer interaction times and the fact that the boundaries were further out allowed us to use an RMS value of Ω_{eff} to get close agreement between theoretical and experimental lineshapes without explicit time-averaging. The effect of this variation is similar to having a range of interaction times. It has been verified that time-averaging resolves the discrepancy between the simulations and the experiment though this is not relevant to the focus of this work as seen in Fig. 5.3.

To experimentally determine the threshold τ_{cr} for overlap, the momentum growth associated with spreading within the primary resonance must be distinguished from diffusion that can occur after resonance overlap. This is accomplished by measuring the momentum transferred from a potential $V(x) = (\hbar\Omega_{eff}/16)\cos(2k_L x)$ for the same duration as the $\sin^2$ case. This is simply a square pulse. In this case, there is only a single resonance which is identical to the primary resonance in the $\sin^2$ pulse due to the choice of relative

amplitudes. Therefore, the RMS prior to resonance overlap should be the same in both cases. After resonance overlap is crossed, there should be a distinct increase in the $\sin^2$ RMS as compared with the square pulse. The experimental results in Fig. 5.4(a) show the RMS momentum for both cases as a function of pulse duration (rise and fall times of 25 ns are included in the square pulse duration). These agree well with numerical simulations in Fig. 5.4(b) and the estimated resonance overlap threshold. For the square pulse, the oscillation within the spatially periodic potential is clear and further validates the single particle quantum description of the experimental atomic statistical ensemble. Note that crossing the overlap threshold is more clearly visible in the lineshape than in the RMS momentum, but the rms is a more quantitative measure.

5.3 Adiabatic Limit

In the limit of long pulse period one expects adiabatic behavior and in simple quantum systems such as the harmonic oscillator, the conditions for adiabaticity are clear. However in nonlinear quantum systems there is generally not a single time scale, and the conditions for adiabaticity must be analyzed more carefully. A prominent feature in the phase portraits in Fig. 5.3 is the narrowing of the chaotic band, measured in momentum units of $2\hbar k_L$, with increasing pulse duration. This is seen easily by considering the width of the band of chaos given by

$$\frac{\Delta\rho}{\hbar} = \frac{\Delta p}{2\hbar k_L} = \frac{2(1+\sqrt{2k})}{\hbar} \tag{5.12}$$

which on defining the pulse duration $T_s = \alpha\tau_{HO}$ can be rewritten as

$$\frac{\Delta\rho}{\hbar} = \frac{\pi}{2\omega_r\tau_{HO}}\frac{(1+\alpha)}{\alpha}\,, \tag{5.13}$$

Thus the number of states (separated by $2\hbar k_L$) within the chaotic band decreases with increasing pulse duration. A simple estimate for an adiabatic threshold is obtained by setting $\Delta\rho/\hbar$ equal to the initial thermal momentum

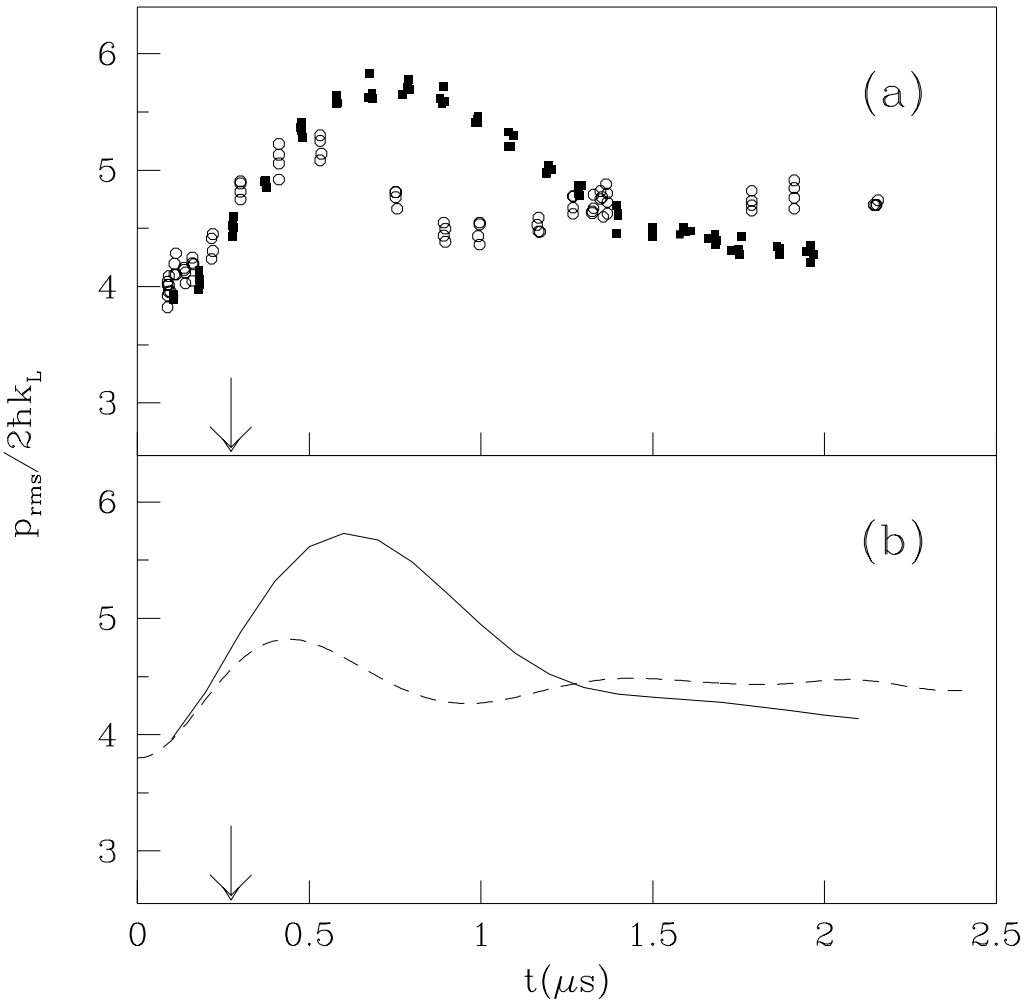

Figure 5.4: (a) RMS momentum computed from experimentally measured momentum distributions for $\sin^2$ (solid) and square (open) pulses. (b) The corresponding quantum simulations are the solid and dashed lines. The threshold estimated from resonance overlap is indicated by the arrow. A clear deviation occurs at a pulse duration close to the predicted value. An absolute power calibration was not available for this data due to a problem with a detector. The momentum transfer for the square pulse was consistent with $\Omega_{eff}/2\pi = 41$ MHz. The initial momentum spread was 3.8 in $2\hbar k_L$ units [72].

spread of the atoms. Operationally, this condition requires the width of the chaotic band to be several times the width σ_p of the thermal Gaussian. For example, considering $\Delta\rho/\hbar = 4\sigma_p$ leads to

$$\alpha \geq \frac{1}{((\frac{8\sigma_p\omega_r}{\pi})\tau_{HO} - 1)} , \tag{5.14}$$

which is valid when the denominator is positive and which shows a strong dependence on the initial momentum width. Thus, for the parameters of Fig. 5.3 ($\sigma_p = 2.9$) adiabatic behavior occurs only for times longer than ≈ 25 μs while for Fig. 5.4 ($\sigma_p = 3.8$) the threshold is ≈ 2 μs. These timescales are fully consistent with the experimental pulse durations where the lineshape approaches the initial condition.

Our discussion has focused on the $\sin^2$ pulse profile, though these results can be applied to other pulse shapes. For example, earlier work on momentum transfer was performed in an atomic beam crossing a standing wave of light [73]. The resulting temporal pulse is then of the form $e^{-(t/T)^2}$. In practice, the laser beam profile has a natural cut-off imposed by spatial filtering which leads to a well-defined period of the pulse analogous to the pulse duration in the $\sin^2$ profile. The potential can now be written as a discrete Fourier sum in multiples of this fundamental frequency and resonance overlap can result. Parameters where resonance overlap is significant can be attained though this was not the case for the parameters in Ref. [73].

Experimentally the resonance overlap route to global classical chaos has been tested. These results illustrate that for nonlinear time dependent systems, novel physics can occur on intermediate timescales. This 'gray zone' between fast passage and adiabatic interactions is, in fact, the generic situation and must be studied. In particular, interactions of standing waves of light with ultra-cold atoms clearly fall into this category and progress in control and manipulation of atomic motion must take these factors into account.

Chapter 6

Future Directions in Atom Optic Quantum Chaos

6.1 Conclusions

Thus far we have realized a periodically driven rotor using atom optics where the underlying classical phase space goes from stable to chaotic as a control parameter is varied. The experimental results are in good absolute agreement with a quantum Floquet analysis and with a quantum simulation. The quantum evolution can be related to the underlying classical dynamics in this mixed phase space regime.

We also have the first direct experimental realization of the quantum δ-kicked rotor. A standing wave is pulsed on periodically in time to approximate a series of delta functions. Momentum spread of the atoms increases diffusively with every pulse until the "quantum break time" after which exponentially localized distributions are observed. Quantum resonances are found for rational ratios of pulse period to natural period. Preliminary studies of noise induced delocalization have also been performed (see Sec. 6.3).

In addition, momentum transfer from a single pulse of a standing wave of light to a sample of atoms was studied. What is observed is a sharp increase in the momentum transfer when the pulse duration exceeds a critical value τ_{cr}. A classical analysis of nonlinear resonances shows that resonance overlap occurs at τ_{cr}, and there is a transition to global classical chaos. These results are a

direct experimental test of the "resonance overlap criteria" and illustrate that even the turning on and off of a nonlinear interaction can lead to surprising and novel results. This type of time-dependent interaction is ubiquitous and occurs, for example, whenever an atomic beam passes through a standing wave of light. This could have profound implications for many experiments. An estimate of the adiabatic timescale is also given for this nonlinear system.

6.2 Future Directions

What we have done thus far with the atom optics realization of quantum chaos is only the tip of the iceberg. Looking towards future studies of quantum dynamics in a mixed classical phase space (see Chapter 3) it is clear that better confined initial conditions could open new areas of research. In the present work, initial conditions are Gaussian distributed in p and uniformly distributed in x on the scale of the standing wave period. It is within reach of current trapping and cooling technology to localize the atoms within the standing waves. Relative to the phase portraits shown in Chapter 3, this would place the initial conditions within a "box" in phase space, which would enable many interesting directions for future work. For example, if the atoms are initially prepared within an island of stability, classically they would remain there indefinitely. It may be possible to directly observe dynamical quantum tunneling from an island. Control of initial conditions may also enable a direct study of the enhanced probability associated with ghosts and scars [74] in this system, which would have important consequences in the field of quantum chaos.

For the δ-kicked rotor of Chapter 4 continuing studies of noise induced delocalization should provide interesting insights into the physics, as discussed in Sec. 6.3. The role of dimensionality on localization has been studied extensively for the Anderson problem in two and three dimensions [75]. Extra

degrees of freedom can be attained by introducing additional spatial periodicities to the δ-kicked rotor of Chapter 4 or by adding additional modulation frequencies to the modulated system of Chapter 3. This provides other ladders of states separated by to connect to. These added pathways mimic higher dimensions.

6.3 Noise and Dissipation

The quantum behavior of classically chaotic systems is dominated by coherence effects, including dynamical localization [1, 76]. Up to this point, every effort has been made to reduce the effects of decohering noise on the system, by detuning sufficiently far to avoid spontaneous emission, by power locking the laser to avoid amplitude noise, and by keeping the interaction sufficiently short so that phase noise in the standing wave is minimal. One question is how sensitive a particular coherence effect, such as dynamical localization, under study is against degradation. Another question is what are the effects of different types of noise [76]. The effects of noise have been studied experimentally in the case of ionization of Rydberg atoms [77].

In our system the canonical variables are position and momentum, as opposed to angle and angular momentum for the quantized rotor. The observed effects reported so far are identical for both systems. Momentum is not quantized, but the transitions that are induced by the standing wave couple only momenta that differ by $2n\hbar k_L$, where n is an integer. If initially an atom is prepared in a state with momentum p_o, it can only reach states connected by a ladder $p_0 + n2\hbar k_L$, where n is an integer. Noise can be introduced in the standing wave in the form of amplitude noise, phase noise, or noise in the period between kicks. This parametric type of noise, however, still preserves the available ladder of states spaced by $2\hbar k_L$. Another type of noise is spontaneous emission, where the random momentum projection along the axis of interest is

anything between 0 and $\hbar k_L$, but again the atom returns to a (shifted) ladder of states spaced by $2\hbar k_L$. However, by adding noise terms that break the spatial periodicity, the quantum dynamics can be substantially different than for a kicked rotor [78, 79, 80, 81, 82, 83, 84]. This can be achieved experimentally by adding a standing wave that has a different, incommensurate periodicity (see Sec. 1.1). The effects of "symmetry breaking" potentials both in the context of noise induced delocalization, and localization in two and three dimensions offer fertile grounds for study.

The most interesting case to study is that of weak noise [84]. Suppose this noise destroys quantum coherence after a characteristic time t_c. If the variance of the noise is ν, coherence is destroyed when there is an appreciable probability for noise-induced transitions between levels, so

$$t_c = \frac{\hbar^2}{\nu} \tag{6.1}$$

Noise is considered to be weak if t_c is large compared to the quantum break time t^*:

$$t^* \ll t_c. \tag{6.2}$$

Under this circumstance, localization is still present. If the duration of the interaction is much shorter than t_c, the effect of noise can be ignored altogether (which is presumed to be the case with all experiments described thus far). On the other hand, if t_c is less than the interaction time, rather than localizing to a constant value, diffusion in p (Eq 4.16) is resurrected with a much smaller diffusion constant.

$$D_{noise} = \frac{t^*}{t_c} D \tag{6.3}$$

where D is the classical diffusion rate. For the specific case of spontaneous emission the theoretical noise-induced diffusion constant is

$$D_{noise} \propto N \tag{6.4}$$

where N is the probability of spontaneous emission [85, 86]. In addition, the characteristic exponential distribution is predicted to be approximately Gaussian when a sufficient level of spontaneous emission is present.

Experimentally both amplitude and phase parametric noise have been attempted. As discussed Sec. 2.3.4, a random number sequence is used to set the value of the phase or amplitude for each pulse. The results are very tentative and all experimental parameters have not been well characterized so far. Qualitatively, as noise is increased an increased noise induced rate of diffusion is observed, and the characteristic exponential lineshapes become approximately Gaussian. Unfortunately for the experiments thus far, the increased momentum spread was limited by the classically predicted border in momentum space (Eq. 4.36). The solution to this, of course, is to reduce the duration of the pulses down to the minimum $\tau = 50$ ns. In addition, there is a great deal of scatter in each curve. Ideally, the experiment should be repeated for a large number of random number sequences, and the results for each value of the noise variance should be averaged.

6.4 Beyond Quantum Chaos

Quantum chaos is only one of many directions that time-dependent Hamiltonians can lead in atom optics. Very general time dependencies can be achieved by using AOMs and EOMs for amplitude and phase modulation using arbitrary waveform generators. In principle, very general spatial dependencies can also be achieved. If beams are crossed at angles other than 180° (counter propagating) then the periodicity of the standing wave can be varied (see Sec 1.1). One could imagine several pairs of beams, forming several periodicities, superposed to make a non-sinusoidal waveform. Ideally, one could reproduce any periodic function if a Fourier series representation is made. It might be argued that this will result in more than just a one-dimensional standing wave due

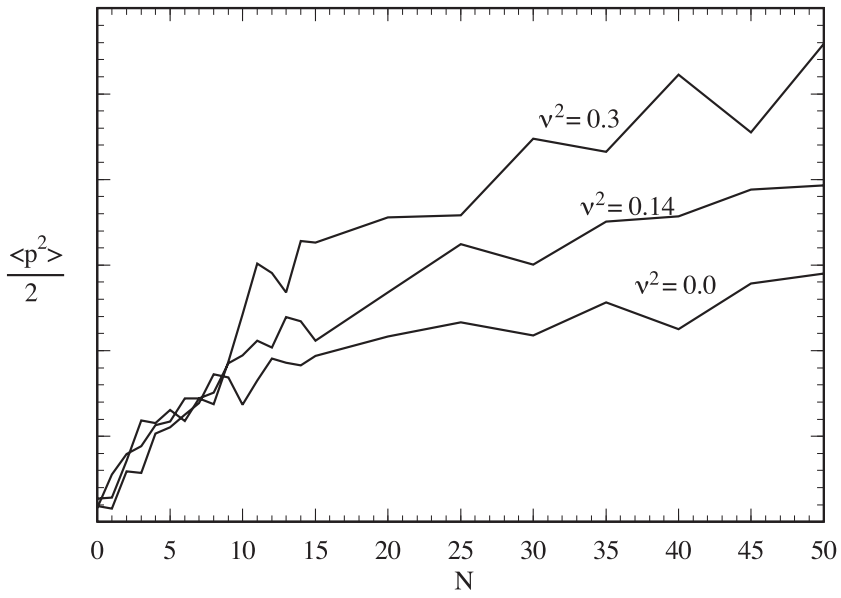

Figure 6.1: Preliminary experimental observation of amplitude noise-induced delocalization. Tentative phase noise induced delocalization experiments give qualitatively similar results.

to unintended cross terms. This effect can be eliminated if pairs of beams are offset in frequency by a 80 MHz AOM, for example. In this case, the cross terms would be moving with a high velocity and would have almost no effect on the atoms for the same reason that the resonant kick boundary discussed in Chapter 3 turns off the interaction. With this one could then make a standing wave of arbitrary time and spatial dependence. Such a scheme could open up many exciting possibilities not only for quantum chaos but for atom optics in general. One could consider manipulating atomic wavepackets into a desired state, perhaps incorporating the ideas of quantum control applied to external atomic degrees of freedom. Quantum control theory provides an algorithm to find the appropriate time dependent Hamiltonian to go from an initial state to a desired final state.

$$e^{-\frac{i}{\hbar}\int_0^T \hat{H}(t)dt}\Psi_i(p) = \Psi_f(p) \tag{6.5}$$

In chemistry, for example, quantum control ideas are being tested that use non-trivial time dependent fields to selectively break bonds in complicated molecules [87]. The atom optical approach has the advantage that the potentials involved are fully understood, the timescales are much more easily realized, and one has an extremely good measure of the outcome. This would be an excellent testing ground for the ideas of quantum control. The generation of atomic wave packets could be used in atom optics to produce a coherent atomic beam splitter, for example.

Time dependent potentials could also be used to study effects in a periodic lattice of interest to the solid state community. The atom optic system is appealing because studies can be done in the absence of site impurities and dissipation. Landau-Zener tunneling [88], Wannier Stark ladders [89], and particle transport in quasi-crystals are but a few examples.

Bibliography

[1] R. Graham, M. Schlautmann, and P. Zoller, Phys. Rev. A **45**, R19 (1992).

[2] Martin Fischer, Master's Thesis, The University of Texas at Austin, 1993.

[3] Laser cooling and trapping is reviewed by Steven Chu in Science **253**, 861 (1991).

[4] M. H. Anderson, J. R. Ensher, M. R. Matthews, C. E. Wieman, and E. A. Cornell, Science **269**, 198 (1995).

[5] P. Meystre, and M. Sargent III, *Elements of Quantum Optics*, Springer-Verlag (1991).

[6] Claude Cohen-Tannoudji, Jacques Dupont-Roc, and Gilbert Grynberg, *Atom-Photon Interactions*, Wiley and Sons (1992).

[7] Phillip Gould, Am. J. Phys. **62** 1046 (1994).

[8] W. Demtröder, *Laser Spectroscopy*, Springer-Verlag (1988).

[9] W. L. Wiese, M. W. Smith, and B. M. Miles, *Atomic Transition Probabilites*, v. 2, National Standard Reference Data Service, National Bureau of Standards (1969).

[10] P. W. Milonni, and B. Sundaram, in *Progress in Optics XXXI*, 1, North-Holland (1993).

[11] S. Fishman, Quantum Localization, Lecture Notes for the 44th Scottish Universities Summer School in Physics, Stirling, Scotland (1994).

[12] Shmuel Fishman, private communication.

[13] Dominique Delande, and Andreas Buchleitner, Classical and Quantum Chaos in Atomic Systems, p. 85, in *Advances in Atomic, Molecular, and Optical Physics*, v. 34, Benderson and Walther eds., Academic Press (1994).

[14] A. Peres, Proc. of Adriatico Conf., in *Quantum Chaos*, H. Cerdiera, G. Casati, and R. Ramaswamy, eds., World Scientific (1990).

[15] R. V. Jensen, S. M. Susskind, and M. M. Sanders, Phys. Rep. **201**, 1 (1991).

[16] B. Sundaram, and R. V. Jensen, Phys Rev. **A47**, 1415 (1993).

[17] C. Iu, G. R. Welch, M. M. Kash, D. Kleppner, D. Delande, and J. C. Gay, Phys. Rev. Lett. **66**, 145 (1991).

[18] Feldmann, Physics Reports (1982).

[19] D. J. Thoules, Phys. **C5**, 77 (1972).

[20] S. Fishman, D. R. Grempel, and R. E. Prange, Phys Rev. **A29**, 1639 (1984).

[21] R. Graham, M. Schlautmann, and D. L. Shepelyansky, Phys. Rev. Lett. **67**, 2 (1991).

[22] C. M. Marcus, A. J. Rimberg, R. M. Westervelt, P. F. Hopkins, and A. C. Gossard, Phys. Rev. Lett. **69** (3), 506 (1992).

[23] M. Latka, and B. J. West, Phys. Rev. Lett. (to appear).

[24] Martin, Peter, Dissertation, MIT, 1987.

[25] *New Focus Inc.* catalog, 1995-1996.

[26] J. Kelly, A. Gallagher, Rev. Sci. Instrum. **58** (4), 563 (1987).

[27] S. Zilio, E. Montiero, E. Marega, V. Bagnato, Revisia De Fisica Aplicadae Instrumentacao **6**, 130 (1991).

[28] T. Gallagher, N. Traw, J. Watjen, App. Opt. **25** (4), 510 (1986).

[29] W. Hardy, L. Whitehead, Rev. Sci. Instrum. **52** (2), 213 (1981).

[30] Edward Tomme, Master's Thesis, The University of Texas at Austin 1994.

[31] J. L. Hall, L. Hollberg, T. Baer, H. G. Robinson, Appl. Phys. Lett. **39**(9), 680 (1981).

[32] L. Hollberg, Ma Long-Sheng, M. Hohenstatt, J. L. Hall, *Proc. of SPIE: Laser-based Ultrasensitive Spectroscopy and Detection V*, v. 426, 91 (1983)

[33] Mark Kasevich, Dissertation, Stanford University, 1992.

[34] Bernd Maisenhölder, "Frequenzstabilisierung eines Titan-Saphir-Laser-Systems", Diplomarbeit Universität Konstanz, Dec. 1993.

[35] *Spectra Moleculaire de l'Iode*, Lab Aime Cotton, Orsay-France.

[36] S. Gerstenkorn, Revue De Physique Appliquee **14**, 791 (1979).

[37] Sune Svanberg *Atomic and Molecular Spectroscopy*, 2 ed., Springer-Verlag (1992).

[38] T. W. Hansch, and B Couillaud, Optics Comm., **35** (3), 441 (1980).

[39] E. K. Hasle, Optics Comm. **31**(2), 206 (1979).

[40] R. Balhorn, H. Kunzmann, F. Lebowsky, App. Opt. **11** (4), 742 (1972).

[41] L. B. Arguimbau, R. D. Stuart, *Frequency Modulation*, John Wiley and Sons (1956).

[42] W. W. Macalpine, R. O. Schildknecht, Proc. of the IRE, 2099 (1959).

[43] Rodney Loudon, *The Quantum Theory of Light*, Oxford (1983).

[44] Claude N. Cohen-Tannoudji, and William D. Phillips, Physics Today, 33, Oct. 1990.

[45] P. D. Lett, W. D. Phillips, S. L. Rolston, C. E. Tanner, R. N. Watts, and C. I. Westbrook, J. Opt. Soc. Am. B **6**(11), 2084 (1989).

[46] C. Cohen-Tannoudji, Laser Manipulation of Atoms and Ions, Proceedings of the International School of Physics 'Enrico Fermi' CXVIII, North-Holland Press (1992).

[47] David S. Weiss, Erling Riis, Yaakov Shevy, P. Jeffry Ungar, and Steven Chu, J.Opt. Soc. Am. B bf 6(11), 2072 (1989).

[48] Alain Aspect, Laser Manipulation of Neutral Atoms, p. 193, in *Laser Interactions with Atoms, Solids, and Plasmas*, ed. R. M. More, Plenum Press, NY (1994).

[49] Graham P. Collins, Search and Discovery, Physics Today, p.18, June 1995.

[50] See contributions in *Irregular Atomic Systems and Quantum Chaos* Ed. J. C. Gay, Gordon & Breach, NY (1992).

[51] P. J. Bardroff, I. Bialynicki-Birula, D. S. Krähmer, G. Kurizki, E. Mayr, P. Stifter, and W. P. Schleich, Phys. Rev. Lett. **74**, 3959 (1995).

[52] J. C. Robinson, C. Bharucha, F. L. Moore, R. Jahnke, G. A. Georgakis, Q. Niu, M. G. Raizen, and Bala Sundaram, Phys. Rev. Lett. **74**, 3963 (1995).

[53] F. L. Moore, J. C. Robinson, C. Bharucha, P. E. Williams, and M. G. Raizen, Phys. Rev. Lett. **73**, 2974 (1994).

[54] S. E. Koonin and D. C. Meredith, *Computational Physics*, Addison Wesley, Menlo Park (1990).

[55] Cyrus Bharucha, Master's Thesis, The University of Texas at Austin, 1994.

[56] Ya. B. Zeldovich, *JETP* (U.S.S.R.) **24**, 5 (1967).

[57] D. J. Thouless, Phys. Rep. **13**, 93 (1974); Shmuel Fishman, D. R. Grempel, and R. E. Prange, Phys. Rev. Lett. **49**, 8 (1982).

[58] Doron Iliescu, Shmuel Fishman, and Eshel Ben-Jacob Phys. Rev. B **46**, 14675 (1992).

[59] A. L. Lichtenberg, and M. A. Lieberman, *Regular and Chaotic Dynamics* Springer-Verlag (1991).

[60] L. E. Reichl, *The Transition to Chaos in Conservative Classical Systems: Quantum Manifestations* Springer-Verlag (1992) and references therein.

[61] R. Blümel, S. Fishman, and U. Smilansky, J. Chem. Phys. **84**, 2604 (1986).

[62] F. L. Moore, J. C. Robinson, C. F. Bharucha, Bala Sundaram, and M. G. Raizen, Phys. Rev. Lett. (in press).

[63] Michael Tabor. *Chaos and Integrability in Nonlinear Dynamics*. Wiley-Interscience (1989).

[64] B. V. Chirikov, F. M. Izrailev, and D. L. Shepelyansky, Sov. Sci. Rev. Sec. C2, 209 (1981)

[65] D. L. Shepelyansky, Phys. Rev. Lett. **56**, 677 (1986), Physica **28**D, 103 (1987).

[66] I. Dana, E. Eisenberg, and N. Shnerb, Phys. Rev. Lett. **74** (5), 686 (1995).

[67] F. M. Izrailev, and D. L. Shepelyansky, Sov. Phys. Dokl. **24**, 996 (1979); Theor. Math. Phys. **43**, 553 (1980).

[68] Q. Niu and Bala Sundaram, submitted for publication.

[69] B. V. Chirikov, Phys. Rep. **52**, 265 (1979).

[70] G.H. Walker, and J. Ford, Phys. Rev. **188**, 416 (1969).

[71] Resonance overlap in the stochastic heating of a plasma interacting with a large-amplitude standing wave was first reported by F. Doveil, Physical Review Letters **46**, 532 (1981). See A. Fasoli, F. Skiff, and M. Q. Tran, Phys. Plasmas **1**, 1452 (1994) for more recent results.

[72] J. C. Robinson, C. F. Bharucha, K. Madison, F. L. Moore, Bala Sundaram, S. R. Wilkinson, and M. G. Raizen, submitted to Phys. Rev. Lett.

[73] see, for example, P. J. Martin, P. L. Gould, B. G. Oldaker, A. H. Miklich, and D. E. Pritchard, Physical Review A **36**, 2495 (1987).

[74] E. J. Heller, and S. Tomsovic, Phys. Today **46**, 38 (1993).

[75] G. Cassati, I. Guarneri, D.L. Shepelyansky, Phys. Rev. Lett. **62** (4), 345 (1989).

[76] R. Graham, Quantum Coherence and Decoherence in a Classically Chaotic Experimentally Accessible Quantum Optical System, XXXI Winterschool of Theoretical Physics 'Chaos: The Interplay of Classics, Stochastics, and Quanta', Karpacz Poland, Feb. 1995.

[77] Blümel, R., R. Graham, L. Sirko, U. Smilansky, H. Walther, and K.Yamada, Phys. Rev. Lett. **62** (4), 341 (1989).

[78] E. Ott, and T. M. Antonsen, Jr., Phys. Rev. Lett. **53** (23), 2187 (1984).

[79] T. Dittrich, and R. Graham, Europhys. Lett. **7** (4), 287 (1988).

[80] T. Dittrich, and R. Graham, Europhys. Lett. **7**(3), 263 (1987).

[81] D. Cohen, Phys. Rev. Lett.**67** (15), 1945 (1991).

[82] D. Cohen, Phys. Rev. A, **43** (2), 639 (1991).

[83] Doron Cohen, Phys. Rev. A **44** (4), 2292 (1991).

[84] S. Fishman, and D. L. Shepelyansky, Europhys. Lett.**16**, 643 (1991).

[85] Robert Graham, XXXI Winterschool of Theoretical Physics, Karpacz, Poland, 1995.

[86] S. Dyrting, and G.J. Milburn, Phys. Rev. A **51** (4), 3136 (1995).

[87] S. Shi, and H. Rabitz, J. Chem. Phys. **92** (1), 364 (1990).

[88] Y. Gefen, and D.J. Thouless, Phys. Rev. Lett. **59** (15), 1752 (1987).

[89] E. E. Mendez, G. Bastard, Physics Today, 34, June 1993.

Vita

John Charles Robinson was born on June 19, 1964 to Jeanne and Charles Robinson in Minneapolis, Minnesota. After graduating from Breck High School in Minneapolis, John earned his Bachelor's degree in physics at Carleton College in 1986. In 1991 he earned a Master's degree in physics under the supervision of Professor Manfred Fink researching spontaneous Raman spectroscopy at The University of Texas at Austin. In the fall of 1991 Mark G. Raizen arrived as a new Assistant Professor of physics at The University of Texas at Austin. As Mark's first graduate student, John began the daunting task of building a brand new state-of-the-art laser physics laboratory from the ground up. In the beginning John primarily worked on laser cooled ions in rf-traps to study quantum optics. In 1993 he began working on the atom-optic realization of quantum chaos with ultra-cold atoms, which is presented here.

Permanent address: 706 East 47th Street
Austin TX 78751
U.S.A.

This dissertation was typeset with LaTeX[‡] by the author.

[‡]LaTeX is a document preparation system developed by Leslie Lamport as a special version of Donald Knuth's TeX Program.